

# Naval Research Laboratory

Washington, DC 20375-5320

AD-A278 785



2

NRL/FR/8121--93-9545

## UVPI Imaging from the LACE Satellite: The Low Cost Launch Vehicle (LCLV) Rocket Plume

H.W. SMATHERS  
D.M. HORAN

*Space Systems Development Department  
Naval Center for Space Technology*

J.G. CARDON  
E.R. MALARET  
L. PEREZ

*Applied Coherent Technology Corporation  
Herndon, Virginia*

T. TRAN

*AlliedSignal Technical Services Corporation  
Alexandria, Virginia*

J.E. BRANDENBURG

*Research Support Instruments  
Alexandria, Virginia*

September 24, 1993

Unpublished contains color  
images. All DTIC reproductions  
must be in black and  
white.

DTIC  
SELECTED  
MAY 03 1994  
S B D

11407 94-13214

Approved for public release; distribution unlimited.

04 5 02 087

# DISCLAIMER NOTICE



THIS DOCUMENT IS BEST QUALITY AVAILABLE. THE COPY FURNISHED TO DTIC CONTAINED A SIGNIFICANT NUMBER OF COLOR PAGES WHICH DO NOT REPRODUCE LEGIBLY ON BLACK AND WHITE MICROFICHE.

PAGES \_\_\_\_\_  
ARE  
MISSING  
IN  
ORIGINAL  
DOCUMENT

REPORT DOCUMENTATION PAGE			Form Approved OMB No. 0704-0188	
Public reporting burden for this collection of information is estimated to average 1 hour per response, including the time for reviewing instructions, searching existing data sources, gathering and maintaining the data needed, and completing and reviewing the collection of information. Send comments regarding this burden estimate or any other aspect of this collection of information, including suggestions for reducing this burden, to Washington Headquarters Services, Directorate for Information Operations and Reports, 1216 Jefferson Davis Highway, Suite 1204, Arlington, VA 22202-4302, and to the Office of Management and Budget, Paperwork Reduction Project (0704-0188), Washington, DC 20503.				
1. AGENCY USE ONLY (Leave Blank)	2. REPORT DATE  September 24, 1993	3. REPORT TYPE AND DATES COVERED  Interim		
4. TITLE AND SUBTITLE  UVPI Imaging from the LACE Satellite: The Low Cost Launch Vehicle (LCLV) Rocket Plume		5. FUNDING NUMBERS  PE-63217C PMA-N1305		
6. AUTHOR(S)  H.W. Smathers, D.M. Horan, J.G. Cardon, <sup>1</sup> E.R. Malaret, <sup>1</sup> L. Perez, <sup>1</sup> T. Tran, <sup>2</sup> and J.E. Brandenburg <sup>3</sup>				
7. PERFORMING ORGANIZATION NAME(S) AND ADDRESS(ES)  Naval Research Laboratory Washington, DC 20375-5320		8. PERFORMING ORGANIZATION REPORT NUMBER  NRL/FR/8121--93-9545		
9. SPONSORING/MONITORING AGENCY NAME(S) AND ADDRESS(ES)  Strategic Defense Initiative Organization Washington, DC 20301		10. SPONSORING/MONITORING AGENCY REPORT NUMBER		
11. SUPPLEMENTARY NOTES  <sup>1</sup> Applied Coherent Technology Corporation, Herndon, Virginia <sup>3</sup> Research Support Instruments, Alexandria, Virginia <sup>2</sup> AlliedSignal Technical Services Corporation, Alexandria, Virginia				
12a. DISTRIBUTION/AVAILABILITY STATEMENT  Approved for public release; distribution unlimited.			12b. DISTRIBUTION CODE	
13. ABSTRACT (Maximum 200 words)  The Ultraviolet Plume Instrument (UVPI) is a small, plume-tracking instrument flown on the Naval Research Laboratory's Low-power Atmospheric Compensation Experiment (LACE) satellite. The plume camera has a relatively narrow field of view, 0.184° by 0.137°, and observes sources through any of four filters with passbands of 195 to 295 nm, 200 to 320 nm, 235 to 350 nm, and 300 to 320 nm. The LCLV (Low Cost Launch Vehicle) was launched from Wallops Island, Virginia, before sunrise on 6 February 1991. The third stage, powered by an Aries solid-fuel rocket motor, reached a 117-km altitude and was successfully detected and tracked by the UVPI from a range of 450 to 550 km. The spectral radiance and spectral radiant intensities of the missile plumes were extracted from these images for the four passbands.				
14. SUBJECT TERMS Ultraviolet Plume Instrument      Plume Tracking      Low Cost Launch Vehicle UVPI      Spectral radiance      Aries motor UV      Spectral radiant intensities      Missile plumes LACE satellite      LCLV      Plume imaging			15. NUMBER OF PAGES  115	
			16. PRICE CODE	
17. SECURITY CLASSIFICATION OF REPORT  UNCLASSIFIED	18. SECURITY CLASSIFICATION OF THIS PAGE  UNCLASSIFIED	19. SECURITY CLASSIFICATION OF ABSTRACT  UNCLASSIFIED	20. LIMITATION OF ABSTRACT  UL	

## CONTENTS

EXECUTIVE SUMMARY .....	E-1
1.0 INTRODUCTION .....	1
1.1 Background .....	1
1.2 UVPI Capability .....	1
1.3 Scientific Objectives for UVPI .....	3
1.3.1 Specific Objectives Related to Radiometrics .....	3
1.3.2 Specific Objectives Related to Spatial Features .....	4
1.3.3 Specific Objectives Related to Temporal Features .....	4
1.3.4 Specific Objectives Related to Spectral Features .....	4
1.4 Experiment Concept .....	4
1.4.1 LCLV Trajectory and Description .....	4
1.4.2 Radiometrics .....	5
2.0 LCLV OBSERVATION AND INSTRUMENT PERFORMANCE .....	6
2.1 Observation Scenario .....	6
2.2 LCLV Performance Summary .....	7
2.3 Encounter Geometry .....	7
3.0 EXTRACTION OF RADIOMETRIC QUANTITIES .....	10
3.1 Data Calibration Procedure .....	10
3.1.1 Discrimination of Photoevents .....	11
3.2 Relation of Photoevents to Source Radiance .....	12
3.3 The Peak Normalized Radiance Approximation .....	14
3.4 Reference Spectrum for Aluminum-Loaded Propellants .....	15
3.5 Use of the Reference Spectrum to Calculate a Scaling Constant .....	16
3.6 Centroid Wavelength Determination .....	18
3.7 Calculations of Radiance and Radiant Intensity .....	18
3.8 Summary of Radiometric Conversion Constants .....	19
4.0 PLUME DATA .....	19
4.1 Data Intervals .....	20
4.1.1 Description of Intervals .....	20
4.1.2 Calibration Parameters Associated with Intervals .....	21
4.2 Intensity History Overview .....	21
4.3 Single Images .....	23
4.4 Composite Plume Camera Images and Contour Plots .....	24
4.5 Calibrated Tracker-Camera Images .....	45
4.6 Error Analysis for Radiometric Observations .....	58
4.6.1 Due to Measurement Noise .....	58
4.6.2 In Gain Conversion Factor .....	59
4.6.3 Calculation of Total Error .....	60
4.7 Noise Equivalent Radiance .....	62
5.0 SPATIAL FEATURES .....	63
5.1 Delineation of Plume Central and Outer Regions .....	63
5.2 Plume Extent and Point Spread Function .....	65

5.3	Comparison of Results to CHARM 1.4 Predictions . . . . .	66
6.0	TEMPORAL FEATURES . . . . .	75
6.1	Plume Camera Intensity Plots . . . . .	75
6.2	Tracker-Camera Intensity Plots . . . . .	84
7.0	SPECTRAL ANALYSIS OF PLUMES . . . . .	87
7.1	Observed Spectral Radiant Intensities . . . . .	87
7.2	Discussion . . . . .	89
8.0	PERSISTENT CLOUDS OR TRAILS . . . . .	89
9.0	COMPARISON OF LCLV WITH OTHER TEST FLIGHTS . . . . .	89
9.1	The Far-UV Excess . . . . .	92
9.2	Luminous Plume Outer Region . . . . .	92
10.0	SUMMARY AND CONCLUSIONS . . . . .	102
10.1	Summary . . . . .	102
10.2	Achievement of Objectives . . . . .	104
10.2.1	General Objectives . . . . .	104
10.2.2	Specific Objectives Related to Spatial Features . . . . .	104
10.2.3	Specific Objectives Related to Temporal Features . . . . .	105
10.2.4	Specific Objectives Related to Spectral Features . . . . .	105
10.3	Conclusions . . . . .	105
	REFERENCES . . . . .	106
	APPENDIX A: LCLV Trajectory Parameters . . . . .	109
	APPENDIX B: UVPI Parameters . . . . .	119
	GLOSSARY . . . . .	129

Accession For	
NTIS GRA&I	<input checked="" type="checkbox"/>
DTIC TAB	<input type="checkbox"/>
Unannounced	<input type="checkbox"/>
Justification	
By	Distribution
Availability Codes	
Dist	Avail and/or Special
A-1	

## EXECUTIVE SUMMARY

The Ultraviolet Plume Instrument (UVPI) [1] is a small, plume-tracking instrument flown on the Naval Research Laboratory's Low-power Atmospheric Compensation Experiment (LACE) satellite, which was launched on 14 February 1990. The Low Cost Launch Vehicle (LCLV) was the third demonstration of the ability of the UVPI to observe and track missiles in flight above the atmosphere. The LCLV had been launched from Wallops Island, Virginia, on 6 February 1991. The launch time and trajectory were selected to synchronize the flight with the LACE satellite's pass.

Missile tracking in the ultraviolet is advantageous because of:

- extremely low Earth and solar backgrounds,
- extremely sensitive photodetectors that do not require cryogenic cooling, and
- very high optical resolution that is made possible by optics of relatively modest size.

The UVPI system aperture is only 10 cm in diameter. However, it can detect and image missile plumes at a 500-km range. The two cameras of the instrument use narrowband filters, image intensifiers, and charge-coupled device (CCD) detectors to observe sources in the ultraviolet band. The primary function of the tracker camera, which views over a relatively wide field ( $1.98^\circ$  by  $2.60^\circ$ ) and broad spectrum (255 to 450 nm), is to locate and track a source for higher resolution observation by the plume camera. The plume camera has a narrow field of view ( $0.184^\circ$  by  $0.137^\circ$ ) and observes sources through any of four filters with passbands of 195 to 295 nm, 220 to 320 nm, 235 to 350 nm, and 300 to 320 nm. The wavelengths shorter than 310 nm are essentially invisible from the ground because of atmospheric absorption. The limiting resolution of the tracker camera is about 230  $\mu$ rad (mrad) and that of the plume camera is about 90  $\mu$ rad; this is equivalent at a 500-km range to 115 m and 45 m, respectively.

The first and second stages of the three-stage LCLV fired only at low altitude (below 40 km) and were not expected to be visible in the ultraviolet from space. The LCLV third stage used a powerful solid-fuel rocket motor, the Aries, that contained aluminum in its fuel and was thus a good candidate for observation. It reached a 117-km altitude and was successfully detected and tracked by the UVPI from a range of 500 to 480 km.

The third-stage plume was successfully tracked for about 40 s, and 385 images of plume data (1/30th second each) were acquired by using the four plume-camera filters. The image quality and tracking accuracy were of sufficient quality to permit the superposition of images for plume radiance determination. Image superposition to enhance the signal level is needed for accurate radiometry because of the small telescope aperture.

The spectral radiance and spectral radiant intensities of the missile plume were extracted from these images. Absolute values are necessarily obtained on the basis of an assumed spectral shape, namely, one that is derived from a physical model of the plume as a nearly transparent stream of several micron-sized alumina particles at their melting points. This spectral shape is termed simply the reference model spectrum. A comparison of the results for the four UVPI filters indicates that the reference spectral shape is an accurate representation of the LCLV third-stage plume spectrum. However, the spectrum appeared to show an excess in the far UV,  $\lambda < 300$  nm, relative to that expected from the reference spectrum. This apparent UV excess, relative to the reference spectrum, is in agreement with data gathered on the Stryi flight [2], which also showed an apparent excess in the far UV relative to the reference spectrum. The LCLV data did show a weak but identifiable UV bright

outer region of the plume similar to the UV luminous outer region seen on the Strypi and other flights.

The time dependence of the plume central-region radiant intensity within each filter interval showed no pronounced trends or variations. Momentary, single-frame peaks that exceeded the range of normal statistical variation were detected. Whether these can be correlated with missile engine events or other sensors remains to be seen. A persistent cloud trail was seen in the tracker camera just prior to burnout.

The tracker camera, within its relatively limited resolution, obtained radiant intensity data to 450-nm wavelength. These data, taken with the plume camera data in the 195 to 350-nm range, support the conclusion that the central-region spectrum is quite close to the reference model, with some relative excess in the far UV.

This base of UV LCLV radiometric data is a foundation for further analysis to yield refined interpretations and evaluation. Comparison with models, with data from sensors on other platforms, and with data from other test flights will also yield improved radiometric results and an enhanced phenomenological understanding of UV emission by solid rocket motors in the upper atmosphere.



## **UVPI IMAGING FROM THE LACE SATELLITE: THE LOW COST LAUNCH VEHICLE (LCLV) ROCKET PLUME**

### **1.0 INTRODUCTION**

#### **1.1 Background**

The Ultraviolet Plume Instrument (UVPI) carried aboard the Low-power Atmospheric Compensation Experiment (LACE) satellite launched in February 1990 was designed to collect rocket plume imagery in the ultraviolet band. An LCLV three-stage solid-fuel rocket was selected for one in a series of tests. The overall objective of the observation was to gather UV data at moderate altitude, about 100 km, from space to enhance the current level of understanding of plume physics and chemistry and to help answer questions about radiance, spatial extent, and temporal variability of plumes. A number of more specific objectives are listed in Section 1.3, which describes the LCLV mission plan.

#### **1.2 UVPI Capability**

The Ultraviolet Plume Instrument (UVPI) is carried aboard the Low-power Atmospheric Compensation Experiment (LACE) spacecraft. The UVPI's mission is to collect images of rocket plumes in the ultraviolet waveband and to collect background image data on Earth, Earth's limb, and celestial objects. Background object imagery already collected with the UVPI includes the day and night Earth limb air glow, aurora, sunlit and moonlit clouds, solid Earth scenes with varying solar illumination, cities, and stars. A detailed description of UVPI is found in the UVPI description and data methodology report [1] and in the Strypi plume report [2].

The UVPI sensor head assembly [3,4] contains two coaligned camera systems that are used in concert to acquire the object of interest, control UVPI, and acquire UVPI images and radiometric data. The two camera systems are the tracker camera and the plume camera; these are discussed briefly below. The two cameras share a fixed 10-cm diameter Cassegrain telescope that uses a gimbaled plane steering mirror to view a field of regard, which is a 50°-half-angle cone around the nadir. In addition, UVPI contains a second plane mirror on the instrument door. The mirror can be set at an angle of approximately 45° relative to the nadir and used in conjunction with the steering mirror to view Earth's limb and stars near the limb. The configuration of the UVPI and the radiometric response of UVPI are discussed in Ref. 1 and 2; characteristics of the UVPI were previously reported [4,5].

The tracker camera is an intensified charge-coupled device (CCD) camera that is sensitive over a wide wavelength range, extending from 255 to 450 nm. Figure 1 shows the overall response of the tracker camera as a function of wavelength, including the effects of the bandpass filter in the camera system, the photocathode response, and the other optical elements. This camera has a relatively wide total field of view (1.98° by 2.60°) and images over this full field of view can be recorded at a 5-Hz image rate. The tracker camera can also be operated in a mode where the transmitted field of view is restricted to the central 17% of the full field of view and the image rate is increased to 30 Hz. The intensifier gain and the exposure time of the camera can be controlled to provide a radiometric dynamic range greater than  $10^6$ .

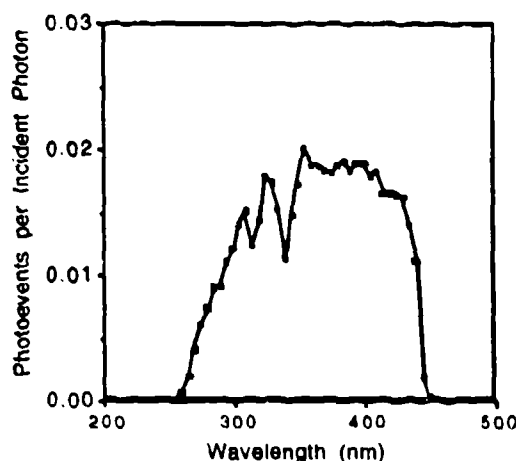


Fig. 1 - Tracker camera: net quantum efficiency curve

The plume camera is also an intensified CCD camera operating in the ultraviolet. The plume-camera optical train contains a filter wheel with four selectable filters that have bandpasses within the range 195 to 350 nm. Figure 2 shows the overall response of the plume camera for each of these four filters. The plume camera has a total field of view of  $0.184^\circ$  by  $0.137^\circ$  with a correspondingly higher resolution than can be achieved by the tracker camera. Plume camera images can be recorded or transmitted at either 5 or 30 Hz, depending on the desired field of view. The intensifier gain can be controlled to provide a radiometric dynamic range greater than  $10^6$ .

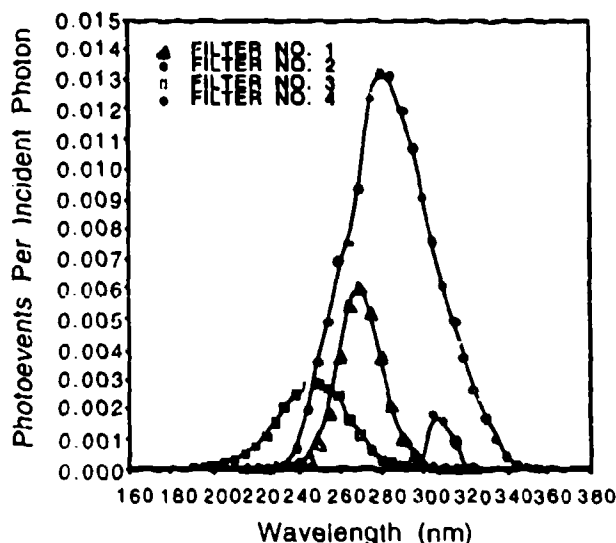


Fig. 2 - Plume camera: net quantum efficiency curves

Table 1 summarizes the instrument characteristics and telemetry rates. Note that the field of view per pixel values are revisions of those listed in the data methodology report [1] and in the Strypi plume report [2].

Table 1 - Instrument Characteristics

Parameter	Tracker Camera	Plume Camera
Shared telescope type	Maksutov Cassegrain	Maksutov Cassegrain
Telescope diameter	10 cm	10 cm
Focal length	60 cm	600 cm
Field of regard	100° x 97°	100° x 97°
Field of view (max)	2.60° x 1.98°	.184° x .137°
Field of view per pixel	180.5 x 143.9 $\mu$ rad	12.8 x 10.0 $\mu$ rad
Pixel footprint @ 500 km	90 x 72 m	6.4 x 5.0 m
System resolution (FWHM)	220 to 250 $\mu$ rad	80 to 100 $\mu$ rad
Spectral region	255-450 nm	195-350 nm
Number of filters	1	4
Photocathode material	Bialkali	Cs Te
Time for filter change	n/a	1.7 s
Digitization	8 bits/pixel	8 bits/pixel
Digital data rate	2.5 Mbps	2.5 Mbps
Image rate: normal	5 per second	5 per second
zoom*	30 per second	30 per second
Pixels: normal	251 x 240	251 x 240
zoom	91 x 112	91 x 112
Pixel exposure time	.16 to 33.3 ms	33 ms
Frames integrated	n/a	1 - 6
Exposure range	>10 <sup>6</sup>	>10 <sup>6</sup>

\*Reduced field of view.

### 1.3 Scientific Objectives for UVPI

The primary goal of the LCLV mission [6,7] for UVPI was to collect spatially resolved, radiometric UV plume data for the third stage of the rocket. This was to be accomplished by using UVPI's capabilities for tracking and imaging a moving target at long range. The plume-camera filters were cycled to vary the wavebands. Emphasis was placed on the mid-UV bands because these data can be obtained only from a space-based sensor, and because the bands have the best potential for high signal-to-background contrast. Pointing accuracy was optimized because this simplifies registration of images when superposed, a necessary procedure for improving statistics. The UVPI observation was coordinated with ground observations to provide infrared and visible band data as an important supplement to the UV data.

A secondary goal was to observe any serendipitous special events such as transients, puffs, chuffing, clouds, or contrails. The brightness, size, frequency, and persistence of such phenomena would provide useful information.

Specific objectives of the mission related to UVPI data are given in the following subsections. They revolve around a number of questions concerning plume radiance, spatial extent, temporal variability, and spectral shape of the UV emissions [8, 9]. The objectives are grouped under headings reflecting these subjects.

#### 1.3.1 Specific Objectives Related to Radiometrics

The following four objectives are basic to those listed in the subsequent subsections.

- Obtain isoradiance contours for multiple plume-camera bandpasses for the LCLV third-stage plume.

- Obtain radiant intensity measurements in multiple plume-camera bandpasses for the LCI V third-stage plume based on the entire field of view of the plume camera and on a subregion corresponding approximately to a plume core.
- Compare radiometric measurements for the LCLV third-stage plume with other measurements or expectations.
- Provide radiometric measurements for nonplume, transient phenomena, if any.

#### 1.3.2 *Specific Objectives Related to Spatial Features*

- Obtain the length of the LCLV third-stage plume core, and investigate implications for cooling rate and emissivity of particles.
- Obtain the shape of the shock boundary/mixing layer of the rocket.
- Identify asymmetries in plume shape, and investigate angle-of-attack and uneven burning as possible causes.

#### 1.3.3 *Specific Objectives Related to Temporal Features*

- Identify temporal trends in radiometrics, and investigate possible dependence on rocket velocity and altitude.
- Investigate radiometric fluctuations to determine whether short-term variations in brightness are observed.
- Identify changes with time in the shape of the plumes' outer regions, if any, and investigate possible dependence on rocket velocity or altitude.
- Identify persistence and cumulative effects, if any, in plumes or nonplume phenomena.

#### 1.3.4 *Specific Objectives Related to Spectral Features*

- Compare the shape of the plume central region's emission spectrum from the multiple bandpass measurements with a reference spectral shape and spectral shape determinations based on other sensors.
- Relate tracker-camera measurements to visible and infrared measurements made by other sensors.
- Characterize the emission spectrum for the plumes' outer regions, if any.

### 1.4 **Experiment Concept**

#### 1.4.1 *LCLV Trajectory and Description*

The LCLV Developmental Launch Vehicle was a three-stage rocket with the Talos and Sergeant as the first and second stage, respectively, and a high-energy Aries motor as the third stage (Fig. 3). The Aries motor had an average thrust of about 17,000 lb. The propellant for the Aries was a composite that included ammonium perchlorate, powdered aluminum, and rubber binder. The propellant had an aluminum loading of roughly 20% and a flame temperature of approximately 3200 K. Table 2 summarizes LCLV rocket motor characteristics.

The LCLV rocket was designed to give low-cost access to space at an altitude of about 120 km. The planned trajectory was high, with a burnout altitude for the last stage of about 117 km. The trajectory called for LCLV to be launched from Wallops Island, Virginia, fly in an east-northeast direction, and land in the Atlantic Ocean. The Talos and Sergeant stages were to burn out at 7 and 47 s after launch, respectively, followed by a coast period of 23 s. The Aries stage was to burn 59 s.

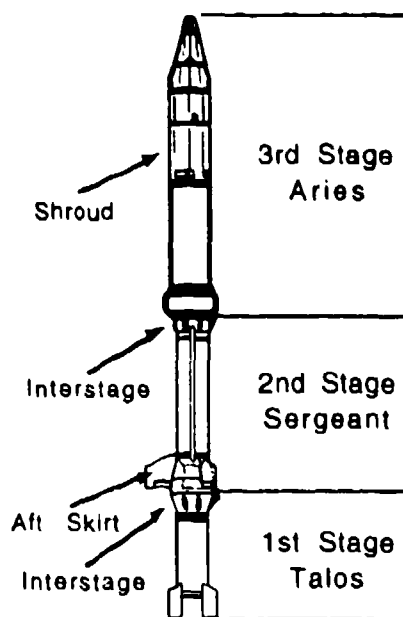


Fig. 3 - LCLV three-stage rocket

Table 2 - Summary Of LCLV Flight

Stage (Solids)	Thrust (lb)	UVPI/LCLV Observation	
		Ignition/Burnout Time (s)	Ignition/Burnout Altitude (km)
Talos	104000	0 - 7	0 - 1.0
Sergeant	43000	11 - 47	2.0 - 21.2
Aries	17000	70 - 129	33.6 - 112.8
Stage	Ignition/Burnout Range (km)	Ignition/Burnout Aspect Angle (deg)	Ignition/Burnout Velocity (km/s)
Talos *	836 - 800	59.5 - 60.3	0.0 - 0.27
Sergeant **	778 - 610	60.3 - 40.8	0.21 - 0.68
Aries	528 - 497	32.8 - 37.8	0.44 - 2.66

\* Not observed

\*\* Partially observed

Based on information from Ref. 7.

#### 1.4.2 Radiometrics

The LCLV third stage, or Aries, rocket motor propellant is a composite with a composition of approximately 70% oxidizer, 20% powdered aluminum, and a small amount of hydrocarbon binder. The combustion products for the Aries rocket motor are  $\text{Al}_2\text{O}_3$  particles,  $\text{H}_2\text{O}$ ,  $\text{CO}$ ,  $\text{CO}_2$ , and other gases. The temperature inside the rocket motor chamber is typically 3200 K, which is hot enough to melt the  $\text{Al}_2\text{O}_3$  (melting point 2320 K) but not hot enough to vaporize it (boiling point approximately 3700 K). As the exhaust exits the rocket nozzle it cools, and the  $\text{Al}_2\text{O}_3$  begins to solidify. The temperature of the exhaust decreases further as it moves away from the rocket [7].

In the ultraviolet, the emission from the plume central regions of these rocket motors is expected to be dominated by thermal emission from hot particles of  $\text{Al}_2\text{O}_3$ . In a simplified model, the temperature of the  $\text{Al}_2\text{O}_3$  particles is taken to be constant at the solidification temperature of 2320 K because the latent heat of fusion causes the temperature of the particles to pause at this point as they cool. In the outer region, other thermophysical processes can produce emission bands arising from exhaust gases or atmospheric constituents, and these will contribute to the spectrum.

Even in the simplified model, in which the  $\text{Al}_2\text{O}_3$  particles in the plume are assumed to be at a uniform temperature of 2320 K, the plume emission is different from a 2320 K blackbody for two primary reasons. First, the plume consists of a rather transparent cloud of particles, and the total emission from the cloud is substantially less than would be the case from a solid object the same size as the plume. Second, the  $\text{Al}_2\text{O}_3$  particles are typically a few microns in size and are inefficient emitters of visible and longer wavelengths.

The rocket's emission was estimated for all four filter bandpasses of the UVPI's plume camera by using a modified version of the CHARM 1.4 code. The results are given in Table 3. This information was used to determine the desired sequence of the plume-camera filters for the LCLV observation.

Table 3 - Expected Intensities for LCLV Third Stage

Filter	W/sr	Photoevents/Frame
PC-1	120	129
PC-2	75.4	134
PC-3	31.7	26.6
PC-4	367	2100

Filter PC-4 was selected to begin the observation of the LCLV because its wider bandpass would provide the brightest signature. Filter PC-4 responds to wavelengths longer than 300 nm that pass through the ozone layer. Its primary purpose is to obtain a few seconds of data for comparison with that from ground-based and airborne sensors. Filters PC-1 and PC-3 observe wavelengths that do not pass through the ozone layer. Thus, they cannot be observed from the ground. Use of these filters would provide unique data. Since the UVPI plume camera filters must be cycled in sequence, a few seconds of data using filter PC-2 would be collected to complete the data set, even though PC-2 passes wavelengths that can be observed from the ground.

## 2.0 LCLV OBSERVATION AND INSTRUMENT PERFORMANCE

### 2.1 Observation Scenario

The LCLV plume observation by UVPI was highly successful because of a well coordinated effort by the LACE team and the cooperative effort by the LCLV launch team.

The following is the sequence of events during this observation. Figure 4 shows the LACE ground track during the encounter.

The LCLV launch occurred only 1.2 s later than the requested launch time of 07:29:20 GMT. After the launch time was announced by launch control, a new latest rocket pointing function was computed and transmitted to the spacecraft. UVPI pointed to the LCLV trajectory during the second-stage burn. A bright target appeared in the tracker camera's FOV using a gain of 9. The acquire command was sent immediately, and UVPI was able to track the second stage for about 10 s before it burned out (review of the data indicated no noticeable signal in the plume camera with the PC-4 filter in place). Then, before the third-stage ignition, the acquire command was sent and UVPI

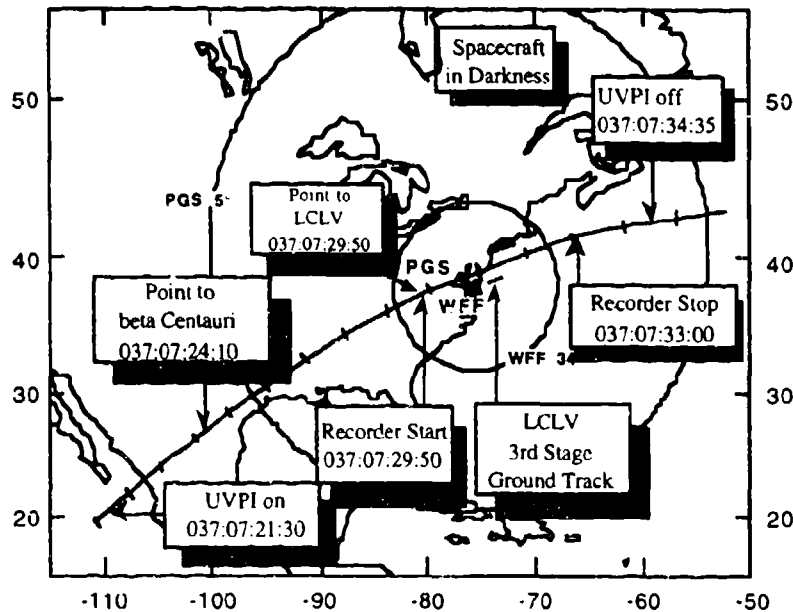


Fig. 4 - Ground track of LACE satellite during LCLV flight

acquired the target almost instantly at ignition. At the third-stage ignition, launch control gave the count-up sequence over the communications network. This count-up sequence guided the encounter manager to instruct the console operator to cycle through the filter sequence of 4, 3, 2, and 1 in a timely manner. Data in the plume camera were collected with a nominal gain of 9, 13, 12, and 11 corresponding to the filters 4, 3, 2, and 1, respectively. The tracker camera, on the other hand, showed a gain of 5.

After the third-stage burnout, a noticeably bright, elongated source appeared in the tracker camera. The slender shaped source spanned almost the entire tracker camera FOV in the horizontal direction. The bright source was identified as a persistent cloud trail from the LCLV third stage enhanced by moonlight.

The timeline in UVPI mission time (UMT) for the observation is shown in Table 4.

Figure 5 graphs time vs frame number. Time in Fig. 5 is chosen such that zero time corresponds to the LCLV rocket liftoff time, 07:29:20.3 GMT. For this observation, the linear equation for time is:  $TIME = (FRAME - 13213) / 29.877$ . Note that there is 1/30th of a second between frames.

## 2.2 LCLV Performance Summary

The overall performance of the LCLV rocket was nominal. Appendix A provides flight telemetry data for the LCLV trajectory. Figure 6 shows the thrust profile of the second and third stages of the LCLV flight. Figure 7 shows the altitude and velocity for the LCLV trajectory. Figure 8 shows the angle of attack of the LCLV during the later portion of the flight.

## 2.3 Encounter Geometry

From the post-launch telemetry data for the LCLV vehicle's position and attitude, the range and aspect angle vs time after launch were computed (Fig. 9). The aspect angle is defined as the angle between the line-of-sight vector from UVPI to the target point and the longitudinal axis of the rocket. Zero degree aspect angle means looking "nose on" and 180° means looking up the nozzle. The best range/aspect angle combination occurred toward the end of the third-stage burn.

Table 4 - Timeline of LCLV Observation

Timeline UMT	Frame	Event
07:22:18	545	Begin dark field data collection
07:22:38	1126	End dark field data collection
07:25:29	6256	Begin <i>beta Centauri</i> observation
07:27:34	10006	Begin <i>beta Centauri</i> data collection
07:28:20	11396	End <i>beta Centauri</i> data collection
07:29:36	13658	End <i>beta Centauri</i> observation
07:29:52	14138	Begin Stage 2 observation
07:30:05	14541	End Stage 2 observation
07:30:33	15364	Begin Stage 3 observation
07:30:43	15647	Begin Stage 3 data collection
07:31:30	17067	End Stage 3 data collection
07:31:30	17067	End Stage 3 observation
07:32:11	18301	Begin <i>zeta Centauri</i> observation
07:32:32	18944	Begin <i>zeta Centauri</i> data collection
07:33:32	20721	End <i>zeta Centauri</i> data collection
07:34:21	22198	End <i>zeta Centauri</i> observation

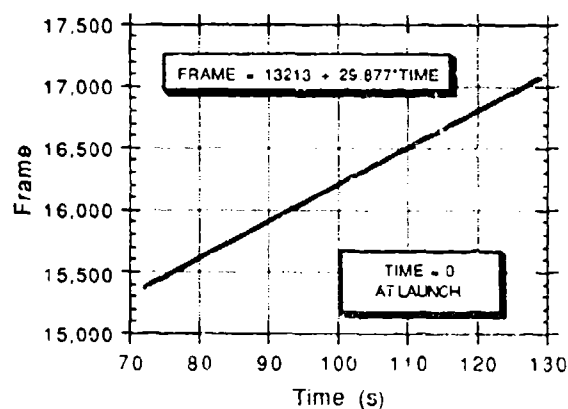


Fig. 5 - Telemetry frame vs time after liftoff

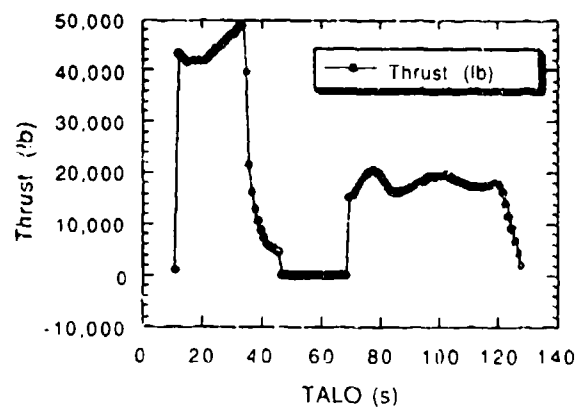


Fig. 6 - LCLV thrust profile



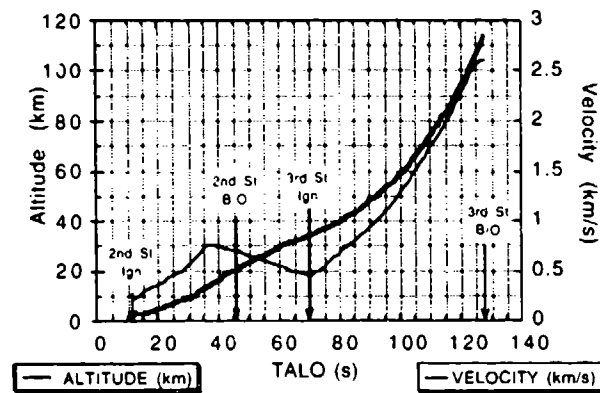


Fig. 7 - LCLV altitude and velocity profiles

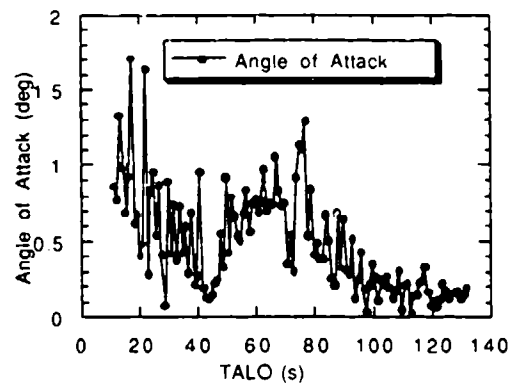


Fig. 8 - LCLV angle of attack profile

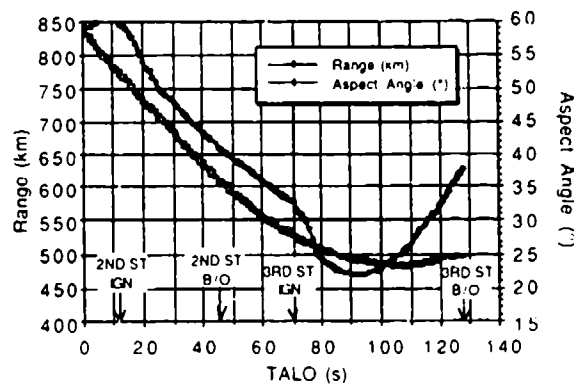


Fig. 9 - Range and aspect angle

Figure 10 shows the percent vignetting and the orientation angle of the rocket body in the tracker camera's FOV. At the LCLV third-stage ignition, the plume intensity signal was essentially clear of vignetting and remained so throughout the data collection period. The orientation angle in Fig. 10 is used to assist with the radiometric analysis of the plume. This angle is defined as the angle between the tracker camera's horizontal axis and the projection of the rocket body onto the focal plane of the tracker camera.

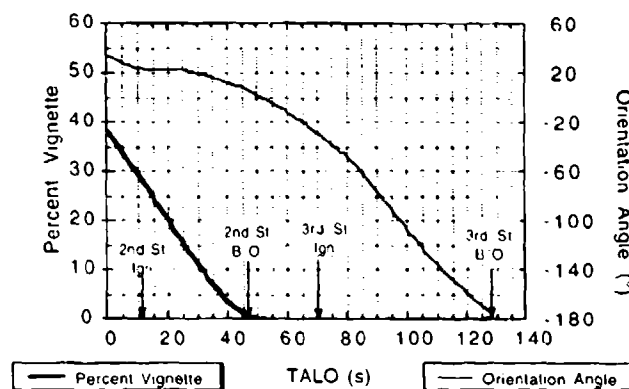


Fig. 10 - UVPI-LCLV encounter: percent vignetting and image orientation angle

### 3.0 EXTRACTION OF RADIOMETRIC QUANTITIES

Three levels of data reduction are useful for any radiometric experiment. At the first level, data are merely reduced to instrument readings or counts at the image plane; at the second level, instrument readings are converted by manipulating instrument-specific factors, which may be approximate, into approximate measures of physical quantities, e.g., radiance, with no assumed spectral shape for the source being used; at the third level of reduction, a spectral shape is assumed to reduce data and present it.

A spectral shape must be assumed because instrument efficiency is a function of wavelength within each band. Therefore, the spectral distribution of incident photons is needed to provide the appropriate weighting at each wavelength within the passband of integrated response. Since the spectral shape is not known from the data, a spectral shape must be assumed to determine this weighted distribution. Once a spectral shape has been assumed, the number of photoevents measured is used to infer the amplitude or intensity of the emission with that spectral shape.

#### 3.1 Data Calibration Procedure

The raw image data transmitted from the satellite are in the form of arrays of 8-bit binary numbers  $Q_k$  representing the intensity of light falling on the  $k$ th pixel of the CCD. From  $Q_k$ , an estimate of the number of photoevents  $P_k$  occurring at the corresponding photocathode pixel during the image frame can be obtained by using

$$P_k = (Q_k - D_k) / (U_k G_g), \quad (1)$$

where

$G_g$  is the gain conversion factor for gain step  $g$ , i.e., the value of  $Q_k$  for a single photoevent, assumed to be the same for all pixels  $k$ ;

$D_k$  is the measured dark value for the  $k$ th pixel; and

$U_k$  is the measured gain nonuniformity correction factor for the  $k$ th pixel.

The pulse height distribution of the image intensifier will cause noninteger values for  $P_k$ . The conversion of CCD response peaks to integral photoevent counts is possible only on the weakest images because of the overlap of photoevent images. Hence,  $P_k$  values are treated as continuous variables. The  $G_g$ ,  $D_k$ , and  $U_k$  factors are discussed in detail with the data calibration procedure in Section 2.0 of Ref. 1.

### 3.1.1 Discrimination of Photoevents

When a single photoevent is generated in the microchannel plate (MCP) of the UVPI plume camera, it is registered as a spatial distribution of charge in the CCD. In general, a photoevent is registered within a  $3 \times 3$  pixel region and the largest response is at the center pixel. Note that the blurring of a single photoevent is a relatively small component of the overall system point spread function.

When UVPI is looking at a dim source, compared to the instrument sensitivity, the instrument gain is automatically set high, for example, gain 13. At these high gains the calibration procedure, i.e., the estimation of photoevents from the measured digital number (DN), is sensitive to any mismatch between the estimated dark field level used for calibration and the actual dark field level. Although a small bias error in the dark field estimate would have a small impact on the photoevent estimate for a single pixel, it could have a large impact on the results when summing the contribution from large groups of pixels. Hence, for dim signal levels such as the LCLV rocket plume, a statistical discrimination scheme was developed that fixes the probability of false alarm for every pixel. In the context of calibrating UVPI data, a false alarm occurs when the noise in a pixel that contains no target is large enough to be considered part of a photoevent.

Working with the already calibrated images, the discrimination scheme consists of estimating a statistical decision threshold for each image. The threshold is given in terms of the background mean, standard deviation, and the accepted probability of false alarm. Estimates for each image of the background mean and variance are made by using 4 image blocks located at each corner of the image and with dimensions of  $8 \times 8$  pixels. The estimated threshold will exactly correspond to a probability of false alarm  $PF$  if the following assumptions hold [10]:

- the local mean and local variance background statistics are the same over the whole focal plan array, and
- the density function of the background follows a Gaussian distribution.

Mathematically the decision threshold is given by

$$t' = \mu + \sigma \cdot t'$$

where:

$\mu$  is the estimated background mean,

$\sigma$  is the estimated background standard deviation, and

$t'$  must satisfy the integral equation

$$PF = 1 - \text{erfc}(t').$$

where the standard complementary error function was used [10].

All the plume camera images that were used in this report to estimate radiance or radiant intensities were subjected to the above discrimination scheme using a probability of false alarm of 0.0001. False alarms were in fact observed in approximately 1 out of every 10000 pixels, indicating that the two assumptions stated above are generally representative of this data. Recalling that a photoevent may spread over a  $3 \times 3$  pixel region; immediate neighbors are also included as possible signal contributors for all those pixels where a photoevent took place. A new estimate for the number of photoevents from the  $k$ th pixel was computed based on the following rule,

$$P_k = P_k - \mu \text{ if } P_k > \mu \text{ or } 0, \text{ otherwise.}$$

The rule states that if any pixel in the local neighborhood of the  $k$ th pixel exceeds  $\mu$  then the value at the  $k$ th pixel is adjusted to be the maximum of zero or  $P_k - \mu$ . Thus, pixels containing no photoevent contribution are set to exactly zero, thereby eliminating the possibility of an "erroneous" contribution resulting from uncertainties in the dark field estimate for that pixel. This adjustment can be significant when large numbers of pixels contain no photoevents, i.e., few photoevents per image.

Figures 11 and 12 show a composite image created with no statistical discrimination and a composite image created by using statistical discrimination.

### 3.2 Relation of Photoevents to Source Radiance

Presumably, the photoevents at the image plane are a result of a radiation source in the field of view. If the radiation source is isotropic and uniform over an emitting region of area  $A_s$ , then an expression for the photon flux  $\phi_{in}$ , incident on the face of the telescope in photons/second, is

$$\phi_{in} = (A_s \Omega_s / hc) \int \lambda L(\lambda) d\lambda, \quad (2)$$

where

- $L(\lambda)$  is source spectral radiance in  $\text{W/m}^2\text{-nm-sr}$ ,
- $A_s$  is area of emitting region,
- $\Omega_s$  is solid angle of emission subtended by the telescope,
- $h$  is Planck's constant,
- $c$  is speed of light.

The factor  $\lambda/hc$  converts the spectral radiance  $L(\lambda)$ , to a photon radiance (photons/s- $\text{m}^2\text{-nm-sr}$ ).

By setting the size of the emitting region equal to the footprint area of a pixel, the following reciprocity relation results:

$$A_s \Omega_s = A_s A_c / R^2 = A_c \Omega_p,$$

where

- $A_c$  is system aperture area,
- $\Omega_p$  is pixel field of view,
- $R$  is range from the detector to the emitting region.

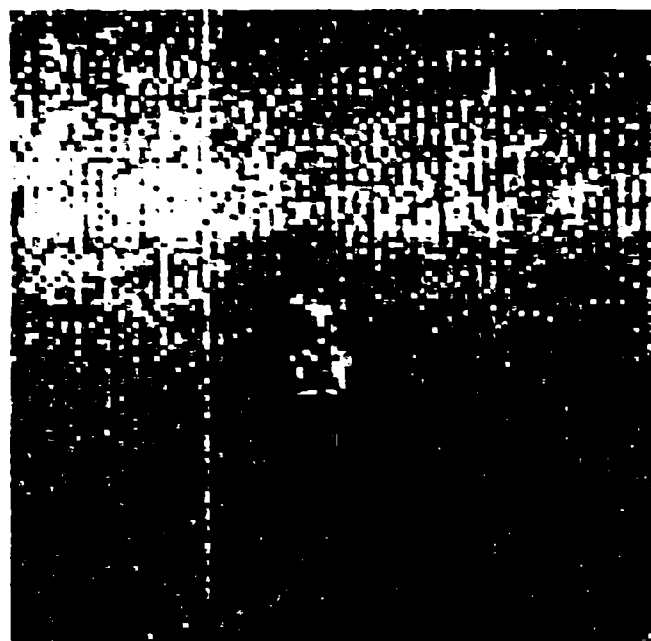


Fig. 11 - Composite image using no statistical discrimination



Fig. 12 - Composite image using statistical discrimination

The general expression for the number of photoevents  $P_k$  in pixel  $k$  at the image plane due to an emitting source of spectral radiance  $L(\lambda)$  filling the pixel field of view is then given by [11]:

$$P_k = (A_c \Omega_p \tau / hc) \int \lambda Q(\lambda) L(\lambda) d\lambda, \quad (3)$$

where

$\tau$  is exposure time, and

$Q(\lambda)$  is wavelength-dependent photoelectronic conversion efficiency, or net quantum efficiency, of the optics and detector.

In general, the exposure time  $\tau$  is 1/30th s for the plume camera and variable to a maximum of 1/30th s for the tracker camera. The pixel field of view  $\Omega_p$  is 12.8 by 10.0  $\mu\text{rad} = 1.28 \times 10^{-10}$  sr for the plume camera and 180.5 by 143.9  $\mu\text{rad} = 2.60 \times 10^{-8}$  sr for the tracker camera. At the typical range of 500 km, these pixel fields of view correspond to 6.4 by 5.0 m and 90 by 72 m, respectively.

For further insight into the relationship of photoevents to source radiance, several forms of approximation can be helpful. Equation (3) can be rearranged as follows

$$\int \lambda Q(\lambda) L(\lambda) d\lambda = (P_k / \tau) (hc / A_c \Omega_p). \quad (4)$$

Now note that the integral on the left is similar to the source radiance integral  $\int L(\lambda) d\lambda$  except for the  $\lambda$  and  $Q(\lambda)$  factors. One quick and simple approximation involves substituting constant values for  $\lambda$  and  $Q(\lambda)$  and allowing them to come out from under the integral and move to the right side. For example,  $\lambda_0 = (\lambda_1 + \lambda_2)/2$  and  $Q_0 = Q_{\max}/2$  provide estimated "average" values that allow reduction of the integral to an approximate radiance. The sensitivity of this approximate radiance to  $\lambda$  and  $Q(\lambda)$  for various assumed spectra is discussed in Section 4.6 of Ref. 1. A more frequently used approximation (the peak normalized radiance) is discussed in the next section.

### 3.3 The Peak Normalized Radiance Approximation

The second level of data reduction involves manipulation of instrument-specific factors to obtain approximate measures of radiance and other similar quantities. One common method is called peak normalization in which both sides of Eq. (4) are divided by the quantities  $\lambda_m$  and  $Q(\lambda_m)$ .  $\lambda_m$  is defined as the wavelength of peak net quantum efficiency and  $Q(\lambda_m)$  is the peak net quantum efficiency. The result is called the peak normalized radiance  $L_{pn}$ , which is defined as

$$L_{pn} = \int \lambda Q(\lambda) L(\lambda) d\lambda / [\lambda_m Q(\lambda_m)]. \quad (5)$$

In practice, the evaluation of  $L_{pn}$  is based on the measured  $P_k$ , using:

$$L_{pn} = (P_k / \tau) (hc / \lambda_m) / [A_c \Omega_p Q(\lambda_m)]. \quad (6)$$

Table 5 gives the values of  $\lambda_m$ ,  $Q(\lambda_m)$ , and  $\lambda_m Q(\lambda_m)$  for each of the filters; the quantity  $hc / A_c \Omega_p = 1.98 \times 10^{-8}$  J-nm/cm<sup>2</sup>·sr.

Table 5 - Plume Camera Filter,  $\lambda_m$ , and Peak Quantum Efficiency

Filter	$\lambda_m(\text{nm})$	$Q(\lambda_m)$	$\lambda_m Q(\lambda_m)$ (nm)
Plume PC-1	270	.00606	1.64
Plume PC-2	305	.00182	0.555
Plume PC-3	250	.00284	0.710
Plume PC-4	280	.0131	3.67
Tracker	355	.0200	7.10

Even though Eq. (5) is an exact expression, it is not a true radiance because the integral contains terms other than  $L(\lambda)$ .  $L_{pn}$  approaches the true radiance as  $[\lambda Q(\lambda)/\lambda_m Q(\lambda_m)]$  approaches 1. For UVPI,  $\lambda/\lambda_m$  is usually about equal to 1, but  $Q(\lambda)/Q(\lambda_m) \ll 1$  for some of the bell-shaped efficiency curves like PC-1 and PC-3 with extended, low-efficiency wings. On the other hand, efficiency curves for PC-2 and the tracker camera are more box-like and  $Q/Q(\lambda_m)$  is close to one. This is discussed further in Ref. 1.

Table 6 presents peak normalized radiance values and reference spectrum values obtained from an observation of the LCLV third-stage rocket by using measured  $P_k$  from the brightest pixel only. The ratio of the two radiances is included in the last column. The peak normalized approximation underestimates the reference spectrum result by a factor of 5 or more for filters PC-1 and PC-3 because of the low-efficiency wings. On the other hand,  $L_{pn}$  is only low by about a factor of two for PC-2.

Table 6 -  $P_k/\tau$  and  $L_{pn}$  for Brightest Pixel

Filter	$P_k/\tau$ (Photoevents/s)	$L_{pn}$ ( $\mu\text{W}/\text{sr}\cdot\text{cm}^2$ )	$L_e$ ( $\mu\text{W}/\text{sr}\cdot\text{cm}^2$ )	$L_{pn}/L_e$
Plume PC-1	$2.19 \times 10^1$	$2.65 \times 10^{-1}$	2.17	0.12
Plume PC-2	$1.70 \times 10^1$	$6.09 \times 10^{-1}$	1.06	0.58
Plume PC-3	8.19	$2.29 \times 10^{-1}$	1.07	0.21
Plume PC-4	$2.02 \times 10^2$	1.09	3.65	0.30

Thus, the peak normalized radiance is an approximate measure of the total radiance in the passband of the filter. A corrected radiance can be obtained if the true spectrum is used to evaluate the integral [12]. To better estimate the true in-band radiance, the approximate shape of the plume spectrum must be known.

### 3.4 Reference Spectrum for Aluminum-Loaded Propellants

The third level of data reduction requires the assumption of a spectrum of the emitting region. The amplitude of the assumed spectrum plays no role, but the shape acts as a weighting function within the passband to determine the distribution of photons as a function of wavelength. This is important because the instrument efficiency is different at each wavelength within a passband. Thus, the implied photon flux at the telescope face for a fixed measurement of photoevents  $P_k$  will depend on how the photons are distributed across that wavelength interval. What is needed is the spectral shape. Such a spectral shape is not provided by the instrument. Fortunately, previous measurements and theoretical predictions can aid in making the assumption, as explained below. The sensitivity of the resulting radiometric numbers to several different spectral shapes is discussed in Section 4.5 of Ref. 1.

The solid rocket motor under consideration contains powdered aluminum in its propellant. This aluminum is oxidized and emerges as an incandescent mist in the rocket exhaust. It is this mist of oxidized aluminum particles or droplets that emits much of the UV radiation seen by UVPI in the plume central region. This mist is optically thin. The plumes are, thus, partially transparent. Since the heat of fusion for aluminum oxide is very high and the rate of cooling for micron-sized particles is relatively low, the particles remain at their melting temperature roughly throughout the length of the plume. Thus, most of the light in the plume will be from this nearly transparent cloud of micron-sized  $\text{Al}_2\text{O}_3$  particles at their melting point, 2320 K.

The assumed spectral shape used is that of a 2300 K blackbody times an emissivity function  $\epsilon_{\text{Al}}(\lambda)$ , shown in Fig. 13 [13]. This emissivity curve is basically characteristic of hot alumina particles of the size found in rocket exhaust plumes [9].

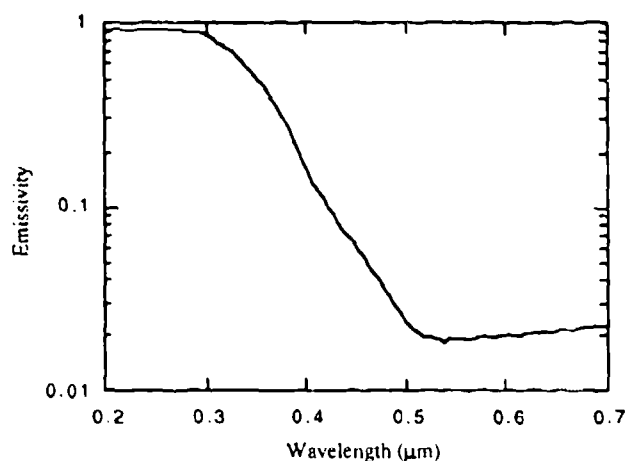


Fig. 13 - Emissivity curve for aluminum particles in rocket plumes

The resulting normalized spectral shape is fairly generic to all solid-fueled boosters with aluminum-loaded fuel and is termed the reference spectrum  $R(\lambda)$ . Mathematically,

$$R(\lambda) = \epsilon_{\text{Al}}(\lambda) L_{\text{BB}}(\lambda), \quad (7)$$

where  $L_{\text{BB}}(\lambda)$  is the 2300 K blackbody spectrum. The reference spectrum, compared to a blackbody spectrum, is shown in Fig. 14.

The spectral shape is a good approximation to actual rocket plume spectra as verified by on-board spectrometers looking back into rocket plumes [14].

### 3.5 Use of the Reference Spectrum to Calculate a Scaling Constant

Assuming that the reference spectrum  $R(\lambda)$  gives the proper spectral shape for  $L(\lambda)$  is equivalent to saying that  $L(\lambda)$  and  $R(\lambda)$  are related by a scaling constant  $\alpha$ , which is independent of  $\lambda$ :

$$\alpha = L(\lambda) / R(\lambda). \quad (8)$$

An expression for the scaling factor  $\alpha_k$  for a pixel can be obtained by first calculating the number of photoevents expected for the unscaled reference spectrum  $P'_k$  by using the expression:

$$P'_k = \left( A_c \Omega_p \tau / hc \right) \int \lambda Q(\lambda) R(\lambda) d\lambda, \quad (9)$$



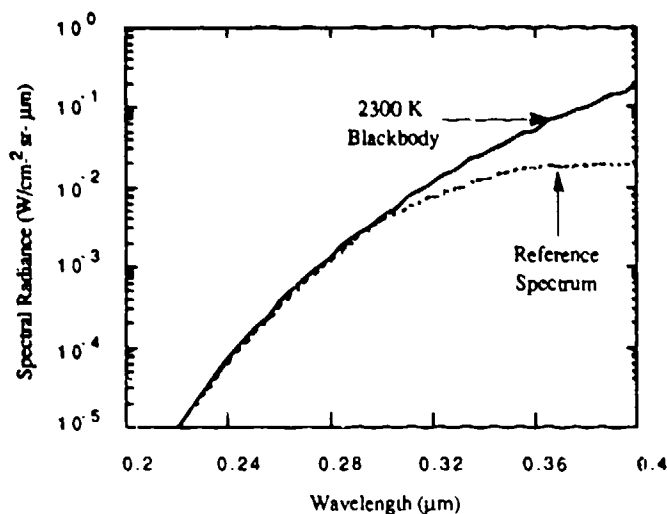


Fig. 14 - Assumed reference spectrum

where the calculated value is the same for all  $k$  (i.e.,  $k$  is superfluous). Then, deriving an expression for  $\alpha_k$  using the ratio of Eq. (3) to Eq. (9), namely:

$$\frac{P_k}{P'_k} = \frac{\int \lambda Q(\lambda) L(\lambda) d\lambda}{\int \lambda Q(\lambda) R(\lambda) d\lambda} = \frac{\alpha \int \lambda Q(\lambda) R(\lambda) d\lambda}{\int \lambda Q(\lambda) R(\lambda) d\lambda} = \alpha_k. \quad (10)$$

In practice,  $\alpha_k$  is estimated for each passband and for each pixel by comparing the measured value  $P_k$  to the calculated value  $P'_k$ :

$$\alpha_k = P_k / P'_k, \quad (11)$$

which gives an in-band, effective value of  $\alpha_k$  for that pixel. Actually, these plumes are optically thin and  $\alpha_k$ , in some sense, provides a measure of the optical thinness or density of emitters along the line of sight of that pixel.

After a value for  $\alpha$  is known, a source spectral radiance function  $L(\lambda)$  can be calculated by using Eq. (8) and, in turn, used to calculate in-band total radiance for the plume data in various filter bandpasses. All the radiometric values presented in this report can be obtained from the source function  $L(\lambda)$  defined by Eqs. (8) and (11). Table 7 gives values for  $P_k / \tau$  and  $P'_k / \tau$ , obtained as an average for the brightest pixel over several frames for the LCLV third-stage plume in the various filter bands.

Table 7 - Photoevents Per Second from LCLV Third-Stage Plume and Reference Spectrum Model for Brightest Pixel and Ratios of These Values

Filter (Plume)	$P_k / \tau$ (PE/s)	$P'_k / \tau$ (PE/s)	$\alpha_k$
PC-1	$2.19 \times 10^1$	$1.89 \times 10^3$	$1.16 \times 10^{-2}$
PC-2	$1.70 \times 10^1$	$1.95 \times 10^3$	$8.72 \times 10^{-3}$
PC-3	8.19	$3.71 \times 10^2$	$2.21 \times 10^{-2}$
PC-4	$2.02 \times 10^2$	$2.84 \times 10^4$	$7.11 \times 10^{-3}$

### 3.6 Centroid Wavelength Determination

The procedure above yields a function  $L(\lambda)$  describing the amplitude of the spectral shape that corresponds to the observed number of photoevents. Describing this function with a single numerical value is difficult, because of the extremely rapid variation of the spectral radiances. [This is evident in Figs. 17, 18, and 19 found in Section 4.] It is sometimes desirable to provide single numerical values of plume spectral radiance and spectral radiant intensity despite this rapid variation. This is achieved simply by taking  $L(\lambda)$  of Eq. (8) at a specific characteristic wavelength  $\lambda_c$  for each filter passband. This might have been selected to be the center of each filter passband, but this choice would neglect the shift in the effective response due to the spectrally varying source. A response centroid wavelength, weighted by the reference spectral function, was defined:

$$\lambda_c \equiv \int \lambda^2 R(\lambda) Q(\lambda) d\lambda / \int \lambda R(\lambda) Q(\lambda) d\lambda. \quad (12)$$

This describes the wavelength of average contribution to the UVPI response for each filter. These centroid wavelengths were computed for various spectral shapes and are shown in Table 8. The integrals of Eq. (12) were evaluated for Table 8 as discrete summations over the range of nonnegligible  $Q(\lambda)$ . *The numbers in parentheses under the exact reference spectrum values are the rounded values that are actually used throughout the report.*

Table 8 - Centroid Wavelength,  $\lambda_c$ , for Various Spectra

	PC-3 (nm)	PC-1 (nm)	PC-2 (nm)	PC-4 (nm)	Tracker (nm)
1800 K Blackbody	270.4	282.4	310.0	314.1	416.2
2300 K Blackbody	265.8	279.2	309.7	308.5	409.7
Reference Spectrum (Rounded)	265.8 (265)	279.1 (280)	309.6 (310)	306.4 (305)	389.4 (390)
Flat Spectrum	248.1	270.7	309.0	287.3	369.5
Peak Normalized	250.0	270.0	310.0	280.0	355.0

This is simply a means of selecting a nominal characteristic wavelength for describing the result of the fitting of the spectral shape to the instrument measurement as single numerical values. Other procedures could have been used to select a reference wavelength for describing the spectral radiance function. For example, the central wavelength for each filter could have been used and the numerical value of the fit function cited at those wavelengths. This would yield different values for the nominal spectral radiances, without changing the function  $L(\lambda)$  at all. In short, these single numerical values for the rapidly varying spectral radiometric parameters must be treated with caution.

### 3.7 Calculations of Radiance and Radiant Intensity

After the spectral radiance is known, the spectral integrals can be evaluated to obtain values for the radiance:

$$L_e \equiv \int_{\lambda_L}^{\lambda_U} L(\lambda) d\lambda = \alpha \int_{\lambda_L}^{\lambda_U} R(\lambda) d\lambda. \quad (13)$$

The units of  $L_e$  are (power)/(area)(solid angle), or  $\text{W/m}^2\text{-sr}$ . The evaluation of these integrals is limited to the nominal bandwidth of the pertinent filter. Note that the integrand of Eq. (13) does not include the response function  $Q(\lambda)$ , and therefore does not become small outside the filter passbands. The values obtained for  $L_e$  will depend very strongly on the limits of integration.

Conversion to radiant intensity can be achieved from the preceding expressions by multiplying by  $R^2\Omega_p$ , where  $R$  is the range to the source and  $\Omega_p$  is the pixel field of view. This is then summed over the pixels containing signal. This is equivalent to summing the apparent radiance or spectral radiance over the projected pixel area and attributing it to a point source within the field of view of the pixel. The spectral radiant intensity  $I(\lambda)$  and the radiant intensity  $I_e$  can be obtained directly from the corresponding expressions for the spectral radiance and radiance, Eqs. (8) and (13), respectively:

$$I(\lambda) = R^2\Omega_p L(\lambda) = R^2\Omega_p \alpha R(\lambda) \quad (14)$$

and

$$I_e \equiv \int_{\lambda_L}^{\lambda_U} I(\lambda) d\lambda = R^2\Omega_p L_e \quad (15)$$

The units of  $I(\lambda)$  are (power)/(spectral bandwidth)(solid angle), or  $\text{W/nm-sr}$ , and the units of  $I_e$  are (power)/(solid angle), or  $\text{W/sr}$ . As with the radiance, the radiant intensity is an integral across a limited portion of the spectrum defined by the nominal filter edges. The value so obtained is far smaller than would be obtained for the full spectrum radiant intensity and will also be very sensitive to the limits of integration chosen for Eq. (15).

### 3.8 Summary of Radiometric Conversion Constants

Table 9 summarizes the definitions of conversion constants most often encountered in calculating one radiometric quantity from another. Table 10 gives the specific values for the conversion constants based on the assumed reference spectrum. Any revised spectral shape assumption will lead to a different set of conversion constants. Table 11 lists the radiometric values corresponding to 1 photoevent/s. The radiant intensity values refer to a range of 500 km. The spectral radiance  $L(\lambda_c)$  and the radiance  $L_e$  values are based on a single photoevent/s per pixel. Any arbitrary number of photoevents measured in a particular pixel is multiplied by the value in the table to determine the radiance of the source in that pixel's field of view. The spectral radiant intensity  $I(\lambda_c)$  and radiant intensity  $I_e$  values are per pixel, even though these terms more often refer to the total number of photoevents measured in the entire plume image.

Note that the conversion constants associated with  $I(\lambda_c)$  and  $L(\lambda_c)$  use the rounded reference spectrum centroid wavelength values shown in parentheses in Table 8.

## 4.0 PLUME DATA

This section presents observed plume data. The data intervals used are defined in Section 4.1, and an overview of the intensity history for each camera is given in 4.2. Examples of single plume-camera images are given in 4.3. Composite images with corresponding contour plots for the defined data intervals for the plume and tracker cameras are presented in 4.4 and 4.5, respectively. Subsection 4.6 discusses the error in the radiometric observations. The concluding subsection, 4.7, discusses the noise-equivalent radiance for the UVPI.

Table 9 – Summary of Formulas Defining Conversion Constants

From	To	Op	Formula
$P_k/\tau$ (photoevents/s)	$\Phi_{in}$ (photons/s)	$\times C_1$	$C_1 = \frac{\int \lambda R(\lambda) d\lambda}{\int \lambda R(\lambda) Q(\lambda) d\lambda}$
$\Phi_{in}$ (photons/s)	$P_{in}$ (W)	$\times C_2$	$C_2 = \frac{hc \int R(\lambda) d\lambda}{\int \lambda R(\lambda) d\lambda}$
$P_{in}$ (W)	$I_e$ (W/sr)	$+C_3$	$C_3 = A_c/R^2$
$L_e$ (W/sr-cm <sup>2</sup> ) $I_e$ (W/sr)	$L(\lambda_c)$ (W/cm <sup>2</sup> -sr-nm) $I(\lambda_c)$ (W/sr-nm)	$+C_4$	$C_4 = \frac{\int \lambda L(\lambda) d\lambda}{L(\lambda_c)}$
$I_e$ (W/sr) $I(\lambda_c)$ (W/sr-nm)	$L_e$ (W/cm <sup>2</sup> -sr) $L(\lambda_c)$ (W/cm <sup>2</sup> -sr-nm)	$+C_5$	$C_5 = R^2 \Omega_p$

Table 10 – Conversion Constants for the Reference Spectrum

Constant	Units	PC-3 ( $\lambda_c = 265$ nm)	PC-1 ( $\lambda_c = 280$ nm)	PC-2 ( $\lambda_c = 310$ nm)	PC-4 ( $\lambda_c = 305$ nm)	Tracker ( $\lambda_c = 390$ nm)
$C_1$	photons/photoevent	1840	1510	976	294	66.2
$C_2$	joules/photon	$7.11 \times 10^{-19}$	$6.61 \times 10^{-19}$	$6.41 \times 10^{-19}$	$6.19 \times 10^{-19}$	$5.11 \times 10^{-19}$
$C_3$	steradians	$3.12 \times 10^{-14}$	$3.12 \times 10^{-14}$	$3.12 \times 10^{-14}$	$3.12 \times 10^{-14}$	$3.12 \times 10^{-14}$
$C_4$	nm	104.5	150.2	20.4	105.5	125.2
$C_5$	cm <sup>2</sup>	$32.0 \times 10^4$	$32.0 \times 10^4$	$32.0 \times 10^4$	$32.0 \times 10^4$	$6493 \times 10^4$

Table 11 – Radiometric Values for One Photoevent Per Second

Units	PC-3 ( $\lambda_c=265$ nm)	PC-1 ( $\lambda_c=280$ nm)	PC-2 ( $\lambda_c=310$ nm)	PC-4 ( $\lambda_c=305$ nm)	Tracker ( $\lambda_c=390$ nm)
$P_k/\tau$ (photoevents/s)	1	1	1	1	1
$\Phi_{in}$ (photons/s)	1840	1510	976	294	66.2
$P_{in}$ (W)	$1.31 \times 10^{-15}$	$9.95 \times 10^{-16}$	$6.26 \times 10^{-16}$	$1.82 \times 10^{-16}$	$3.38 \times 10^{-17}$
$I_e$ (W/sr)	$4.16 \times 10^{-2}$	$3.17 \times 10^{-2}$	$1.99 \times 10^{-2}$	$5.80 \times 10^{-3}$	$.08 \times 10^{-3}$
$I(\lambda_c)$ (W/sr-nm)	$3.96 \times 10^{-4}$	$2.11 \times 10^{-4}$	$9.76 \times 10^{-4}$	$5.50 \times 10^{-5}$	$8.60 \times 10^{-6}$
$L_e$ (W/sr-cm <sup>2</sup> )	$1.30 \times 10^{-7}$	$9.91 \times 10^{-8}$	$6.22 \times 10^{-8}$	$1.81 \times 10^{-8}$	$1.66 \times 10^{-11}$
$L(\lambda_c)$ (W/sr-cm <sup>2</sup> -nm)	$1.24 \times 10^{-9}$	$6.59 \times 10^{-10}$	$3.05 \times 10^{-9}$	$1.72 \times 10^{-10}$	$1.32 \times 10^{-13}$

## 4.1 Data Intervals

### 4.1.1 Description of Intervals

Table 12 summarizes the LCLV third-stage data intervals used in this report and the number of plume-camera images and tracker-camera images analyzed in each interval. Table 13 reports important calibration parameters associated with the intervals. The UVPI-LCLV range is used to determine source radiant intensity, as discussed in 4.2. The image angle variation associated with a sequence of frames is a measure of the variation in plume image axis orientation with respect to television lines in the image display. This parameter is relevant to the spatial analysis presented in Section 5.0.

Table 12 - Definitions of Data Intervals

Data Interval	GMT	TALO (s)	Plume-Camera Filter	Telemetry Frame Range	No. of Plume Images	No. of Tracker Images
1	7:30:41.82-7:30:47.66	81.52-87.36	PC-4	15645-15820	140	36
2	7:30:54.50-7:30:57.67	94.20-97.37	PC-3	16025-16120	61	16
3	7:31:03.25-7:31:07.18	102.95-106.88	PC-2	16287-16405	96	23
4	7:31:20.59-7:31:24.19	120.29-123.89	PC-1	16807-16915	88	21

Table 13 - Parameters Associated with Data Intervals

Data Interval	Plume Camera Filter	Bandpass (nm)	Plume to Tracker Ratio	UVPI-LCLV Range (km)	Image Angle Variation (deg)
1	PC-4	235-350	8:2	501	14.8
2	PC-3	195-295	8:2	489	9.9
3	PC-2	300-320	8:2	485	11.6
4	PC-1	220-320	8:2	493	7.4

The LCLV third-stage plume was first observed in the plume camera around frame 15364. Because of gain changes and ensuing transients in the plume camera, data analysis was limited to intervals 1 through 4 of Table 12. Approximately 5.8 s of filter 4 data, 3.2 s of filter 3 data, 3.9 s of filter 2 data, and 3.6 s of filter 1 data were collected during this time. Analysis of tracker-camera data is restricted to these same intervals.

#### 4.1.2 Calibration Parameters Associated with Intervals

Appendix B provides basic camera parameters pertinent to the radiometric calibration of the data for all frames during which the LCLV third stage was observed. Parameters provided include time, telemetry frame number, gain level for both cameras, and exposure time for both cameras. Changes in gain levels are indicated as are other comments. The plume camera has a constant 1/30th of a second exposure time for each frame. The tracker camera has an electronic gate that can vary the exposure time to a maximum of 1/30th of a second. Figure 15 shows the camera gain levels for both tracker and plume cameras. Figure 16 shows exposure time for both cameras as a function of telemetry frame number. In these figures, the data intervals are depicted as horizontal, bold, solid lines.

#### 4.2 Intensity History Overview

As a quick overview, Figs. 17 and 18 show plume-camera long-term trends in the central region and total spectral radiant intensity, respectively. The values plotted were derived assuming the reference spectral shape. Figure 19 shows similar results for the tracker-camera total spectral radiant intensity in a 19 by 19 pixel region containing the plume camera field of view. Notice that the tracker-camera mean changes from interval to interval. Consequently, part of the difference among measurements taken with the four filters of the plume camera is attributable to long-term temporal variations rather than to spectral differences.

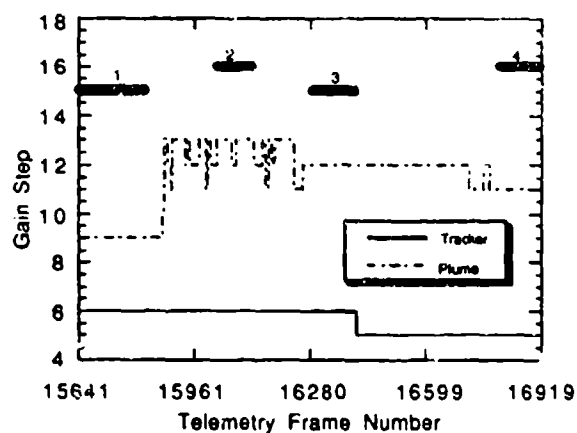


Fig. 15 - Tracker and plume camera gain

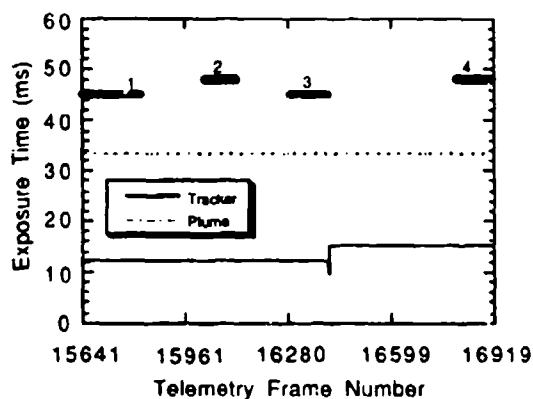


Fig. 16 - Tracker and plume camera exposure times

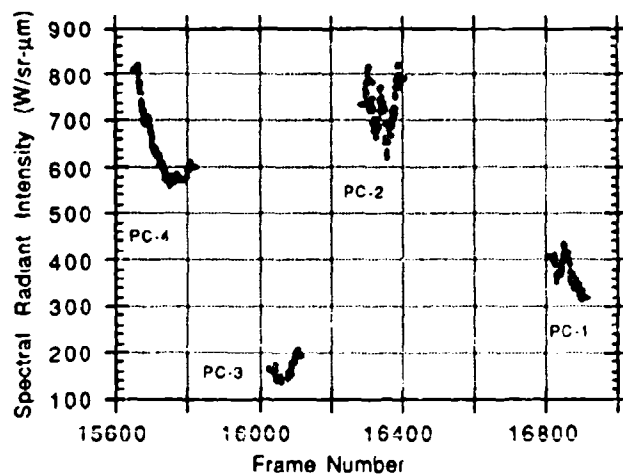


Fig. 17 - Spectral radiant intensity, plume camera, central region

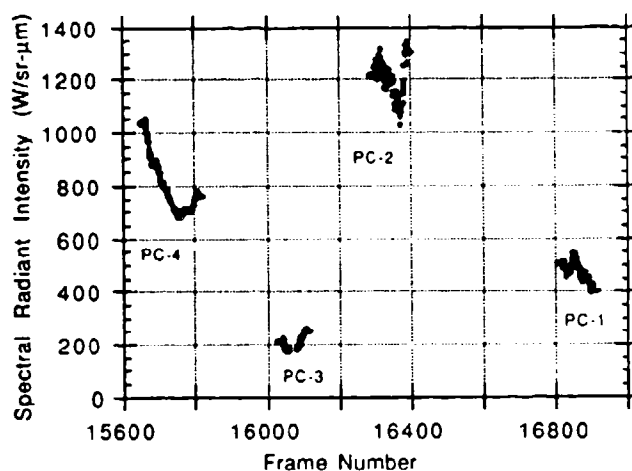


Fig. 18 - Spectral radiant intensity, plume camera, total

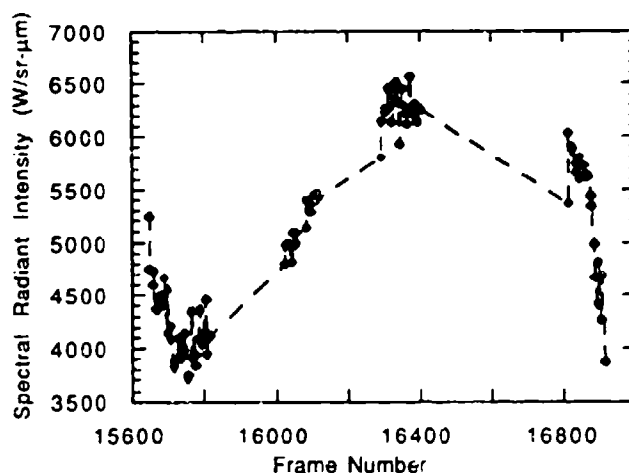


Fig. 19 - Spectral radiant intensity, tracker camera

For these figures, all curves specify spectral radiant intensity at the reference centroid wavelength for each interval.

#### 4.3 Single Images

This subsection presents raw plume image data. Given the characteristics of the UVPI cameras, e.g., exposure time, optics aperture, and the rocket plume radiant intensity, the number of photoevents that are registered within the focal plane array of a camera can be individually counted as isolated events. In this respect, UVPI can be used as a photon-counting instrument.

Figure 20 shows single images, in zoom image transmission rate, of the LCLV third-stage burn for the different filters. The image in the upper left corner is frame 15647, PC-4; the upper right corner is frame 16027, PC-3; the lower left corner is frame 16287, PC-2; and the lower right corner is frame 16808, PC-1. Pixel radiance is encoded as image brightness, where dark and bright are, respectively, relatively smaller and larger radiance. The images demonstrate that the shapes of the plume central region and outer region are not necessarily clearly delineated in a single frame.

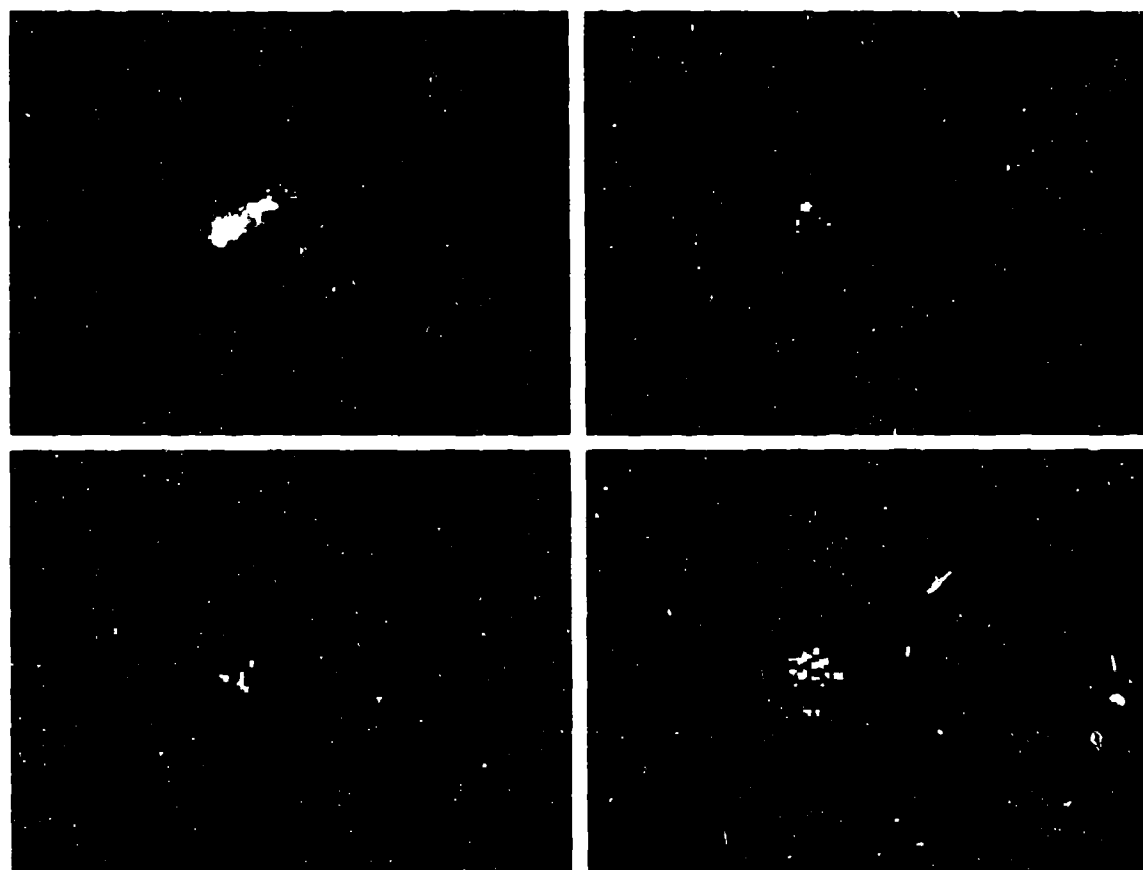


Fig. 20 - Single unprocessed plume camera images of the LCV third-stage plume

Every bright spot on the image corresponds to one or more photoevents that pile up at that particular pixel during the exposure time of the camera. Figure 21 illustrates the number of photoevents/s measured at each pixel location in the center 32 by 32 pixels of the lower left corner image shown in Fig. 20. The  $z$  axis corresponds to the number of photoevents/s, the  $x$  and  $y$  axes correspond to row and column indices. The actual procedure used to compute the number of photoevents from the measured digital number in the UVPI telemetry stream was discussed in Section 3 and in Ref. 1.

#### 4.4 Composite Plume Camera Images and Contour Plots

In this subsection composite plume camera images and their corresponding contour plots are presented showing the spatial distribution of the time-averaged plume radiance. The composite images are made up from calibrated versions of images formed while observing the LCV third stage during the four data intervals listed in Table 12 of Section 4. As explained in Section 3, the reference emission spectrum is assumed to convert UVPI measurements into units of radiance, i.e.,  $W/sr\text{-cm}^2$ . Within each interval the plume-to-tracker image ratio is 8:2, and the exposure time for each individual plume camera image is 1/30th of a second. Many individual images are superposed to form each composite image.

The limiting resolution of the UVPI cameras is described by the point spread function. Observation of a ground-based beacon, a source less than 5 m across, shows that the full-width-half-



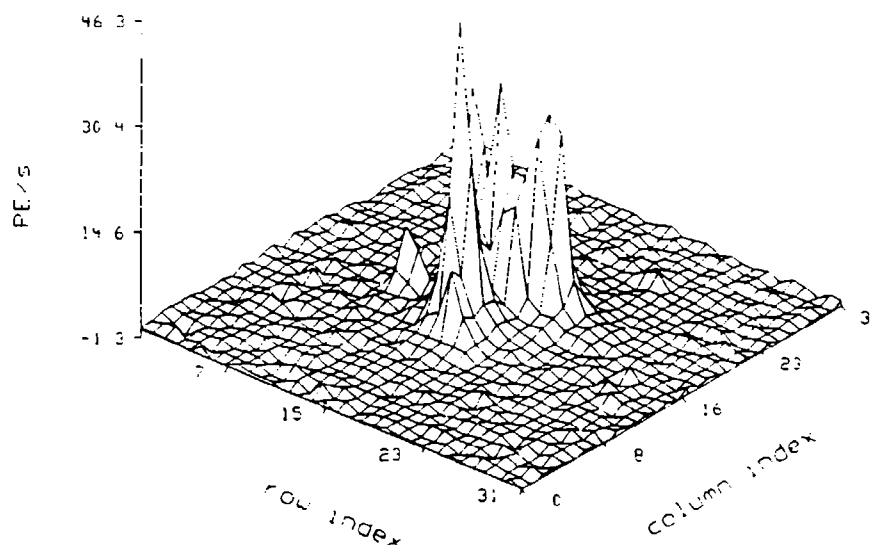


Fig. 21 - Single image of the LCLV third-stage plume

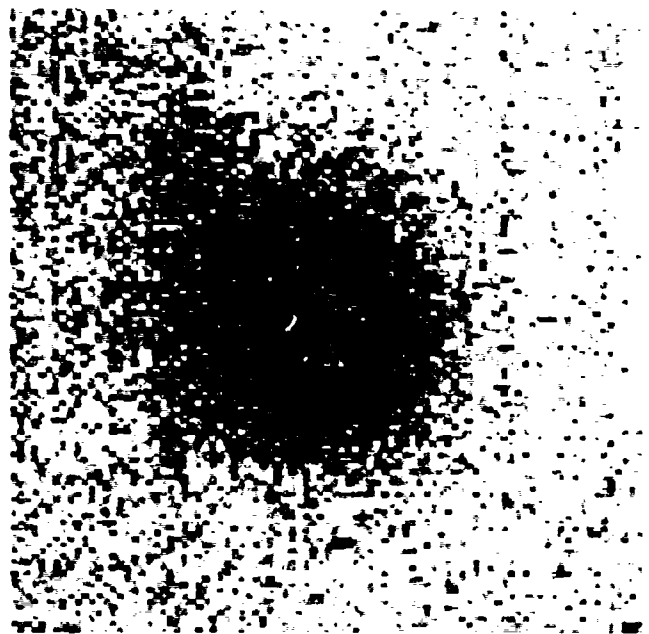
maximum of the point source response in the plume camera is about 9 pixels, or about 90  $\mu\text{rad}$ , which is equivalent to 40 m at a 450-km range. Figure 22 shows a plume-camera image of the beacon on the same scale as the plume images that follow. This is representative of the plume-camera's point spread function. Figure 23 shows the contour plot for the ground beacon, a point source, on the same scale as Figs. 25, 27, 29, and 31 discussed below. This figure indicates the resolution of the plume-camera contour plots due to the point spread function.

Figures 24, 26, 28, and 30 show the calibrated composite images for the four data intervals. In these images the radiant intensity has been mapped to a false-color scale, with black representing the highest intensity, light blue the middle intensity, and white the lowest intensity. A horizontal color bar depicting the mapping of radiant intensity into colors is shown on the lower left corner of each image. A histogram of the image intensity values is shown above the color bar in the form of dark dots.

Figures 25, 27, 29, and 31 show the contour plots for the four data intervals, starting with filter 4 and ending with filter 1. Table 14 contains the value of the maximum apparent pixel radiance measured for the brightest pixel for the plume camera as a function of data interval. The black, blue, and red contours represent, respectively, plume radiance contours at 95%, 50%, and 9.5% of the maximum radiance in the image. The radiance units are  $\text{W/steradian per square centimeter}$ , and the horizontal and vertical axes are scaled in meters. With each picture or plot a companion summary table provides relevant information for the quantitative interpretation of the image or plot. The parameters presented in these tables are described in Table 15.

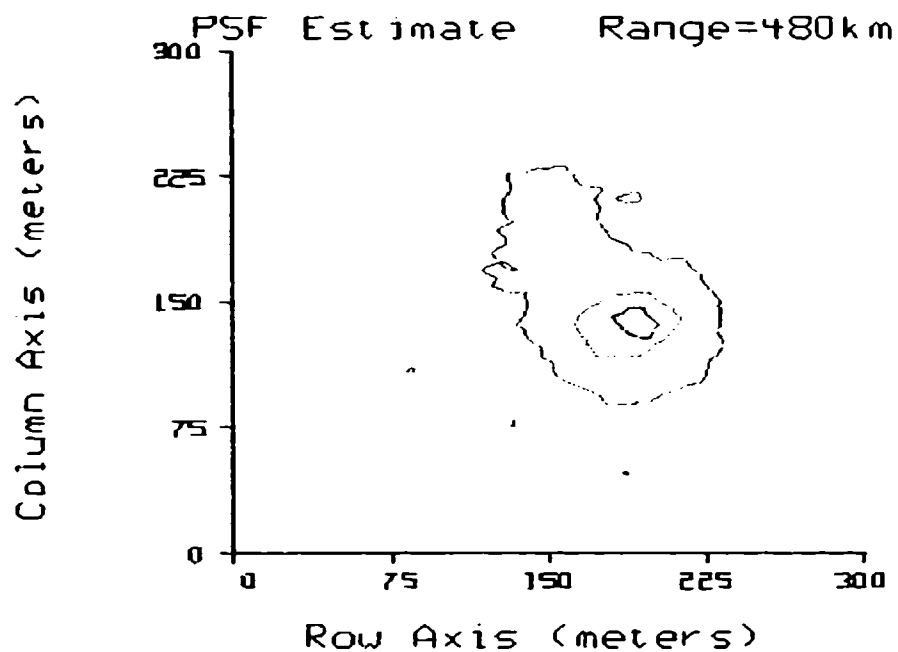
Table 14 - Plume Camera Apparent Peak Radiometric Values

Interval	Filter	Apparent Peak Radiance ( $\mu\text{W/sr-cm}^2$ )	Apparent Peak Spectral Radiance ( $\mu\text{W/sr-cm}^2\text{-}\mu\text{m}$ )	Centroid Wavelength (nm)
1	PC-4	3.65	$3.46 \times 10^1$	305
2	PC-3	1.07	$1.02 \times 10^1$	265
3	PC-2	1.06	$5.19 \times 10^1$	310
4	PC-1	2.17	$1.45 \times 10^1$	280



Observing sensor:	UVPI
Target observed:	UVPI ground-based beacon
Orbit number:	1173
Range of frames used:	12778-12778
Camera:	Plume
Displayed image size (pixels):	112 (vertical) x 91 (horizontal)
Average range (km):	450

Fig. 22 - Plume camera image of ground-based beacon illustrating the point spread function



$I = 0.095 \times \text{max}$     $I = 0.50 \times \text{max}$     $I = 0.95 \times \text{max}$

Observing sensor:	UVPI
Target observed:	UVPI ground-based beacon
Orbit:	1173
Range of frames used:	12778-12778
Camera:	Plume
Average range (km):	450

Fig. 23 - Plume camera contour plot for ground-based beacon

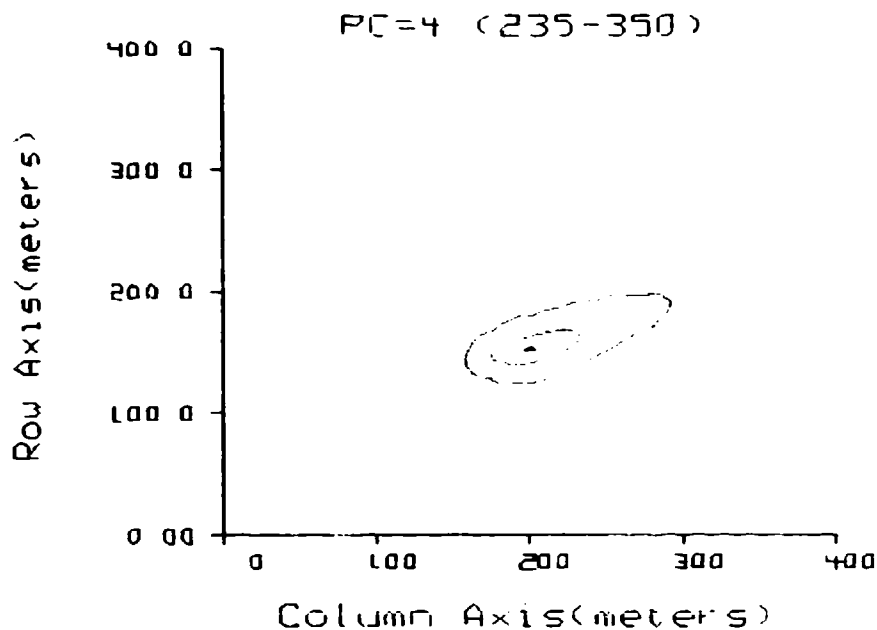


XX

Observing sensor:	UVPI (6 Feb. 1991)
Target observed:	LCLV, Stage 3
Range of frames used:	15645-15820
Number of superposed images:	140
Camera:	Plume
Spectral band (nm):	235-350 (PC-4)
Displayed image size (pixels):	112 (vertical) x 91 (horizontal)
Average range (km):	501
Pixel footprint (m) @ range:	5.01 (vertical) x 6.42 (horizontal)
Aspect angle (deg):	27.2
*Total photoevents/s:	$1.46 \times 10^4$
*Total radiant intensity (W/sr):	$8.51 \times 10^1$
*Total spectral radiant intensity @ 305 nm (W/sr- $\mu\text{m}$ ):	$8.06 \times 10^2$
*Error (%):	13.5

\*For full image.

Fig. 24 - Composite plume camera image for interval 1



max=3.65  $\mu\text{W}/\text{sr}\cdot\text{cm}^2$

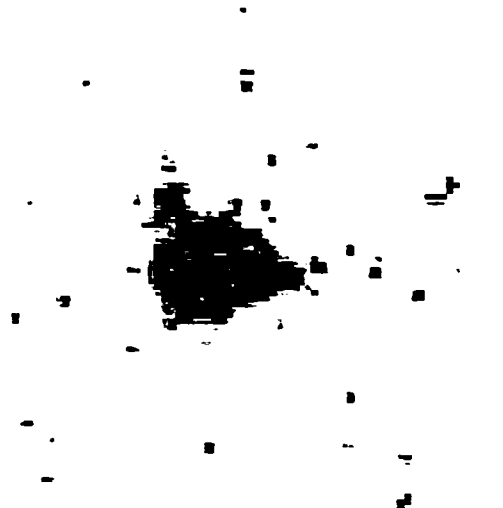
I = 0.095\*max I = 0.50\*max I = 0.95\*max

NRL/ACT 8/21/92

Observing sensor:	UVPI (6 Feb. 1991)
Target observed:	LCLV, Stage 3
Range of frames used:	15645-15820
Number of superposed images:	140
Camera:	Plume
Spectral band (nm):	235-350 (PC-4)
Displayed image size (pixels):	79.8 (vertical) x 62.3 (horizontal)
Average range (km):	501
Pixel footprint (m) @ range:	5.01 (vertical) x 6.42 (horizontal)
Aspect angle (deg):	27.2
*Photoevents/s:	$2.02 \times 10^2$
*Apparent peak radiance ( $\mu\text{W}/\text{sr}\cdot\text{cm}^2$ ):	3.65
*Apparent peak spectral radiance @ 305 nm ( $\mu\text{W}/\text{sr}\cdot\text{cm}^2\cdot\mu\text{m}$ ):	$3.46 \times 10^1$

\*For brightest pixel.

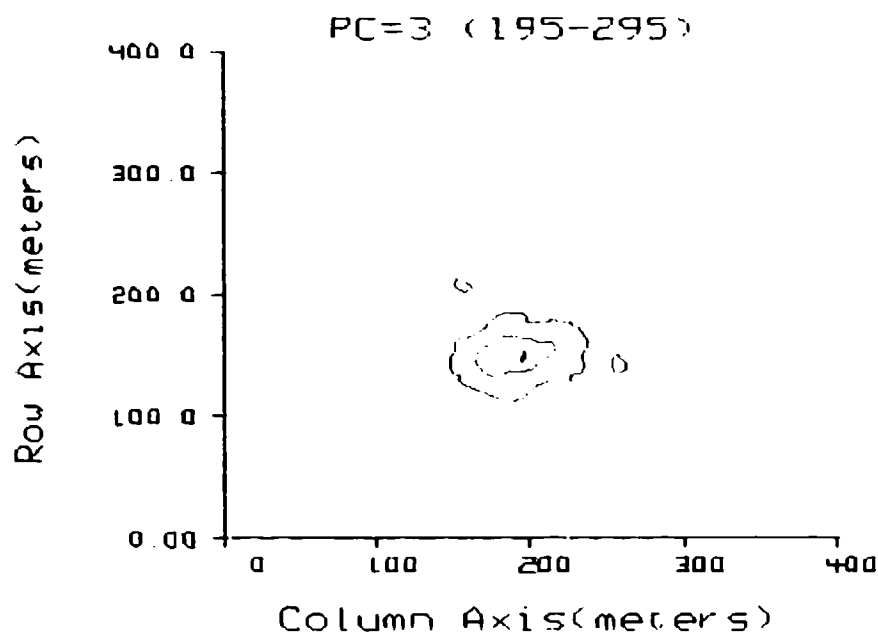
Fig. 25 - Plume camera contour plot for interval 1



Observing sensor:	UV 1 (6 Feb. 1991)
Target observed:	LCLV, Stage 3
Range of frames used:	16025-16120
Number of superposed images:	61
Camera:	Plume
Spectral band (nm):	195-295 (PC-3)
Displayed image size (pixels):	112 (vertical) x 91 (horizontal)
Average range (km):	489
Pixel footprint (m) @ range:	4.89 (vertical) x 6.26 (horizontal)
Aspect angle (deg):	24.4
*Total photoevents/s:	$5.81 \times 10^2$
*Total radiant intensity (W/sr):	$2.31 \times 10^1$
*Total spectral radiant intensity @ 265 nm (W/sr- $\mu\text{m}$ ):	$2.21 \times 10^2$
*Error (%):	10.8

\*For full image.

Fig. 26 - Composite plume camera image for interval 2



max=1.06uW/sr-cm<sup>2</sup>

| =0.095\*max | =0.50\*max | =0.95\*max

NRL/ACT 8/21/92

Observing sensor:	UVPI (6 Feb. 1991)
Target observed:	LCLV, Stage 3
Range of frames used:	16025-16120
Number of superposed images:	61
Camera:	Plume
Spectral band (nm):	195-295 (PC-3)
Displayed image size (pixels):	81.8 (vertical) x 63.9 (horizontal)
Average range (km):	489
Pixel footprint (m) @ range:	4.89 (vertical) x 6.26 (horizontal)
Aspect angle (deg):	24.4
*Photoevents/s:	8.19
*Apparent peak radiance (μW/sr-cm <sup>2</sup> ):	1.07
*Apparent peak spectral radiance @ 265 nm (μW/sr-cm <sup>2</sup> -μm):	1.02 x 10 <sup>1</sup>

\*For brightest pixel.

Fig 27 - Plume camera contour plot for interval 2

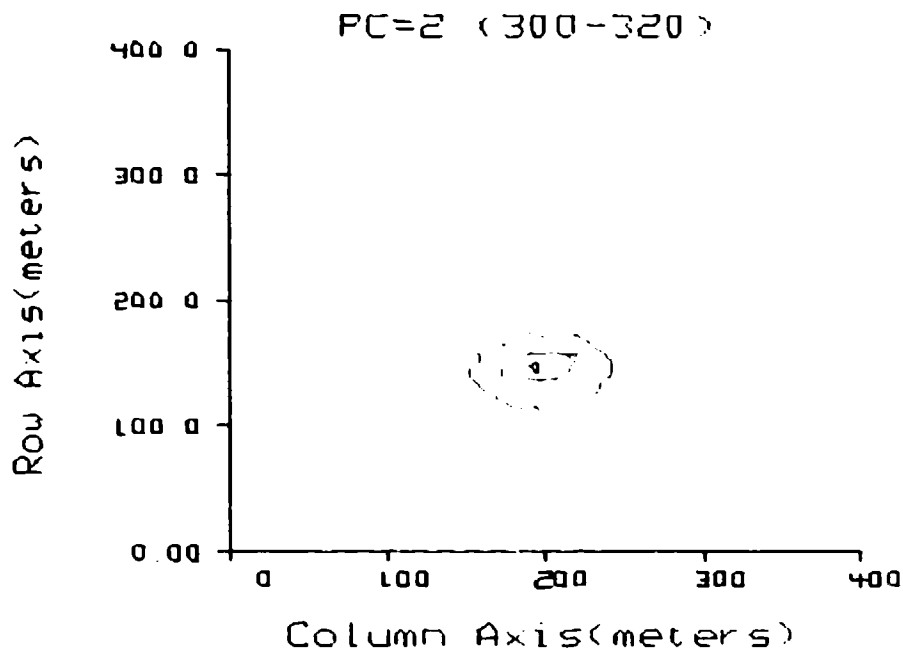


Observing sensor:	UVPI (6 Feb. 1991)
Target observed:	LCLV, Stage 3
Range of frames used:	16287-16405
Number of superposed images:	96
Camera:	Plume
Spectral band (nm):	300-320 (PC-2)
Displayed image size (pixels):	112 (vertical) x 91 (horizontal)
Average range (km):	485
Pixel footprint (m) @ range:	4.85 (vertical) x 6.21 (horizontal)
Aspect angle (deg):	25.6
*Total photoevents/s:	$1.32 \times 10^3$
*Total radiant intensity (W/sr):	$2.48 \times 10^1$
*Total spectral radiant intensity @ 310 nm (W/sr- $\mu\text{m}$ ):	$1.22 \times 10^3$
*Error (%):	16.0

\*For full image.

Fig. 28 - Composite plume camera image for interval 3





max=1.06uW/sr-cm<sup>2</sup>

| =0.895\*max | =0.50\*max | =0.95\*max

NRL/ACT 8/21/92

Observing sensor:	UVPI (6 Feb. 1991)
Target observed:	LCLV, Stage 3
Range of frames used:	16287-16405
Number of superposed images:	96
Camera:	Plume
Spectral band (nm):	300-320 (PC-2)
Displayed image size (pixels):	82.4 (vertical) x 64.4 (horizontal)
Average range (km):	485
Pixel footprint (m) @ range:	4.85 (vertical) x 6.21 (horizontal)
Aspect angle (deg):	25.6
*Photoevents/s:	$1.70 \times 10^1$
*Apparent peak radiance ( $\mu\text{W}/\text{sr}\cdot\text{cm}^2$ ):	1.06
*Apparent peak spectral radiance @ 310 nm ( $\mu\text{W}/\text{sr}\cdot\text{cm}^2\cdot\mu\text{m}$ ):	$5.19 \times 10^1$

\*For brightest pixel.

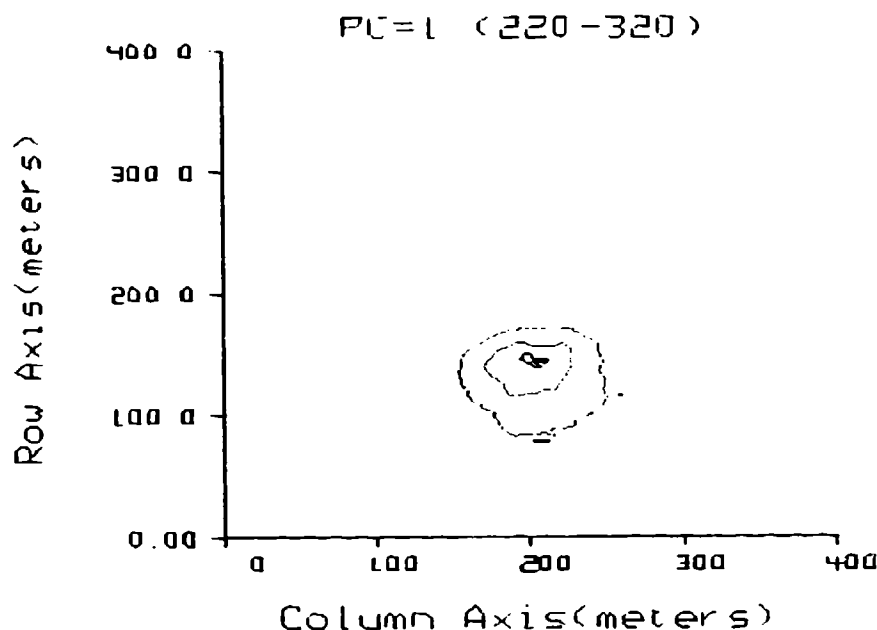
Fig. 29 - Plume camera contour plot for interval 3



Observing sensor:	UVPI (6 Feb. 1991)
Target observed:	LCLV, Stage 3
Range of frames used:	16807-16915
Number of superposed images:	88
Camera:	Plume
Spectral band (nm):	220-320 (PC-1)
Displayed image size (pixels):	112 (vertical) x 91 (horizontal)
Average range (km):	493
Pixel footprint (m) @ range:	4.93 (vertical) x 6.31 (horizontal)
Aspect angle (deg):	34.1
*Total photoevents/s:	$2.27 \times 10^3$
*Total radiant intensity (W/sr):	$7.00 \times 10^1$
*Total spectral radiant intensity @ 280 nm (W/sr- $\mu\text{m}$ ):	$4.67 \times 10^2$
*Error (%):	10.8

\*For full image.

Fig. 30 - Composite plume camera image for interval 4



max=2.17  $\mu\text{W}/\text{sr}\cdot\text{cm}^2$

I = 0.095\*max I = 0.50\*max I = 0.95\*max

NRL/ACT 8/21/92

Observing sensor:	UVPI (6 Feb. 1991)
Target observed:	LCLV, Stage 3
Range of frames used:	16807-16915
Number of superposed images:	88
Camera:	Plume
Spectral band (nm):	220-320 (PC-1)
Displayed image size (pixels):	81.2 (vertical) x 63.4 (horizontal)
Average range (km):	493
Pixel footprint (m) @ range:	4.93 (vertical) x 6.31 (horizontal)
Aspect angle (deg):	34.1
*Photoevents/s:	$2.19 \times 10^1$
*Apparent peak radiance ( $\mu\text{W}/\text{sr}\cdot\text{cm}^2$ ):	2.17
*Apparent peak spectral radiance @ 280 nm ( $\mu\text{W}/\text{sr}\cdot\text{cm}^2\cdot\mu\text{m}$ ):	$1.45 \times 10^1$

\*For brightest pixel.

Fig. 31 - Plume camera contour plot for interval 4

Table 15 - Description of Basic Parameters

Aspect Angle	Angle, in degrees, between the line of sight and the rocket body longitudinal vector.
Average Range	Average distance, in kilometers, between UVPI and the plume target.
Camera	Camera used, either tracker or plume.
Displayed Image Size	Size in pixels (picture elements) of the image being displayed.
Number of Superposed Images	Number of images averaged together to generate the composite image. Because of the tracker-to-plume image ratio, this number is not equal to the number of frames in the range.
Pixel Footprint	Projected pixel dimensions, in meters, at target range. This number does not account for any spreading introduced by the optics or jitter because it incorporates only the instantaneous field of view.
Range of Frames Used	Range of frames containing the set of tracker or plume camera images superposed.
Spectral Band	Spectral band, in nanometers, covered by all images within the set. This band includes more than 99% of the net quantum efficiency response curve.
Target Observed	LCLV Stage 3
Total Photoevents/s	Sum of all photoevent-per-second pixel values over the specified region of the focal plane.
Total Radiant Intensity (W/sr)	Radiant intensity associated with the total photoevents per second.
Total Spectral Radiant Intensity (W/sr- $\mu\text{m}$ )	Spectral radiant intensity at the specified centroid wavelength associated with the total photoevents/s.
Apparent Peak Radiance ( $\mu\text{W/sr-cm}^2$ )	Apparent radiance measured at the brightest pixel in an image. Because of the size and structure of UVPI's point spread function, the value given is likely not to be a good measure of the true peak radiance at the source. The value is useful for rough comparisons and order of magnitude estimates.
Apparent Peak Spectral Radiance ( $\mu\text{W/sr-cm}^2\text{-}\mu\text{m}$ )	Apparent spectral radiance at the specified centroid wavelength measured at the brightest pixel in an image. Because of the size and structure of UVPI's point spread function, the value given is likely not to be a good measure of the true peak spectral radiance at the source. The value is useful for rough comparisons and order of magnitude estimates.
Error (%)	Total error associated with the above radiometric values. This error includes gain conversion factor error and error attributable to photon shot noise and detector noise. Error estimate is based on the total number of images superposed. See Section 4.6 for in-depth discussion.

Because of the UVPI's dynamic range of 256 levels in the analog-to-digital converter, it is difficult to get well-defined plume contours at levels below 9.5% of the maximum radiance unless a large number of images are superposed.

Table 14 also shows apparent peak spectral radiance reported at the specified centroid wavelength. Because of the size and structure of UVPI's point spread function, the values given are primarily useful for rough comparisons and order-of-magnitude estimates. Estimates of true source peak radiance requires further analysis. A comparison of UVPI apparent peak radiance measurements with CHARM 1.4 code predictions is presented in Section 5.3.

Note that the number of images superposed in each data interval can be significantly different. For example, only 61 images were used for interval 2 and 140 were used for interval 1. For each interval, as many images as possible were superposed.

Because of the relatively long observation time, the apparent rocket velocity vector changes from interval to interval. The velocity is directed out of the page toward the viewer at an angle that is the complement of the aspect angle shown in Fig. 9. Over the period of observation, the direction of the rocket velocity vector projected on the image plane changes significantly. Table 16 summarizes the direction of the velocity vector projected on the image plane.

Table 16 - Apparent Velocity Vector Direction for Each Interval

Interval	Filter	Direction of Motion Relative to Tracker Camera X Axis (deg)
1	PC-4	-56.7
2	PC-3	-89.1
3	PC-2	-117.1
4	PC-1	-159.9

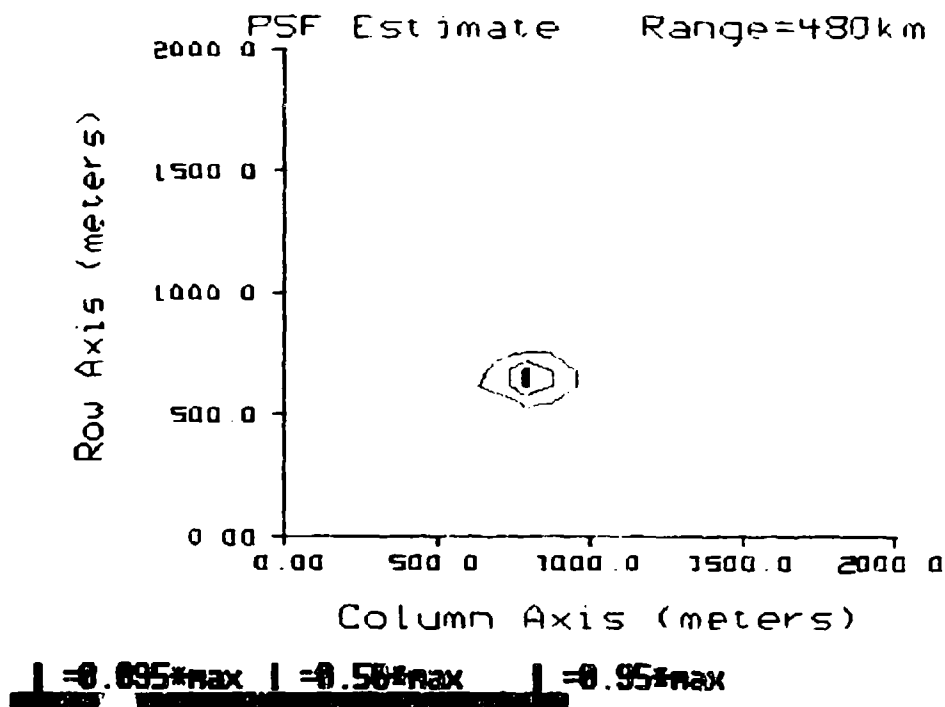
#### 4.5 Calibrated Tracker-Camera Images

While the plume camera gathered rocket plume images, the tracker camera gathered images at a lower rate because of the plume-to-tracker image ratio. The tracker camera's exposure time varied over the data intervals, as shown in Table 17.

Table 17 - Tracker Camera Exposure Time

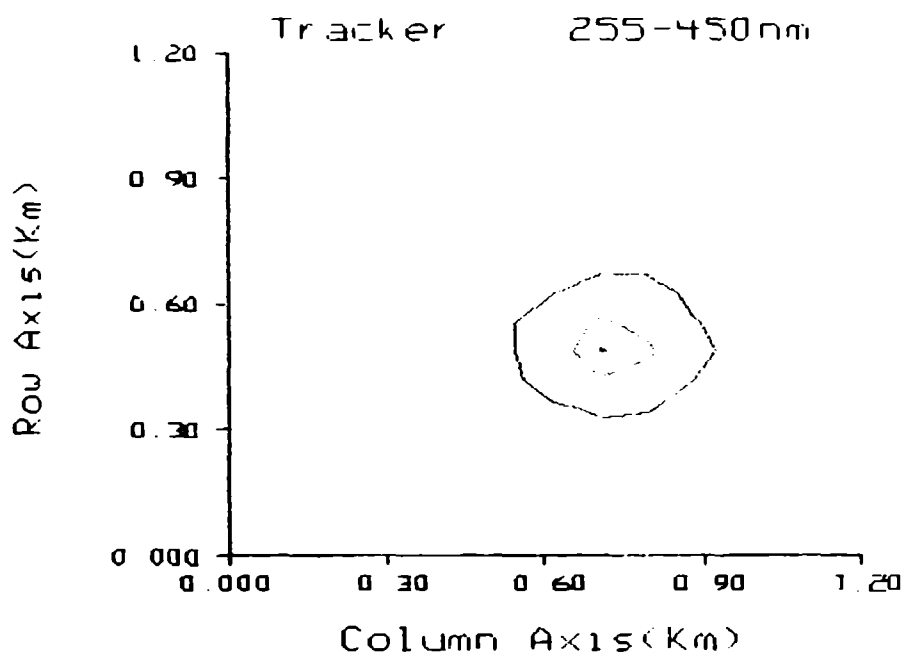
Data Interval	Tracker Camera Exposure Time (ms)
1	12.2
2	12.2
3	12.2
4	15.4

The limiting resolution of the UVPI cameras is described by the point spread function. Observation of the ground-based beacon, a source less than 5 m across, shows that the full-width-half-maximum of the point source response in the tracker camera is about 1.5 pixels, or about 230  $\mu$ rad. This is equivalent to 104 m at 450-km range. Figure 32 is a tracker-camera contour plot of the ground-based beacon. This is representative of the tracker camera's point spread function and can be compared with the interval 3 tracker-camera contour plot shown in Fig. 33. Figure 34 shows a tracker-camera image of the ground-based beacon on the same scale as the LCLV tracker-camera images that follow. The corresponding composite tracker-camera images for each of the four data intervals are shown in Figs. 35 through 38.



Observing sensor:	UVPI
Target observed:	UVPI ground-based beacon
Orbit number:	1173
Range of frames used:	12772 - 12772
Camera:	Tracker
Displayed image size (pixels):	112 (vertical) x 91 (horizontal)
Average range (km):	450

Fig. 32 - Tracker-camera contour plot for ground-based beacon



max=1.65  $\mu\text{W}/\text{sr}\cdot\text{cm}^2$

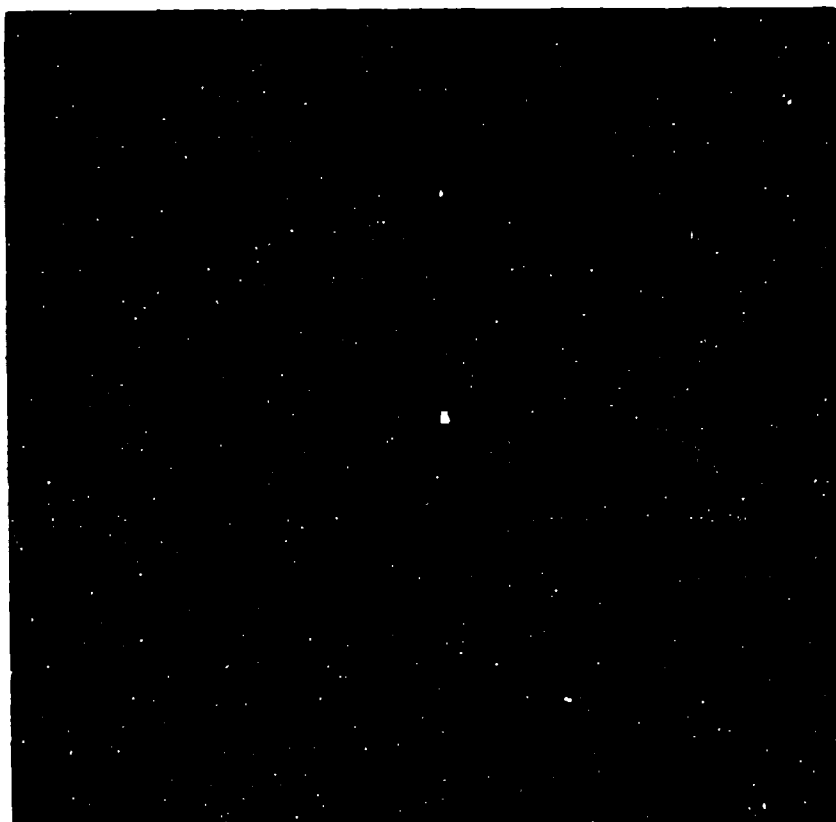
=0.095\*max | =0.50\*max | =0.95\*max

NRL/ACT 8/4/92

Observing sensor:	UVPI (6 Feb. 1991)
Target observed:	LCLV Stage 3
Range of frames used:	16287-16405
Number of superposed images:	23
Camera:	Tracker
Spectral band (nm):	255 - 450
Displayed image size (km):	2 (vertical) x 2 (horizontal)
Average range (km):	485
Pixel footprint (m) @ range:	69.9 (vertical) x 87.6 (horizontal)
Aspect angle (deg):	25.6
*Photoevents/s:	$9.94 \times 10^4$
*Apparent peak radiance ( $\mu\text{W}/\text{sr}\cdot\text{cm}^2$ ):	1.65
*Apparent peak spectral radiance @ 390 nm ( $\mu\text{W}/\text{sr}\cdot\text{cm}^2\cdot\mu\text{m}$ ):	$1.32 \times 10^1$

\*For brightest pixel.

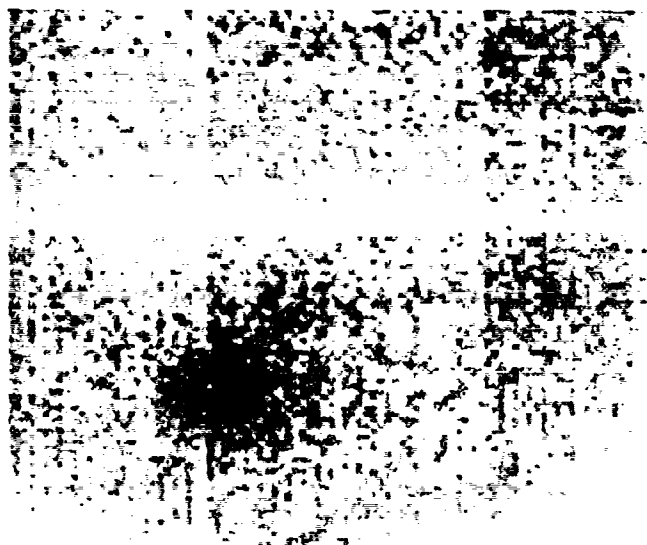
Fig. 33 - Tracker-camera contour plot for interval 3



<b>Observing sensor:</b>	UVPI
<b>Target observed:</b>	UVPI ground-based beacon
<b>Orbit number:</b>	1173
<b>Range of frames used:</b>	12772-12772
<b>Camera:</b>	Tracker
<b>Displayed image size (pixels):</b>	112 (vertical) x 91 (horizontal)
<b>Average range (km):</b>	450

Fig. 34 – Tracker-camera image of ground-based beacon illustrating the point spread function





Observing sensor:	UVPI (6 Feb. 1991)
Target observed:	LCLV, Stage 3
Range of frames used:	15645-15820
Number of superposed images:	36
Camera:	Tracker
Spectral band (nm):	255 - 450
Displayed image size (pixels):	112 (vertical) x 91 (horizontal)
Average range (km):	501
Pixel footprint (m) @ range:	72.1 (vertical) x 90.5 (horizontal)
Aspect angle (deg):	27.2
*Total photoevents/s:	$5.06 \times 10^5$
*Total radiant intensity (W/sr):	$5.49 \times 10^2$
*Total spectral radiant intensity @ 390 nm (W/sr- $\mu\text{m}$ ):	$4.38 \times 10^3$
*Error (%):	$\geq 15.6$

\*For central 19 x 19 pixels.

Fig. 35 - Composite tracker-camera image for interval 1

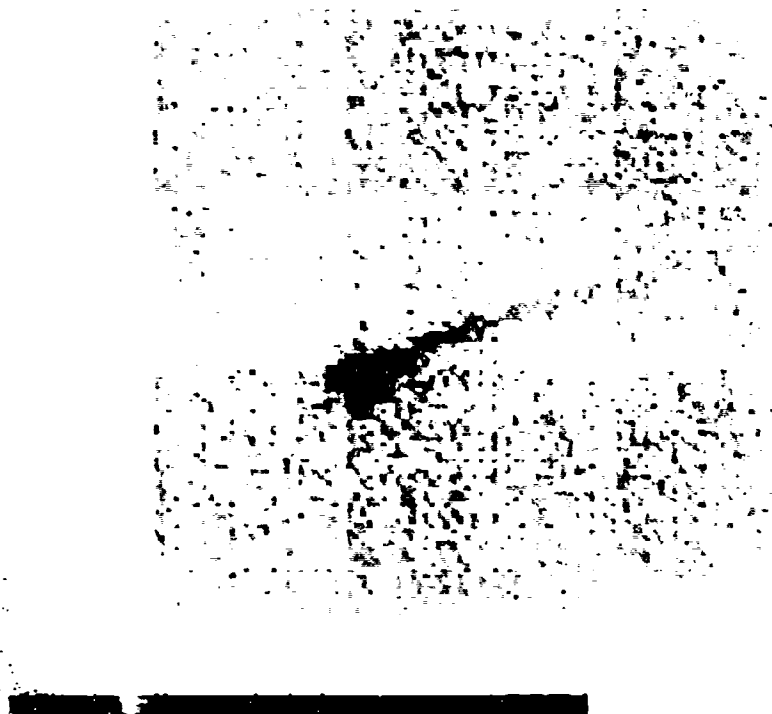


**Figure 37 - Composite tracker-camera image for interval 3**

Observing sensor:	UVPI (6 Feb. 1991)
Target observed:	LCLV, Stage 3
Range of frames used:	16287-16405
Number of superposed images:	23
Camera:	Tracker
Spectral band (nm):	255 - 450
Displayed image size (pixels):	112 (vertical) x 91 (horizontal)
Average range (km):	485
Pixel footprint (m) @ range:	69.9 (vertical) x 87.6 (horizontal)
Aspect angle (deg):	25.6
*Total photoevents/s:	$7.51 \times 10^5$
*Total radiant intensity (W/sr):	$7.63 \times 10^2$
*Total spectral radiant intensity @ 390 nm (W/sr- $\mu\text{m}$ ):	$6.09 \times 10^3$
*Error (%):	$\geq 15.6$

\*For central 19 x 19 pixels.

Fig. 37 - Composite tracker-camera image for interval 3



Observing sensor:	UVPI (6 Feb. 1991)
Target observed:	LCLV, Stage 3
Range of frames used:	16807-16915
Number of superposed images:	21
Camera:	Tracker
Spectral band (nm):	255 - 450
Displayed image size (pixels):	112 (vertical) x 91 (horizontal)
Average range (km):	493
Pixel footprint (m) @ range:	70.9 (vertical) x 89.0 (horizontal)
Aspect angle (deg):	34.1
*Total photoevents/s:	$6.34 \times 10^5$
*Total radiant intensity (W/sr):	$6.64 \times 10^2$
*Total spectral radiant intensity @ 390 nm (W/sr- $\mu\text{m}$ ):	$5.30 \times 10^3$
*Error (%):	$\geq 15.6$

\*For central 19 x 19 pixels.

Fig. 38 - Composite tracker-camera image for interval 4

With each picture or plot a companion summary table provides relevant information for the quantitative interpretation of the image or plot. The parameters presented in these tables are described in Table 15. Radiometric values reported in the table accompanying each figure are for the central 19 by 19 pixels of the tracker camera. This field of view approximately matches the total field of view of the plume camera. This field of view contains plume central region and a portion of the outer region. Therefore, it cannot reliably be converted to radiant intensity or spectral radiant intensity. However, to provide estimates of the radiant intensity and spectral radiant intensity, values based on reference spectral energy distribution assumptions are reported for the tracker camera observations. These results have been reduced by 16.3% to account for red leakage in the tracker-camera filter.

Note that the number of images superposed in each data interval can be significantly different. For example, only 16 images were used for interval 2, and 36 were used for interval 1. For each interval, as many images as possible were superposed.

#### 4.6 Error Analysis for Radiometric Observations

The complete estimate of the error in determining radiometric values from the digital numbers reported by the UVPI cameras observing a rocket plume is composed of two components: (a) measurement noise, summarized in 4.6.1, which includes photon shot noise and other intrinsic sensor noise sources, and (b) calibration error, summarized in 4.6.2, which is the error contained in the gain conversion factor. Section 4.6.3 summarizes the calculation of the total error based on the error components presented in 4.6.1 and 4.6.2. Reference 1 provides detailed discussions of error estimates.

##### 4.6.1 Due to Measurement Noise

Because of photon shot noise, the error in the calculated number of photoevents changes as a function of the plume radiant intensity, which could change as a function of time. This error analysis assumes that the radiant intensity statistics are not affected by a small shift in time. A window size of 15 consecutive images was selected for the statistical analysis of the plume-camera data, and a window of 15 consecutive images was selected for the tracker-camera analysis. A larger time window could be used with the risk of making the locally constant assumption invalid.

Given the number of photoevents as a function of image, the following quantities are defined:

- $M$  is number of images in data interval,
- $N$  is number of images used within the window,
- $\mu_i$  is local mean over  $N$  images around  $i$ th image,
- $\sigma_i$  is local standard deviation around  $i$ th image,
- $t_i$  is  $3.1\sigma_i + \mu_i$  detection threshold,
- $\epsilon_i$  is  $\sigma_i/\mu_i$  local error around the  $i$ th image,
- $G_g$  is gain conversion factor for gain step  $g$ , in units of sensor output per photoevent,
- $\epsilon_{1/G}$  is error in  $1/G_g$ ,
- $\epsilon_N$  is average local error in the measured number,

$$\epsilon_N = \frac{1}{M} \sum_i \left( \frac{\sigma_i}{\mu_i} \right), \quad (16)$$

$\epsilon_u$  is upper bound error in the measured number for the case of  $M$  averaged images,

$$\epsilon_u = \frac{\max(\epsilon_i)}{\sqrt{M}}, \text{ over all } i. \quad (17)$$

To prevent extreme values from affecting the local statistics, the maximum and minimum values within the  $N$  window samples were rejected. That is, only  $N-2$  images were used for the local mean and local standard deviation computation. Under the assumption that the mean radiant intensity is high enough for the radiant intensity fluctuations to be modeled by a gaussian distribution, the probability of exceeding the above defined threshold  $t_i$  is no more than 0.001.

Table 18 lists  $M$ , the number of images averaged in each data interval, and  $\epsilon_N$ , the error due to measurement in the values averaged over the window that consists of  $N$  images. The three columns of  $\epsilon_N$  values correspond to plume-camera central region measurements, plume-camera central region plus outer region, and tracker-camera 19 by 19 pixel field of view. The central region and outer region as used in this report are defined in Section 5.1. Because of the small number of tracker camera frames available for analysis in each interval, an accurate measurement of frame-to-frame variation was not possible for the tracker camera.

Table 18 - Percent Error Per Image Due to Measurement Noise  $\epsilon_N$

Interval	Images (M)	Plume-Camera Central Region	Plume-Camera Central Region + Outer Region	Tracker Camera 19 x 19
1	140	6.51	7.11	-
2	61	28.6	24.8	-
3	96	20.3	15.9	-
4	88	18.6	17.5	-

#### 4.6.2 In Gain Conversion Factor

The gain conversion factor  $G_g$ , derived from on-orbit calibration [1], is based on calibration star measurements. Based on measurements of several calibration stars over the full set of UVPI camera gains, an estimate of error associated with  $G_g$  can be obtained for each camera configuration by calculating the deviations of individual calibration star measurements about a mean calibration curve.

Table 19 tabulates the error associated with the gain conversion factor for the plume and tracker cameras. The average deviation is a good error estimate; the maximum deviation gives a worst-case estimate.

Table 19 - Error in  $1/G_g$  for Tracker and Plume Cameras

Camera/Filter	Average Deviation from Mean Calibration Curve(%)	Maximum Deviation from Mean Calibration Curve(%)
Tracker	15.6	17.3
Plume, PC-1	10.5	33.3
Plume, PC-2	15.9	25.2
Plume, PC-3	9.9	24.7
Plume, PC-4	13.5	26.0

### 4.6.3 Calculation of Total Error

The estimated total calibration error depends on the number of images averaged together,  $M$ . In this report we define the total error as the ratio of the standard deviations of the number of photoevents to the mean value of the number of photoevents. Assuming that the digital number reported by UVPI for a calibration star and the gain conversion factor  $G_g$  are uncorrelated, or weakly correlated, then the total error per image  $\epsilon_F$  can be obtained from [15]:

$$\epsilon_F = \sqrt{\epsilon_N^2 \cdot \epsilon_{1/G}^2 + \epsilon_N^2 + \epsilon_{1/G}^2} \quad (18)$$

where  $\epsilon_N$  is the average local error in the number of measured photoevents presented in Table 18, and  $\epsilon_{1/G}$  is the error in the gain conversion factor tabulated in Table 19.

For the case of  $M$ , an upper bound estimate of the total error is given by:

$$\epsilon_T = \sqrt{\epsilon_u^2 \cdot \epsilon_{1/G}^2 + \epsilon_u^2 + \epsilon_{1/G}^2} \quad (19)$$

Notice that  $\epsilon_T$  can never be smaller than  $\epsilon_{1/G}$  no matter how many images are averaged.

Table 20 summarizes the overall error analysis results for the plume central region radiant intensities for each of the data intervals. The first column identifies the data interval. The second column contains the number of images within the data interval. The column under the  $K$  heading contains the ratio of the average standard deviation of photoevents to the square root of the average number of photoevents, i.e.,

$$K = \frac{1}{N} \sum_i \left( \frac{\sigma_i}{\sqrt{\mu_i}} \right) \quad (20)$$

Under the assumption that the signal is not changing rapidly in time,  $K$  relates the measured noise to the theoretical performance of a background-limited system, where the dominant source of noise is shot noise. A ratio of  $K \approx 1$  implies pure background-limited performance. Hence, the values obtained indicate that although UVPI is close to background-limited performance, other sources of sensor noise are present.

The fourth and fifth columns show, respectively, the total percent error on an image-by-image basis and the total percent error resulting after averaging all  $M$  images available within the appropriate data interval.

Similar to Table 20, Table 21 shows, the radiant intensity errors for the total plume-camera field of view.

Because of the small number of tracker-camera frames available for analysis, an accurate measurement of these values for the tracker camera was not possible. Consequently, the gain conversion factor error  $\epsilon_{1/G}$  is given as a lower bound for  $\epsilon_T$  in Table 22.

Table 23 lists  $\epsilon_T$  for each of the four data intervals for the plume camera observing the central region only, the plume camera observing the central region and the outer region, and the 19 by 19 pixel field in the tracker camera that corresponds to the full plume-camera field of view.

Table 20 – Plume Central Region Radiometric  
Percent Errors for Plume Camera

Interval	$M$	$K$	$\epsilon_F$	$\epsilon_T$
1	140	1.28	15.0	13.5
2	61	1.10	30.4	10.8
3	96	1.05	26.0	15.9
4	88	1.44	21.4	10.9

Table 21 – Central Region Plus Outer Region Radiometric  
Percent Errors for Plume Camera

Interval	$M$	$K$	$\epsilon_F$	$\epsilon_T$
1	140	1.57	15.3	13.5
2	61	1.07	26.9	10.8
3	96	1.05	22.6	16.0
4	88	1.53	20.5	10.8

Table 22 – Radiometric Percent Errors: Tracker  
Camera Over 19 x 19 Pixel Window

Interval	$M$	$K$	$\epsilon_F$	$\epsilon_T$
1	36	–	–	$\geq 15.6$
2	16	–	–	$\geq 15.6$
3	23	–	–	$\geq 15.6$
4	21	–	–	$\geq 15.6$

Table 23 – Total Radiometric Percent Errors  $\epsilon_T$

Interval	Plume-Camera Central region	Plume-Camera Central region + Outer region	Tracker Camera 19 x 19
1	13.5	13.5	$\geq 15.6$
2	10.8	10.8	$\geq 15.6$
3	15.9	16.0	$\geq 15.6$
4	10.9	10.8	$\geq 15.6$



#### 4.7 Noise Equivalent Radiance

Following the noise equivalent radiance (NER) definition given in the *Infrared Handbook* [16], the UVPI NER is defined as the source radiance level that will result in a signal-to-noise ratio (SNR) of 1 at the output of a single pixel. The NER can be interpreted as the sensitivity limit for an imaging system. For UVPI, a single NER number does not fully characterize the sensitivity of the system since this is a function of integration time, spectral filter, camera gain level, number of images superposed, and the assumed source spectrum.

The following discussion is based on empirical estimates of the signal and noise within the UVPI cameras as opposed to a theoretical discussion. Reference 17 provides a theoretical expression for the signal power to noise power ratio applicable to the microchannel plate image intensifier of the UVPI. A single pixel in the plume or tracker camera can be treated as a photoevent counting device. The SNR definition from which the empirical UVPI NER is derived is:

$$(SNR)^2 = M^2 \cdot S^2 / (M \cdot N^2 + M \cdot N_S^2), \quad (21)$$

where:

- $M$  is the number of images superposed; this affects the effective integration time.
- $S$  is the mean number of signal related photoevents collected in a pixel during the integration time.
- $N$  is the signal-independent noise standard deviation for a single pixel in a single image expressed in photoevents/pixel-image. This noise source is constant. When expressed in photoevents/pixel-image, its level depends on the camera gain setting used.
- $N_S$  is the signal-dependent noise standard deviation, in a pixel during the integration time, expressed in photoevents/pixel-image. Based on extensive measurements made on UVPI data, the signal-dependent noise can be expressed in terms of the mean number of signal related photoevents by using the following equation:

$$N_S = 2S^{1/2}. \quad (22)$$

Note that this is two times higher than the photon shot noise prediction.

From the SNR expression above, the mean number of signal-related photoevents/pixel-image in a pixel that will result in a SNR of 1 is

$$S' = 2 \left[ 1 + \left( 1 + M \cdot N^2/4 \right)^{1/2} \right] / M. \quad (23)$$

Notice that for the case of only one superposed image,  $M = 1$ , and a negligible level of sensor noise  $N$ , the resulting sensitivity limit is 4 photoevents/pixel-image. The NER is related to  $S'$  by a multiplicative constant  $K$ , i.e.,

$$NER = K \cdot S' = 2K \left[ 1 + \left( 1 + M \cdot N^2/4 \right)^{1/2} \right] / M, \quad (24)$$

where  $K$  is the radiometric calibration constant that converts from photoevents/pixel-image to  $\mu\text{W}/\text{sr}\cdot\text{cm}^2$ .  $K$  is a function of the spectral filter used, the single image exposure time, and the assumed source spectrum.

The radiometric sensitivity could also be improved by performing spatial averaging at the expense of a lower spatial resolution.

Table 24 summarizes the estimated NERs, or sensitivity levels, for the four data intervals of the plume camera, under the assumption of the reference spectrum. Since, for the plume camera, the signal-independent noise is negligible compared to the signal-dependent noise, image superposition provides an increase in sensitivity that is linear with the number of superposed images.

Table 24 – Plume Camera NER per Pixel for Data Intervals

Data Interval	Filter	UVPI Gain Step	NER for Single Image (W/sr-cm <sup>2</sup> )	Number of Images Superposed	NER for Data Interval (W/sr-cm <sup>2</sup> )
1	PC-4	9	$2.3 \times 10^{-6}$	140	$1.8 \times 10^{-8}$
2	PC-3	13	$1.6 \times 10^{-5}$	61	$2.7 \times 10^{-7}$
3	PC-2	12	$7.8 \times 10^{-6}$	96	$8.1 \times 10^{-8}$
4	PC-1	12	$1.2 \times 10^{-5}$	88	$1.4 \times 10^{-7}$

Table 25 summarizes the estimated NERs, or sensitivity levels, for the four data intervals for the tracker camera under the assumption of the reference spectrum. The last column expresses the sensitivity level in photoevents/s. As opposed to the plume camera data, for the tracker camera and its lower gain settings the signal-independent noise is not negligible and the improvement in sensitivity is not linear with the number of images superposed.

Table 25 – Tracker Camera NER Per Pixel for Data Intervals

Data Interval	NER for Single Image (W/sr-cm <sup>2</sup> )*	Number of Images Superposed	UVPI Gain Step	NER for Data Interval (W/sr-cm <sup>2</sup> )*	Minimum Detectable Number of Photoevents/s for Superposed Images*
1	$1.8 \times 10^{-8}$	36	6	$2.5 \times 10^{-9}$	152
2	$1.8 \times 10^{-8}$	16	6	$3.8 \times 10^{-9}$	231
3	$1.8 \times 10^{-8}$	23	6	$3.2 \times 10^{-9}$	192
4	$2.4 \times 10^{-8}$	21	5	$4.9 \times 10^{-9}$	293

\*Not redleak corrected

## 5.0 SPATIAL FEATURES

This section concentrates on the spatial characterization of the measured plumes. First, definitions for the plume central region and outer region are presented. Second, the plume's spatial extent is discussed with consideration for the UVPI's point spread function (PSF). Finally, the observed plume is compared to the CHARM 1.4 model predictions.

### 5.1 Delineation of Plume Central and Outer Regions

Because of the generally low signal statistics in a single image, an accurate delineation of the plume central or outer region is not possible from a single image. Hence, an average of superposed images (a composite image) is used to define the plume central region extent for each of the four intervals.

Definition of the central region was begun by selecting all pixels in the composite image for which the radiance was at least 25% of the brightest pixel radiance. The resulting region was expanded further by performing a dilation with a square window of 5 by 5 pixels. By using this criterion, the region defining the plume central region is depicted in Fig. 39. The images on the left are the composite images; in the images on the right, the corresponding central region is overlaid as a completely white region. Figure 39 shows the four intervals for the LCLV third-stage burn.



Fig. 39 - Highlighted plume central regions for LCLV third stage

Table 26 summarizes the central region extent in pixels for each of the four data intervals considered.

Table 26 - Central Region Extent in Plume Camera

Interval	Filter	Central Region Extent (pixels)	Central Region Extent (m <sup>2</sup> )
1	PC-4	205	6595
2	PC-3	192	5873
3	PC-2	166	5006
4	PC-1	246	7646

For the tracker camera, the central region was defined as all those pixels that overlap the plume-camera field of view. Hence, in this report, the central region for the tracker camera is not defined over the same area as for the plume camera.

From the point of view of phenomenology, an argument can be made that the central region definition above does not fully contain the plume core. To validate the definition of the plume central region, additional consecutive dilation operations were performed to force the defined central region to become larger. As an example, Fig. 40 shows the number of photoevents per image in the central and outer regions as a function of central region size for data interval 1. A vertical dashed line is used to illustrate the central region size used in this report. This plot can be used to scale the results presented here if a different central region size is desired.

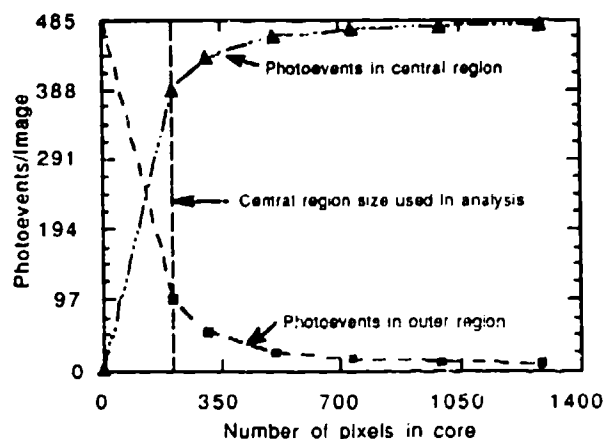


Fig. 40 - Photoevents as a function of defined central region size, LCLV thru stage interval 1

Although these figures show that the outer region contributes somewhat to the total signal measured during each interval, the composite images clearly show that the outer region signal is only weakly localized to the area behind the rocket. For this reason, it is concluded that: (a) the outer region component of the total signal is only weakly attributable to plume induced far-field emissions, and (b) central region results most accurately represent the true plume radiance.

## 5.2 Plume Extent and Point Spread Function

The effective UVPI point spread function (PSF) is defined as the response of the instrument to a point source, e.g., a star or a ground-based beacon. An understanding of the UVPI plume

camera's PSF is critical in establishing the maximum size of the observed LCLV third-stage plume. Table 27 summarizes the estimated plume central region axial length, as defined from peak to either 50% or 10% of peak brightness, for each data interval during the third-stage burn. These plume length estimates do not incorporate corrections for the aspect angle or for the plume camera's PSF.

Table 27 - Observed Axial Length of Plume Central Region

Interval	Filter	Peak to 50% Maximum (m)	Peak to 10% Maximum (m)
1	PC-4	30	90
2	PC-3	14	39
3	PC-2	16	38
4	PC-1	45	84

Based on UVPI data from many observations, one may conclude that the plume camera's PSF depends on the observation modality, i.e., downward looking vs sideward looking. Sideward-looking observations use the door-mounted mirror but downward looking observations do not. Observation of the LCLV third-stage plume did not use the door-mounted mirror. The existing data for point sources indicate that the PSF is less circularly symmetric when using the door-mounted mirror. This could be the result of jitter in the door mirror.

Figure 22 shows a plume camera image of a ground-based beacon. A scaled version of the plume camera's PSF for the beacon is presented in Ref. 1. Figure 41 shows a three-dimensional plot of the PSF that results from observation of the ground-based beacon. For the ground-based beacon, the axial length of the PSF from peak to 50% of the peak along the major axis is about 4 pixels or 20 m at a range of 450 km, as shown in Fig. 42. The full-width-half-maximum length is about 40 m.

Figures 43 through 46 show profiles of the radiance along the major axis of the plume, measured by the plume camera, for each of the data intervals. The horizontal line in Figs. 44 through 46 corresponds to the NER sensitivity limit after image superposition. The NER sensitivity limit for data interval 1 is not distinguishable from the abscissa in Fig. 43. It is evident from these figures that, after image superposition, a good SNR was achieved for all intervals.

Figure 34 shows a tracker-camera image of a ground-based beacon. A scaled version of the tracker camera's PSF for the beacon is presented Ref. 1. Figure 47 shows a three-dimensional plot of the PSF that results from observation of the ground-based beacon; Fig. 48 is an axial profile of the beacon as seen by the tracker camera.

### 5.3 Comparison of Results to CHARM 1.4 Predictions

This subsection compares the UVPI measurements to the predictions provided by a theoretical plume model. The Institute for Defense Analyses (IDA) generated a number of CHARM 1.4 runs in which the LCLV third stage was modeled by using each of the UVPI's plume-camera filter bandpasses [18]. The following parameters were common to all the runs:

Model:	CHARM 1.4
Object modeled:	Intrinsic Core
Aspect for four data intervals:	27.2, 24.4, 25.6, 34.1
Horizontal resolution:	5.0 m
Vertical resolution:	5.0 m

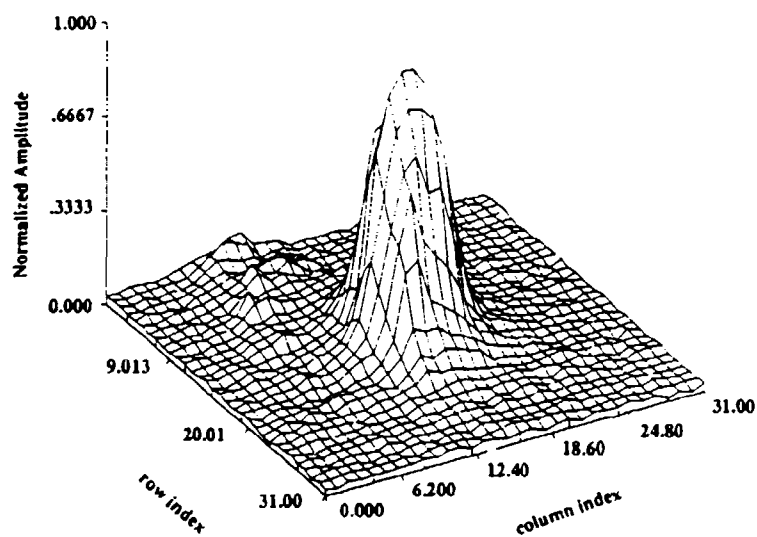


Fig. 41 - Plume camera PSF for ground-based beacon

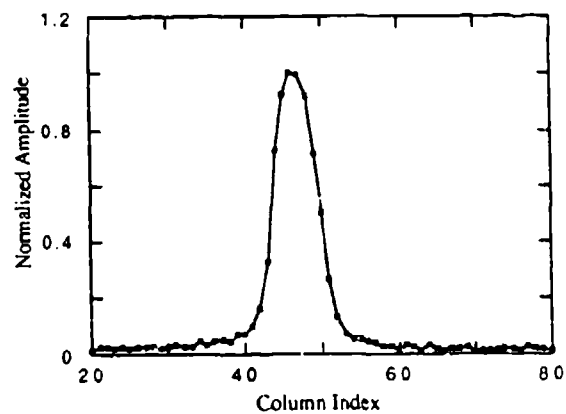


Fig. 42 - Axial profile through plume camera PSF for ground-based beacon

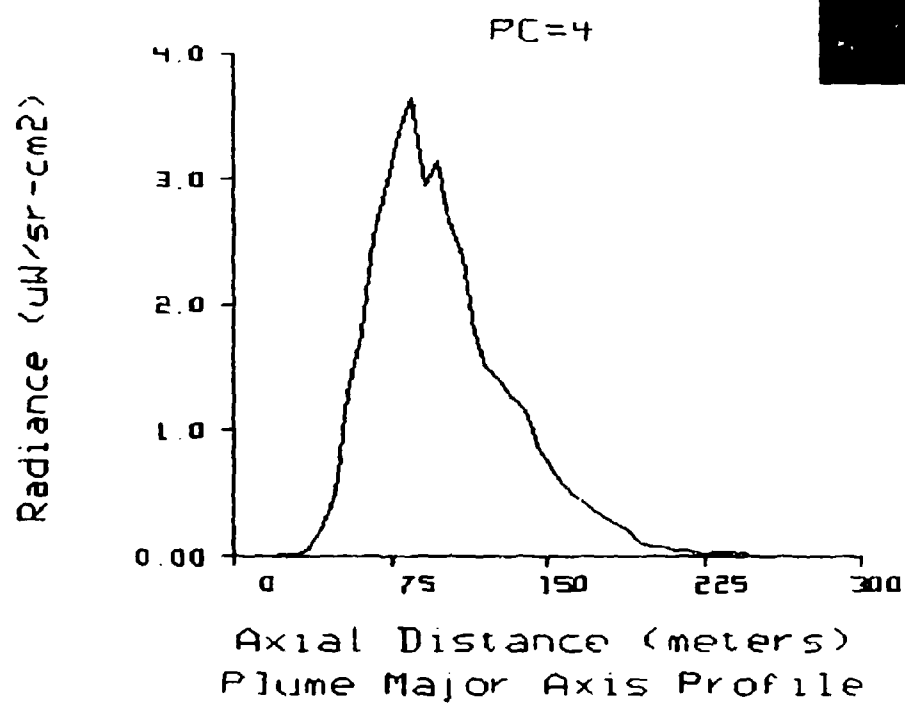


Fig. 43 - Axial profile along plume central region for data interval 1, plume camera

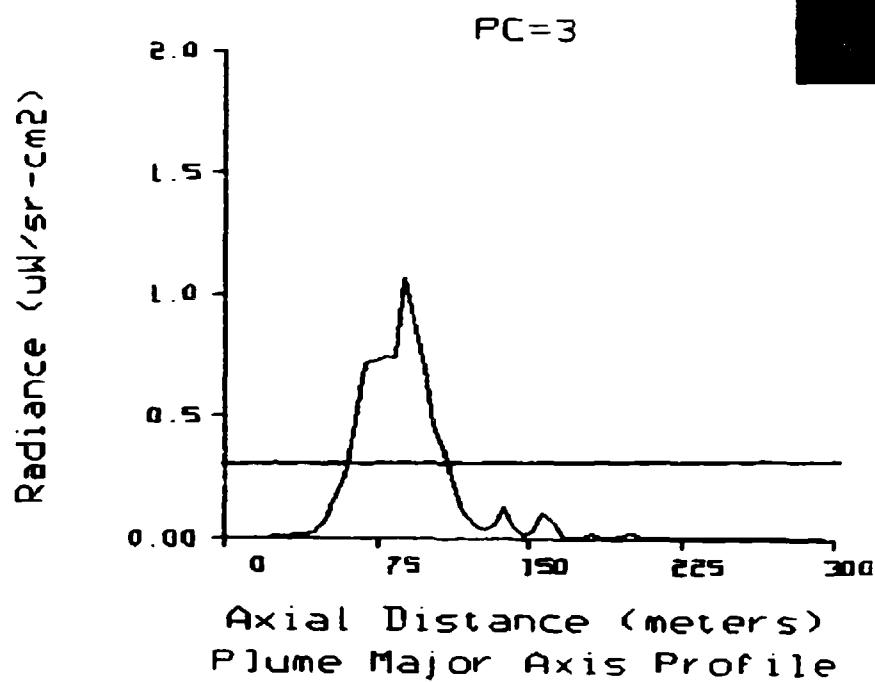


Fig. 44 - Axial profile along plume central region for data interval 2, plume camera



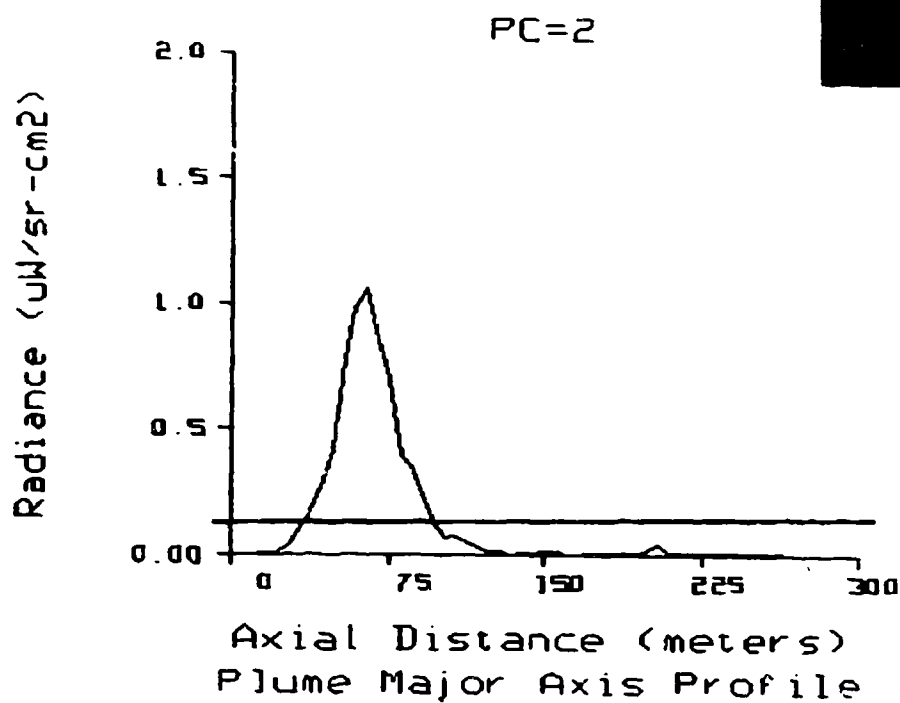


Fig. 45 - Axial profile along plume central region for data interval 3, plume camera

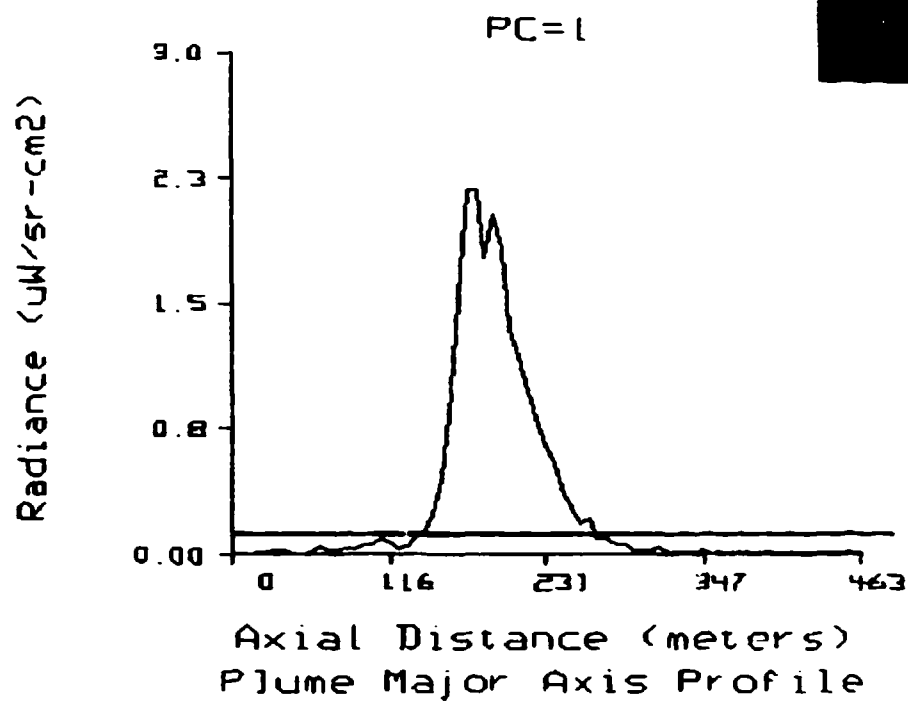


Fig. 46 - Axial profile along plume central region for data interval 4, plume camera

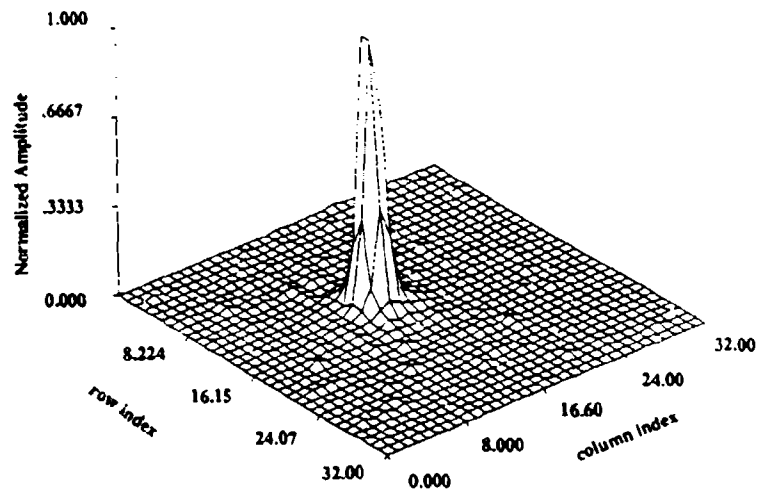


Fig. 47 - Tracker camera PSF for ground-based beacon

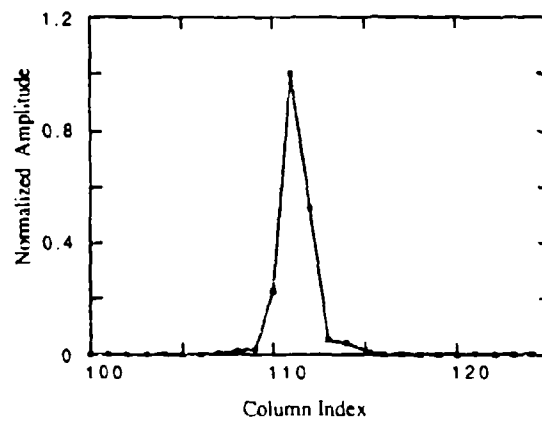


Fig. 48 - Axial profile through tracker camera PSF for ground-based beacon

In all of IDA's runs, a 5 by 5 m pixel resolution was used. To compare the CHARM 1.4 predictions with the UVPI measurement, the CHARM 1.4 predictions were convolved with an estimate of the UVPI's PSF. A normalized version of the ground beacon image, Frame 12778, Orbit 1173, was used as the best UVPI plume-camera PSF estimate.

Figures 49 and 50 show an example of the CHARM 1.4 prediction convolved with the UVPI point spread function (PSF). The left image in Fig. 49 shows a false-color CHARM 1.4 image prediction with 5-m resolution for the third-stage motor, assuming it is being observed with PC-4. The right image shows the same CHARM 1.4 prediction, except that it is convolved with the UVPI point spread function. Figure 50 is the corresponding contour plot for the image prediction, again assuming UVPI PC-4 and convolution with UVPI PSF.

Figures 51 through 54 show: (a) the CHARM 1.4 high-resolution prediction of the plume radiance as a function of axial distance, (b) the CHARM 1.4 prediction convolved with the UVPI plume camera PSF, and (c) a horizontal line depicting the single image noise equivalent radiance (NER) of the plume camera, for the various filter bandpasses. The interval NER values are given in the upper right-hand corner.

The peak radiance and the plume length for the CHARM 1.4 image predictions are listed in Tables 28 and 29.

## 6.0 TEMPORAL FEATURES

This section presents calibrated photoevents per image and radiant intensity values for each of the four data intervals. The calibration procedure is described in Section 3. The conversion to radiant intensity is performed by using a reference emission spectrum for incandescent alumina particles that is typical of the emission spectrum produced by solid-fuel rocket motors containing ammonium perchlorate/aluminum. The latter is similar to the model used in the CHARM 1.4 code. The bandpasses of each of the plume camera filters are also given in Section 1.2. Section 6.1 presents the plume-camera observations; Section 6.2 presents the tracker-camera observations.

### 6.1 Plume Camera Intensity Plots

This section presents the number of photoevents observed in the plume camera, both central region and total, for each image of the four analyzed data intervals. Table 30 lists the figures contained in this section.

The separation of plume central region from total FOV is described in Section 5.1. During the telemetry frame ranges depicted in each plot, the plume-to-tracker image ratio was primarily 8:2. Consequently, the plots show repeated groups consisting of eight consecutive plume camera images followed by a gap where the two tracker camera images occurred.

In addition to the intensities, the figures include: the estimated local mean, which is a running average of the intensity, and a threshold of 3.1 standard deviations above the local mean, which flags intensity values that are highly unlikely (probability less than 0.001) based on local statistics. The local statistics are computed by using a running window of 15 frames for plume-camera data. Section 4.6 provides a more complete discussion of the computations of local statistics.

Figures 55 through 62 convey information useful for indexing those frames or times at which a significant statistical deviation in the intensity is observed, based on the local statistics, and for showing the intensity variation over both the plume central region and the total plume.

CHARM 1.4 Prediction  
Using 5 Meter Resolution

CHARM 1.4 Prediction  
Using UUPI's PSF

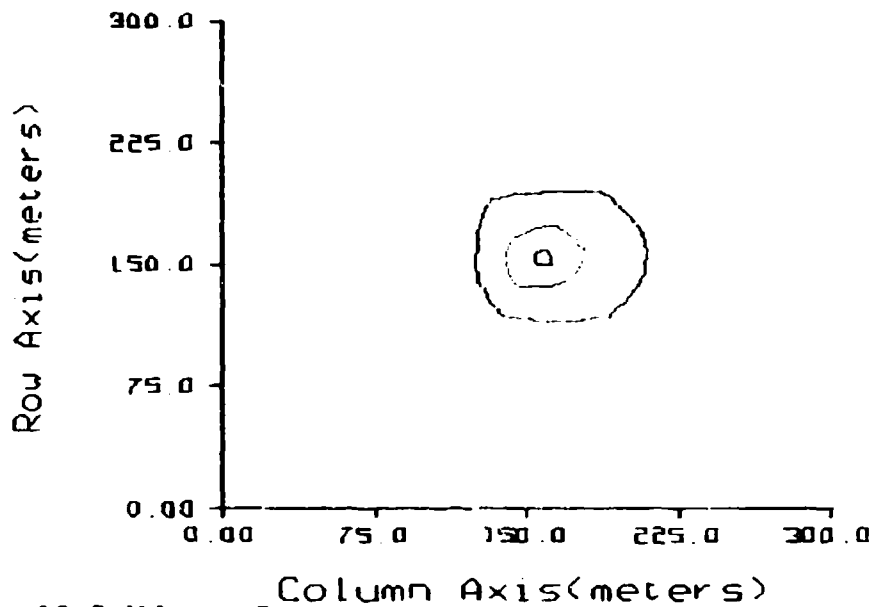


max=242.5 uW/sr-cm2

$I = 0.095 \times \text{max}$   $I = 0.50 \times \text{max}$   $I = 0.95 \times \text{max}$

NRL/ACT 6/15/92

Fig. 49 - CHARM 1.4 prediction for the LCLV rocket motor for PC-4 before and after smearing



max=16.9 uW/sr-cm2

$I = 0.095 \times \text{max}$   $I = 0.50 \times \text{max}$   $I = 0.95 \times \text{max}$

NRL/ACT 8/20/92

Fig. 50 - A contour plot of the CHARM 1.4 prediction for LCLV blurred by the plume camera PSF

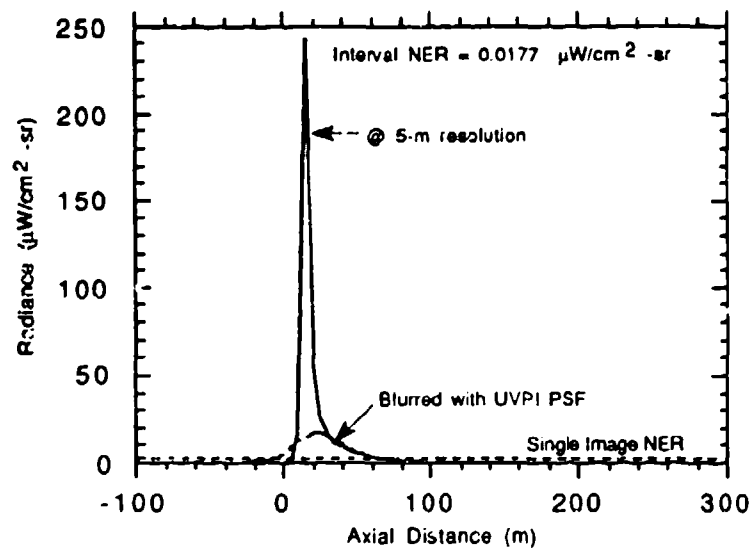


Fig. 51 - CHARM 1.4 predicted axial profile for PC-4 before and after smearing

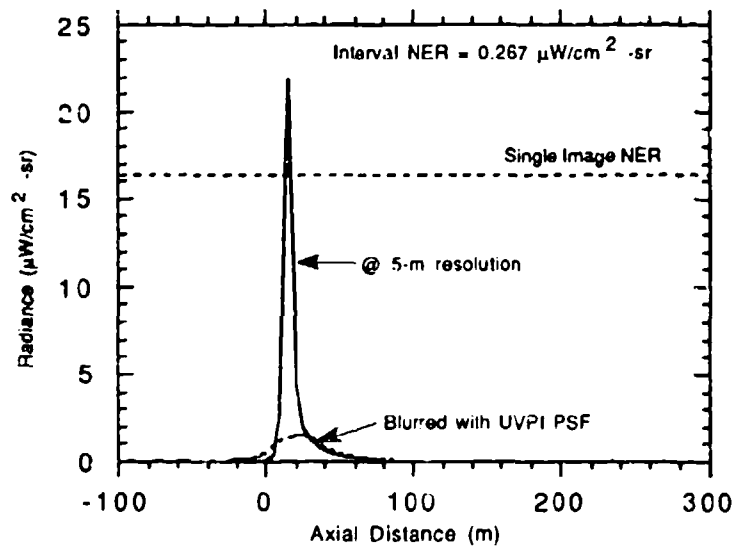


Fig. 52 - CHARM 1.4 predicted axial profile for PC-3 before and after smearing

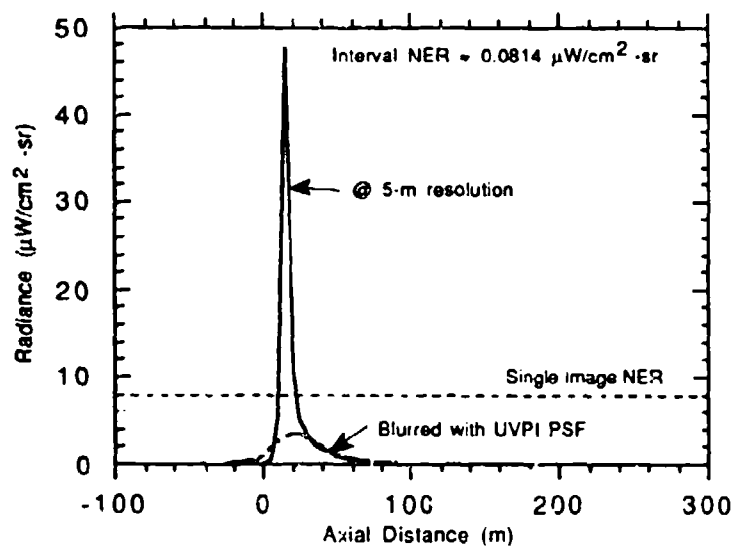


Fig. 53 - CHARM 1.4 predicted axial profile for PC-2 before and after smearing

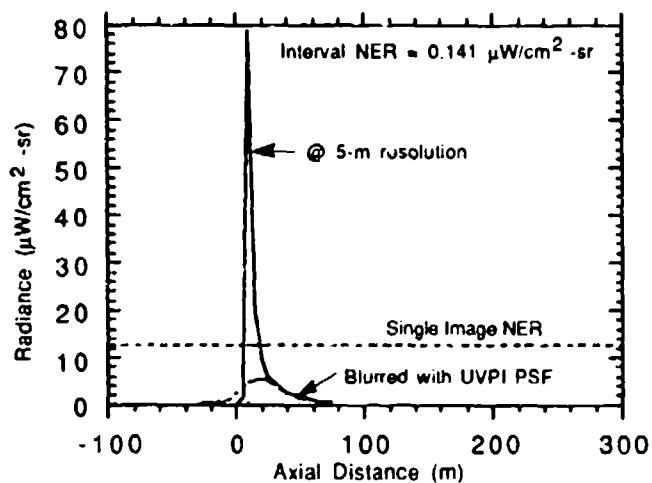


Fig. 54 - CHARM 1.4 predicted axial profile for PC-1 before and after smearing

Table 28 - Peak Radiance Comparison

Interval	Filter	CHARM 1.4 @ 5-M Resolution Peak Radiance ( $\mu\text{W}/\text{sr}\cdot\text{cm}^2$ )	CHARM 1.4 Convolved Peak Radiance ( $\mu\text{W}/\text{sr}\cdot\text{cm}^2$ )	UVPI Measured Peak Radiance ( $\mu\text{W}/\text{sr}\cdot\text{cm}^2$ )
1	PC-4	$2.48 \times 10^2$	$1.69 \times 10^1$	3.65
2	PC-3	$2.19 \times 10^1$	1.54	1.07
3	PC-2	$4.76 \times 10^1$	3.50	1.06
4	PC-1	$7.88 \times 10^1$	5.42	2.17

Table 29 - Comparison of Measured to Predicted Plume Length

		Plume Length (m) Peak to 50% and Peak to 10%					
Interval	Filter	CHARM 1.4 @ 5-M Resolution		CHARM 1.4 Using UVPI's PSF		UVPI Measured	
		50%	10%	50%	10%	50%	10%
1	PC-4	5	15	30	60	30	90
2	PC-3	5	10	30	55	14	39
3	PC-2	5	15	30	60	16	38
4	PC-1	5	15	30	65	45	84

Table 30 - Radiant Intensity Figures

Interval	Total	Central Region
1	55	56
2	57	58
3	59	60
4	61	62



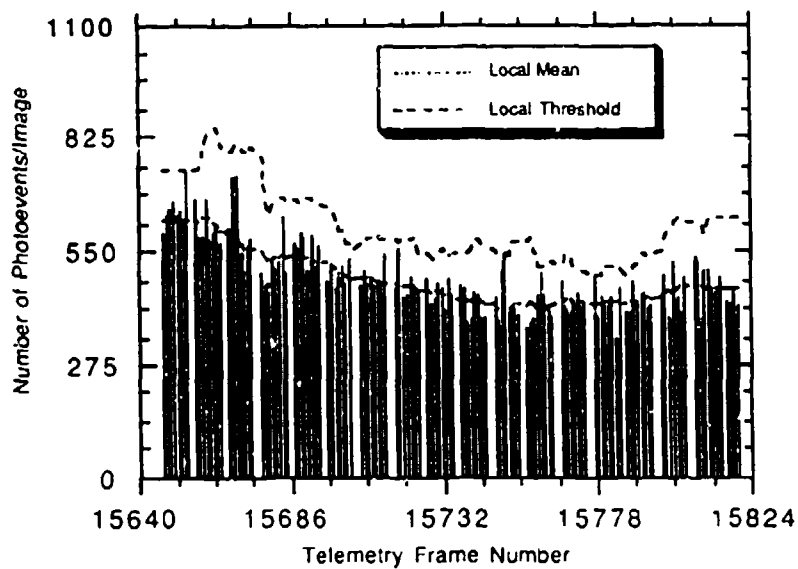


Fig. 55 - Plume camera, total intensity for interval 1

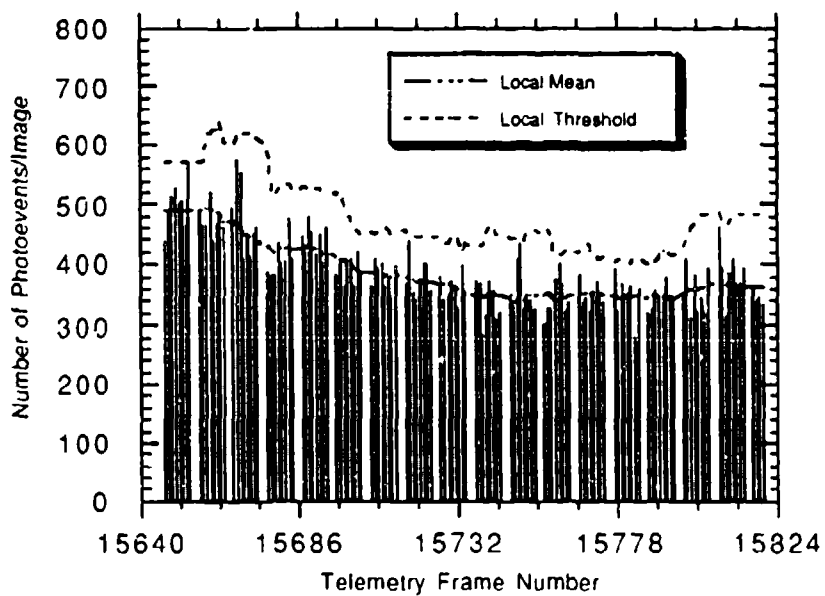


Fig. 56 - Plume camera, central region intensity for interval 1

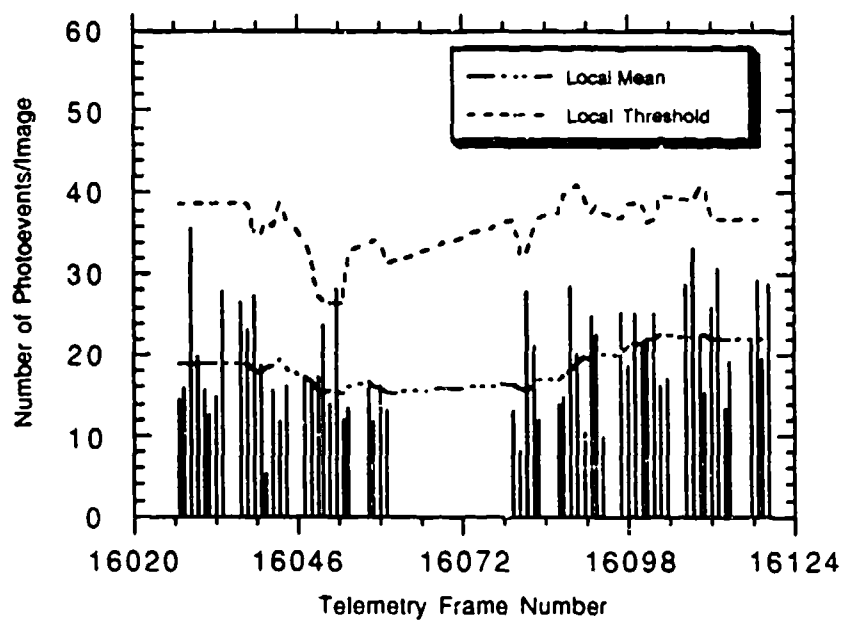


Fig. 57 - Plume camera, total intensity for interval 2

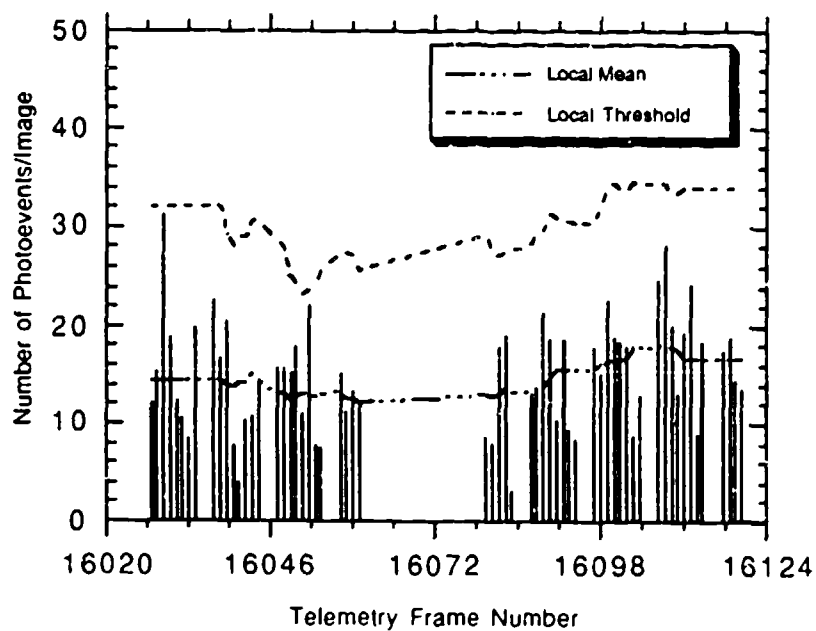


Fig. 58 - Plume camera, central region intensity for interval 2

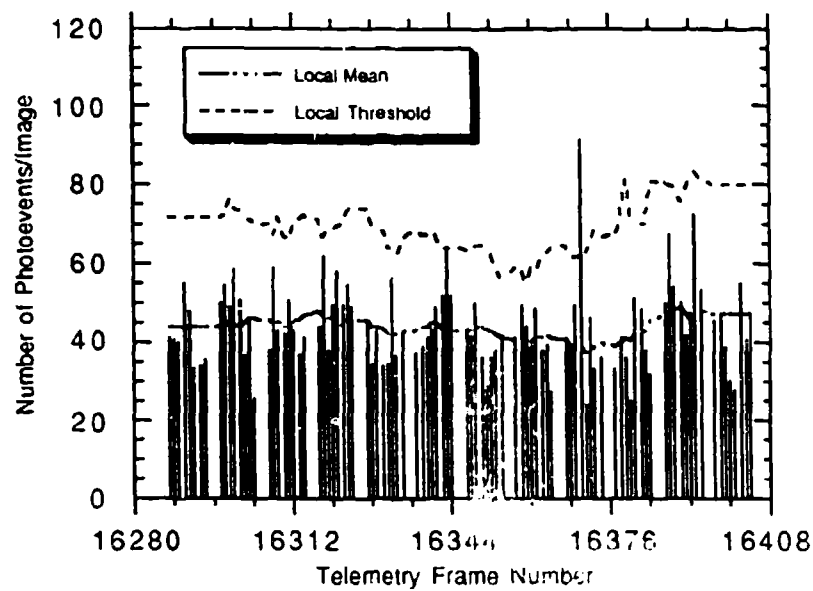


Fig. 59 - Plume camera, total intensity for interval 3

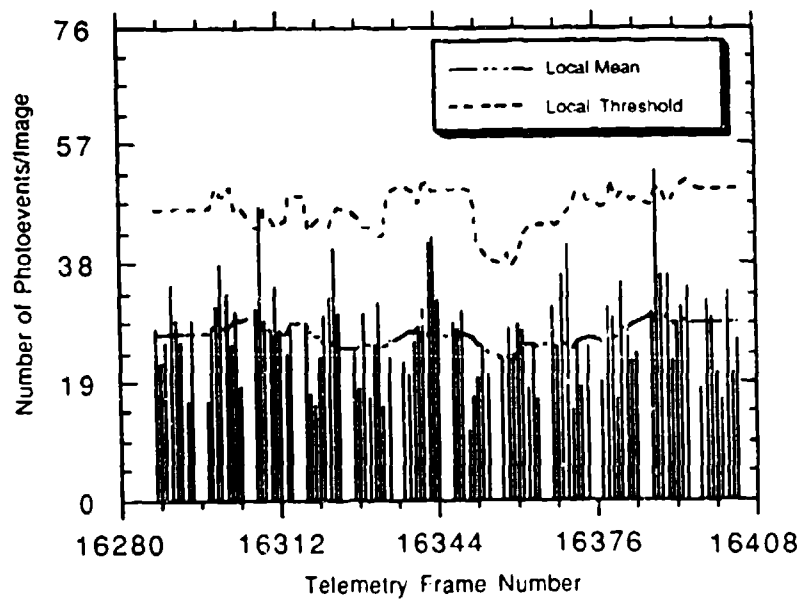


Fig. 60 - Plume camera, central region intensity for interval 3

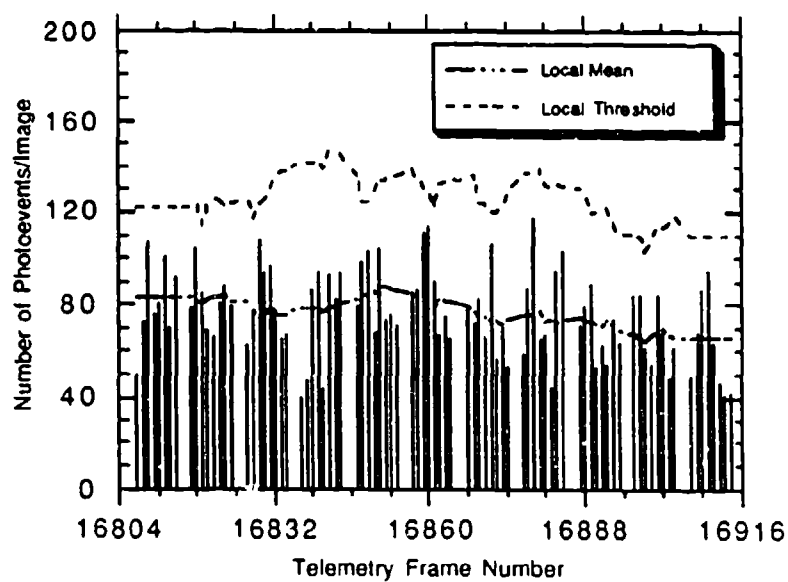


Fig. 61 - Plume camera, total intensity for interval 4

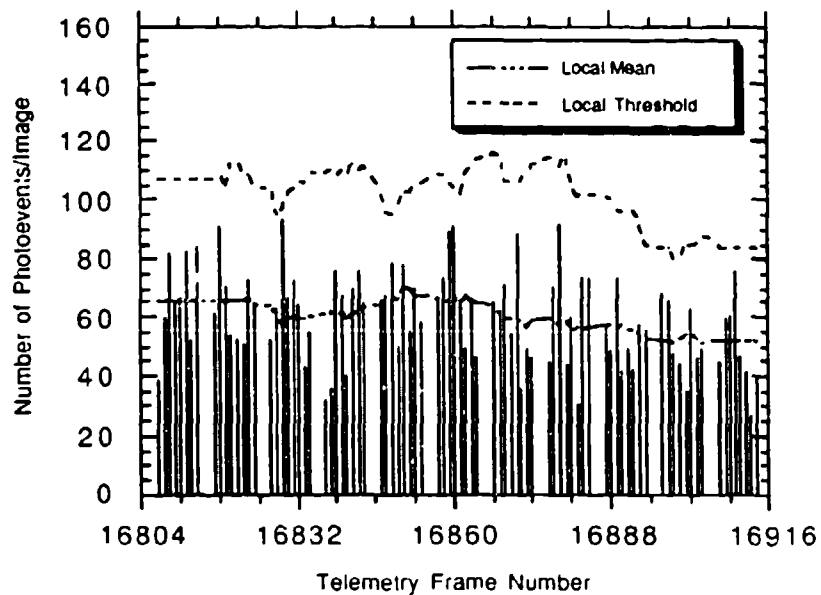


Fig. 62 - Plume camera, central region intensity for interval 4

Figures 57, 59, and 60 show instances in which the measured number of photoevents exceed the local mean by more than 3.1 standard deviations. The probability of such an event is less than 0.001. Therefore, all instances in which the measured number of photoevents exceeded the threshold were investigated in great detail. No significant difference was observed in the composite images after disregarding the images where the major number of photoevents exceeded the threshold.

Table 31 summarizes the average radiant intensities (ARI) for the plume-camera observations over the four data intervals. The average radiant intensity reported for each of the data intervals is based on the reference spectral energy distribution assumption. It represents the average of all images in the interval. Table 31 includes reference spectrum predictions of ARI for the sake of completeness. It is not obvious how to compare the predictions to the experimentally determined values because of different fields of view and complexities with regard to central and outer region mechanisms.

Table 31 – Summary of Plume-Camera Average Radiant Intensities

Interval	Filter	Band (nm)	Measured ARI*		Measured ASRI**		Reference Model
			Central Region ARI (W/sr)	Total ARI (W/sr)	Centroid Wave-length (nm)	Total ASRI (W/sr- $\mu$ m)	Predicted ARI (W/sr)
1	PC-4	235-350	67.9	85.1	305	806	806
2	PC-3	195-295	17.1	23.1	265	221	77.2
3	PC-2	300-320	15.0	24.8	310	1217	987
4	PC-1	220-320	55.3	70.0	280	467	207

\*average radiant intensity

\*\*average spectral radiant intensity

When operating in the zoom image transmission rate, each telemetry frame contains one image.

## 6.2 Tracker-Camera Intensity Plots

Figures 63 through 66 present total photoevents per image for the four data intervals. The figures in this section are based on a 19 by 19 pixel section of the tracker camera, which corresponds approximately to the total field of view of the plume camera. This field of view contains plume central region and a portion of the outer region. To provide an estimate of the average radiant intensity, values based on reference spectral energy distribution assumptions are reported in Table 32 for the tracker-camera observations. These results have been reduced by 16.3% to account for red leakage in the tracker-camera filter.

Figures 63 through 66 are primarily intended to show image-to-image variations in the number of photoevents per image after redleak correction. For the telemetry frame ranges depicted in each plot, the plume-to-tracker image ratio was 8:2. Consequently, the plots show repeated groups consisting of two consecutive tracker-camera images followed by a gap where the eight plume camera images occurred. Because of the small number of images in each data interval, an estimated local mean and a low probability threshold could not be meaningfully computed.

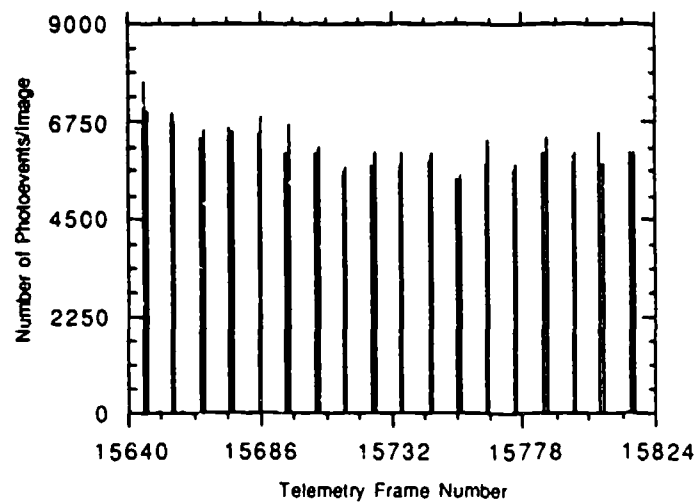


Fig. 63 - Tracker camera total intensity for interval 1

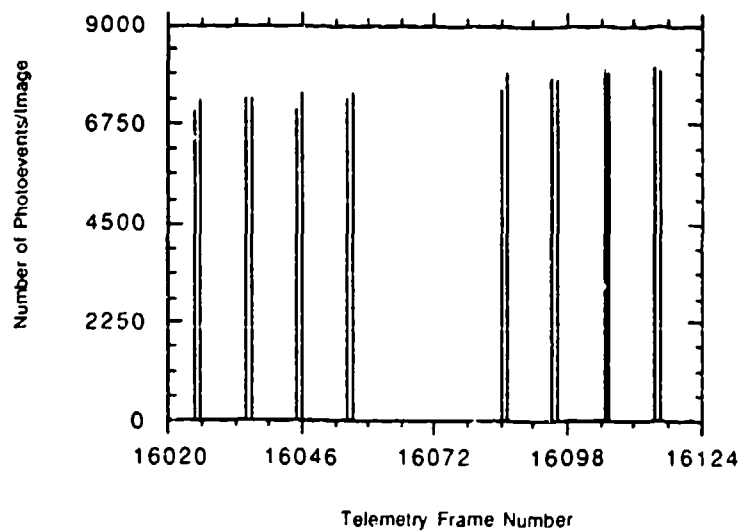


Fig. 64 - Tracker camera total intensity for interval 2

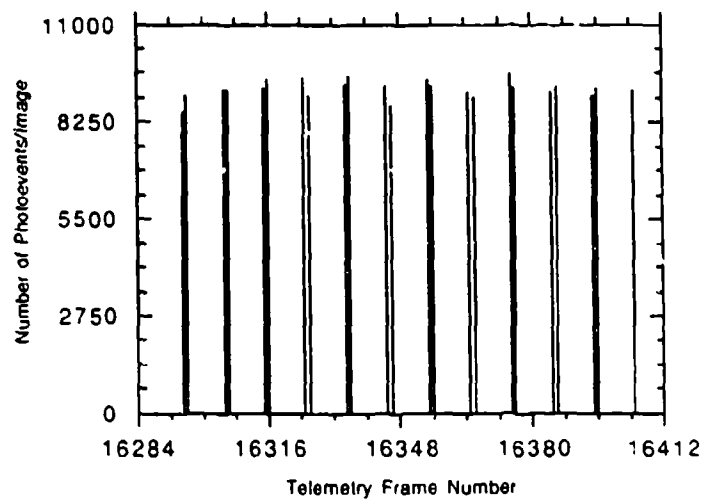


Fig. 65 - Tracker camera total intensity for interval 3

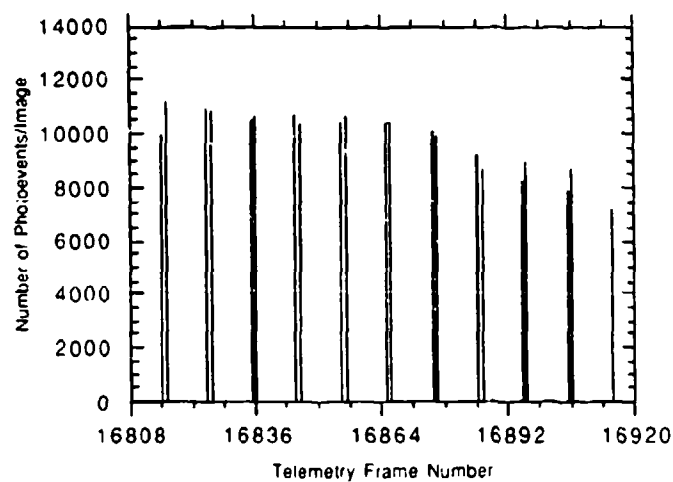


Fig. 66 - Tracker camera total intensity for interval 4

Table 32 – Summary of Tracker-Camera Average Radiant Intensities

Interval	Filter	Band (nm)	ARI* in 19 x 19 Pixel Region (W/sr)	ASRI** in 19 x 19 Pixel Region @ 390 nm (W/sr- $\mu$ m)
1	PC-4	255-450	549	4380
2	PC-3	255-450	638	5090
3	PC-2	255-450	763	6090
4	PC-1	255-450	664	5300

\*average radiant intensity

\*\*average spectral radiant intensity

## 7.0 SPECTRAL ANALYSIS OF PLUMES

This section presents the spectral analysis of the emission from the LCLV third-stage plume central region and from the outer region. As discussed in Section 2, the UVPI plume and tracker cameras observed the stage at a range of approximately 492 km by using a sequence of bandpasses. The figures and tables in this section show the computed spectral radiant intensity in W/sr- $\mu$ m of the plume central region and the spectral radiant intensity measured over the entire plume-camera field of view. The UVPI observations of the central region show that the ratio of the spectral radiant intensity at the longer wavelengths, relative to the spectral radiant intensity at the shorter wavelengths, is smaller than predicted by the reference spectrum. The results for the entire plume-camera field of view show a similar relative excess at the shorter wavelengths.

### 7.1 Observed Spectral Radiant Intensities

The conversion of the plume and tracker camera data to radiometric values requires the assumption of a source spectrum, as described in Section 3.5. The reference spectral shape was used in the analysis of the camera data presented in this section. The wavelength for which the spectral radiant intensity is reported for each filter bandpass is the centroid wavelength when the assumed source spectrum is convolved with the UVPI net quantum efficiency function, as described in Section 3.6.

In selecting the reference spectrum scaling factor, an effort was made to find a good fit for all bands. This method is less sensitive to single band signals but instead compares overall spectral shapes.

The plume-camera observations were made between 81 and 124 s after liftoff. The range from UVPI to the rocket was between 492 and 501 km over this time period. The spectral radiant intensities of the plume central region, as measured by UVPI in the four plume-camera bands, are plotted in Fig. 67. In addition, Fig. 67 shows the reference spectral shape, scaled arbitrarily to pass through the data points, and for comparison shows a blackbody spectrum chosen to coincide with the reference spectral shape at short wavelengths. The data and scaled reference based values are also listed in Table 33. Note that the average radiant intensities of the plume changed with time during the four data intervals. Consequently, the relative spectral intensities must be compared with caution.

Figure 67 shows that the ratio of the spectral radiant intensity measured by UVPI for the central region at the shorter wavelengths, relative to that at the longer wavelengths, is larger than that predicted by the reference spectral shape. The relative intensity increase for the 265-nm data point is a factor of almost three, well beyond the instrument uncertainty discussed in Section 4.6.

The spectral radiant intensity measured by UVPI over the entire plume camera field of view is shown in Fig. 68. These measurements were made by the plume camera operating in the four plume



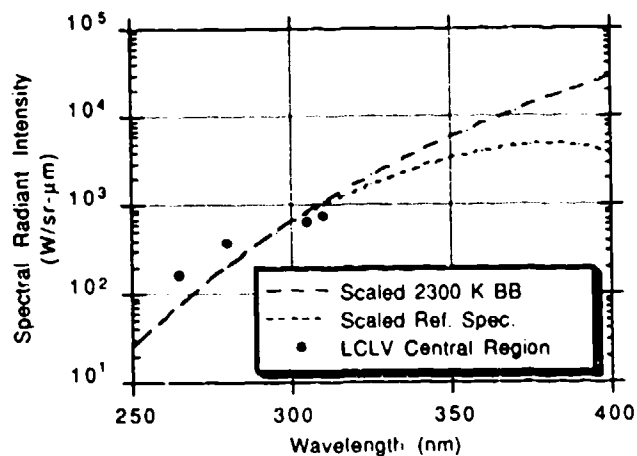


Fig. 67 – Measured spectral radiant intensity for the LCLV plume central region

Table 33 – Measured and Scaled Spectral Radiant Intensity in Units of W/sr-μm

Wavelength (nm)	Filter	Observed Central Region	Plume Camera Field of View	Central Region: Scaled Reference Comparison
265	PC-3	$1.63 \times 10^2$	$2.21 \times 10^2$	$7.72 \times 10^1$
280	PC-1	$3.69 \times 10^2$	$4.67 \times 10^2$	$2.07 \times 10^2$
305	PC-4	$6.43 \times 10^2$	$8.06 \times 10^2$	$8.06 \times 10^2$
310	PC-2	$7.36 \times 10^2$	$1.22 \times 10^3$	$9.87 \times 10^2$

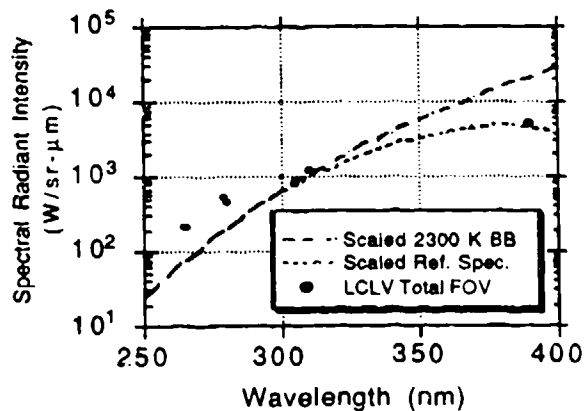


Fig. 68 – Measured spectral radiant intensity for the LCLV plume camera field of view

camera bands and by the tracker camera. Note that the tracker camera pixels analyzed in this section correspond to the full field of view of the plume camera. Figure 68 also shows a scaled reference spectral shape and blackbody spectrum. The plume camera data are also listed in Table 33.

Figure 68 shows that the reference spectral shape is in good agreement with the 275 to 390-nm trend. It also shows that the reference model predicts a more rapid decrease with decreasing wavelength below 275 nm than the data show. These results are similar to those found for the plume central region analysis. Note that the LCLV total and central region spectra data are almost identical, both showing the short wavelength excess.

## 7.2 Discussion

The reference model hypothesizes that the principal source of UV radiation is thermal emission from alumina particles at the fusion temperature of alumina, 2320 K. The spectral shape departs from that of a blackbody because of the decreasing effective emissivity of the particles with increasing wavelength. No obvious modification to this model will yield the far-UV excess evident in the UVPI data. A plausible hypothesis is that an additional emission mechanism is producing the excess UV emission. Spectral line emission by exhaust gases and by the mesospheric atmosphere disturbed by the rocket, e.g., CO Cameron and NO<sub>y</sub> bands are possible sources.

## 8.0 PERSISTENT CLOUDS OR TRAILS

The interval 4 tracker-camera composite image presented in Section 4, Fig. 38, clearly shows a faint cloud trail forming behind the rocket. Although gain changes and ensuing transients following data interval 4 (frame 16915, TALO 123.9 s) rendered the data unreliable for inclusion in the analysis, images were collected until UVPI lost track on the LCLV third stage (frame 17306, TALO 136.9 s). These images showed a very prominent cloud trail that exhibited unusual behavior.

Figure 69 shows a composite tracker camera image formed from frames 17055 and 17056, around TALO 128.6 s. The brightest pixel in the central region of the plume registers approximately 9400 photoevents/s, which is more than a factor of 10 lower than the value measured during data interval 4. Consequently, the cloud is much more conspicuous, relative to the central region, in Fig. 69 than in Fig. 38 of Section 4.

The cloud began to change in appearance around frame 17135, TALO 131.2 s, immediately following a brief loss of track. Figure 70 shows a composite image formed from frames 17135 and 17136. The aspect angle and angle of attack for the third stage is no different than that associated with Fig. 69, but an extension of the cloud trail, apparently to the side or front of the rocket, is clearly evident. This cloud extension seems to be correlated with a loss of thrust that occurred at approximately the same time.

## 9.0 COMPARISON OF LCLV WITH OTHER TEST FLIGHTS

In this chapter the LCLV data is discussed in comparison with other test flights. In all, UVPI observations were made for four rocket launches: Nihka [19], Starbird [20], LCLV, and Strypi [2] in that order. Two features of the data appeared common to most flights and are worthy of comment.

The first common feature is the apparent excess in the far UV,  $\lambda < 300$  nm, relative to that expected from the reference spectrum. This UV excess is described in section 9.1 as it appears in the various tests. The second feature is the presence, in three tests, of a UV luminous outer region beyond the brightest part of the plume. This outer region is discussed in Section 9.2.



Fig. 69 - Cloud trail around TALO 128.6 s



Fig 70 - Cloud trail around TALO 131.2 s

### 9.1 The Far-UV Excess

The UVPI data from the LCLV and the other plumes were analyzed by using the reference spectral shape (Fig. 71), and discussed in detail in Section 3.4. Backward-looking spectrometers flying on the Strypi rocket made direct measurements of the plume central region and showed spectra for the Antares and Star 27 motors that matched the reference spectrum well [14], as can be seen by comparing Fig. 72 with Fig. 71. However, comparison of UVPI total field of view spectral radiance plots for Nihka (Fig. 73), Starbird stages 3 and 4 (Fig. 74), LCLV stage 3 (Fig. 75), and Strypi stages 3 and 4 (Figs. 76 and 77) show that a far-UV excess appears in all data sets. This UV excess appears to be a generic feature of aluminized solid-fuel rocket motor plumes, since the rocket motors varied in size, performance, and detailed fuel composition. The cause of the UV excess may be UV luminous gases such as excited NO and CO with line emissions that outshine the incandescent alumina particles in the far UV. Such an effect was predicted in preflight analysis of the rocket test series [7].

### 9.2 Luminous Plume Outer Region

It was useful for spatial analysis of the rocket plumes to divide the plume into a central and outer region. The central region, approximately defined in Section 5.1 as the pixels within 25% or greater of the maximum pixel brightness, was thought to primarily consist of incandescent alumina particles. The outer region might contain major contributions from molecular luminescence occurring in shock or mixing layers.

Evidence of outer region luminescence was strongly present in two tests: Nihka and Strypi (Figs. 78 and 79). It was weakly present in LCLV (Fig. 80), and was not seen in Starbird (Fig. 81). The luminous outer region was most prominent in either PC-1 or PC-3, which measure far-UV rather than mid- or near-UV. This might suggest that the outer region owed some of its luminosity to molecular radiance in shock or mixing layers. The outer region was most strongly present at higher altitudes. Thus, the source may consist of UV luminous gases in the plume that may expand outward at high altitudes but be confined in the plume core at low altitudes. This correlation between altitude and apparent UV luminous outer regions can be seen in Fig. 82, which shows the altitude range during observation for each flight.

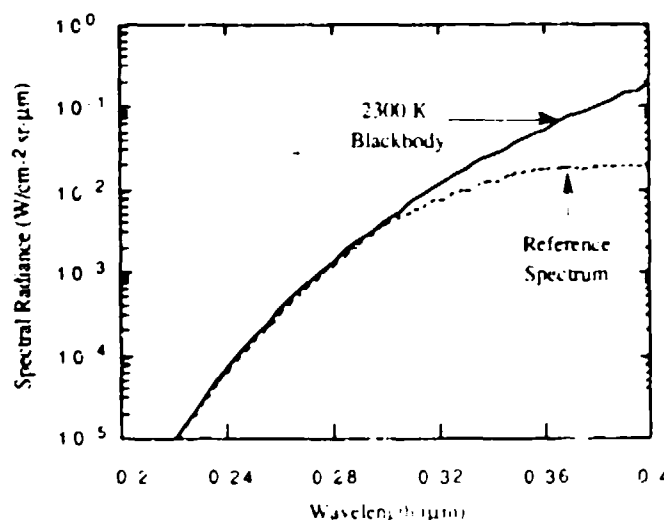


Fig. 71 - Assumed reference spectrum

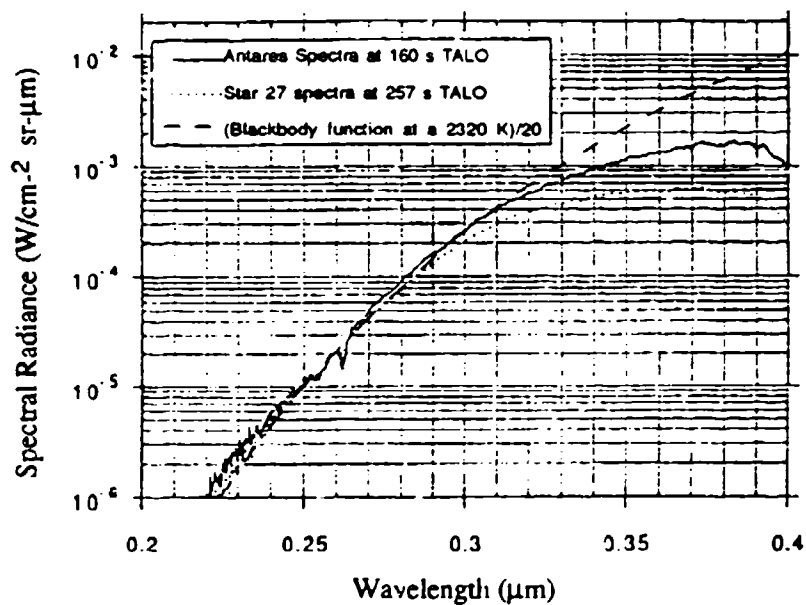


Fig. 72 - On-board spectrometer measurement for Strypi mission [14]

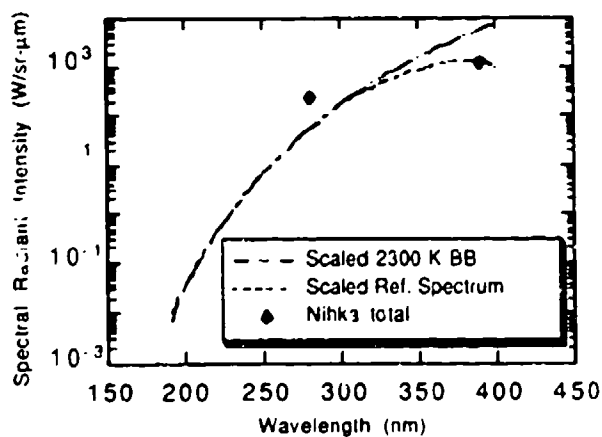


Fig. 73 - Measured spectral radiant intensity of the Nihka for the plume camera total field of view

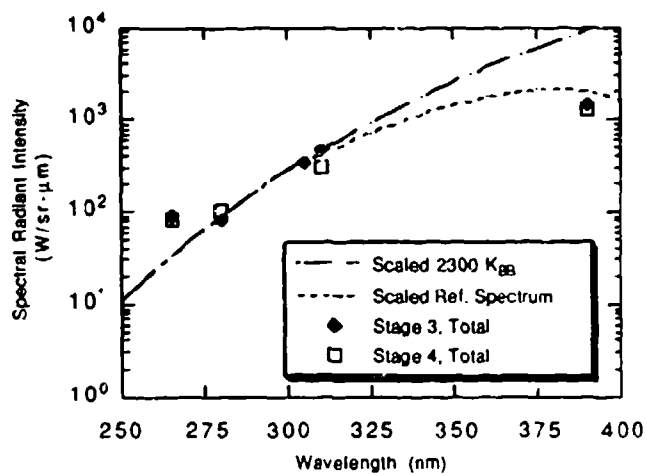


Fig. 74 – Measured spectral radiant intensity of the Starbird stages three and four for the plume camera total field of view

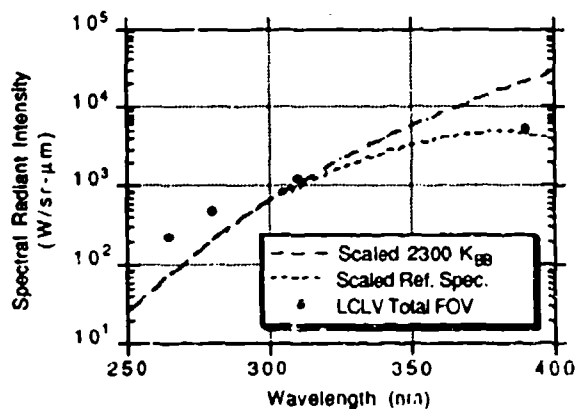


Fig. 75 – Measured spectral radiant intensity of LCLV stage three for the plume camera total field of view

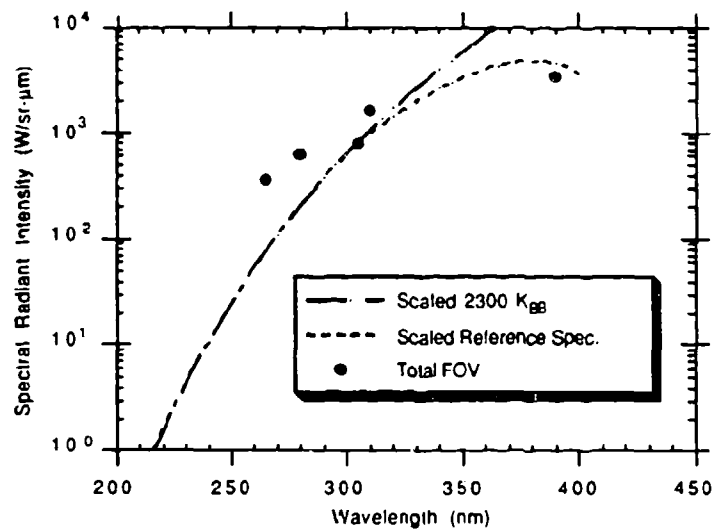


Fig. 76 - Measured spectral radiant intensity of Antares for the plume camera total field of view

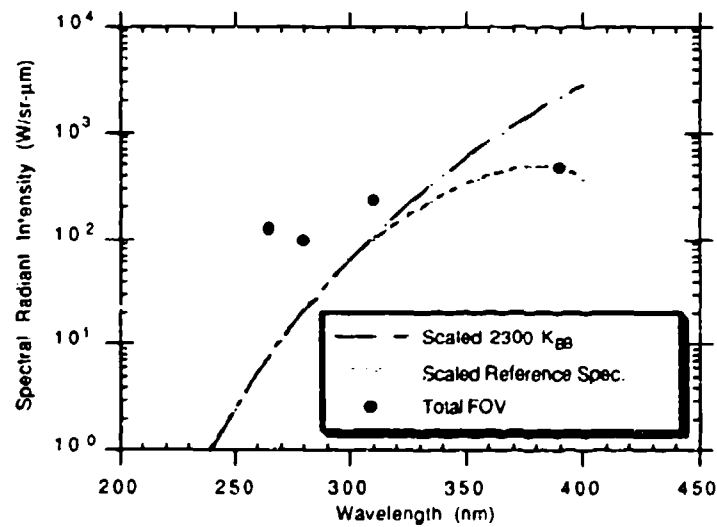


Fig. 77 - Measured spectral radiant intensity of Star 27 for the plume camera total field of view



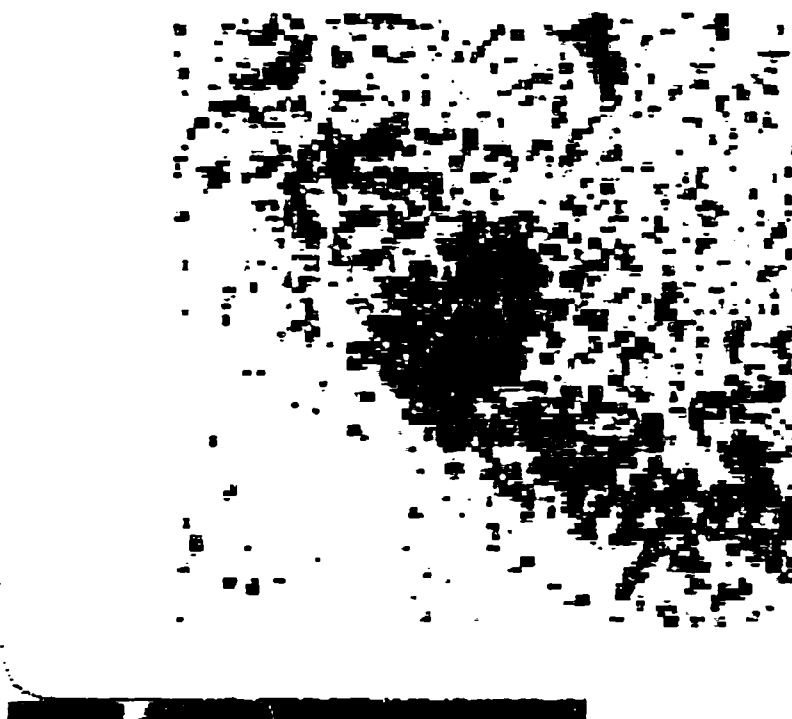


Fig. 78 - A plume-camera composite image using filter PC-1, showing a bright outer region during the Nihka test



Fig. 79 - A plume-camera composite image using filter PC-3, showing an outer region during the Strypi Antares test

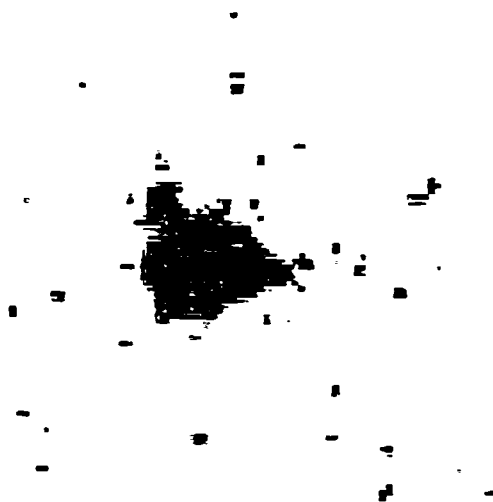


Fig. 80 - A plume-camera composite image using filter PC-3, showing a weak outer region during the LCLV test



Fig. 81 - A plume-camera composite image using filter PC-3, showing no outer region during the Starbird test

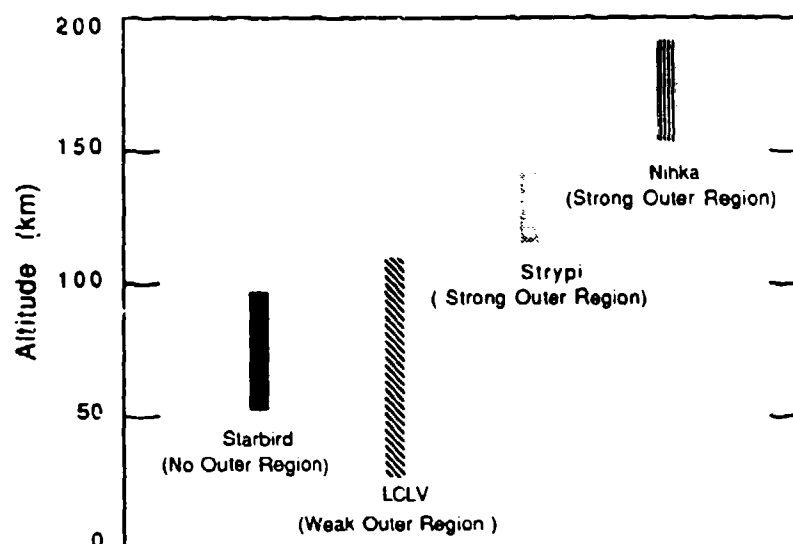


Fig. 82 - Correlation of the presence of outer region with altitude range of rocket during observation

## 10.0 SUMMARY AND CONCLUSIONS

### 10.1 Summary

The goal of the LCLV mission was the acquisition from space of radiometric UV plume data, using the UVPI onboard the LACE satellite. The UVPI plume camera is an imaging radiometer with four filters, centered at 250, 270, 280, and 305 nm (Table 5). This instrument was designed to obtain radiometric data in a spectral region that is especially favorable for missile detection because of the very low solar background. Operation from space is necessary because the atmosphere is practically opaque to wavelengths below 300 nm. From 500-km range, the plume camera has a resolution of approximately 45 m.

The LCLV, a three-stage solid-propellant missile system, was used for this observation. The first stage (a Talos motor) and the second stage (a Sergeant motor) operated at too low an altitude to be observed from space. The mission was designed for the observation of the third-stage plume, which was produced by a powerful Aries rocket motor. The rocket trajectory was selected to permit observation from the LACE satellite during its orbit.

The LCLV was launched from Wallops Island, Virginia, before sunrise on 6 February 1991. The third stage was successfully tracked by the UVPI camera from a range of 500 to 480 km. The third-stage plume was tracked for about 40 s, and plume data were acquired with all four plume-camera filters. The observation intervals are summarized in Tables 12 and 13. The 385 images of the third-stage plume from the plume camera were of sufficient quality and tracking accuracy to permit the superposition of images for increased radiometric accuracy.

The superposed images were analyzed to obtain the spectral radiance, evaluating the plume as a spatially resolved source, and the spectral radiant intensity, summing over space to treat the plume as a point source. The radiometric analysis required a model spectral shape, for which a reference model was taken. Section 3 describes this analysis procedure. The spectral values were also integrated over the nominal filter bandwidths to obtain radiance and radiant intensity values.

The even-numbered Figs. 24 through 30 are false-color maps of the spatial distributions of the time-averaged radiant intensities of the third-stage plumes. Contour plots of the plume radiance were also generated from the superposed images and are presented in the odd-numbered Figs. 25 through 31.

Figure 22 shows the image and Fig. 23 the contour plot of the NRL ground-based UV beacon, which well represents a point source under these conditions. This image indicates the resolution limit of the instrument at 500-km range. The length of the rocket plume, measured in terms of a brightness variation, observed during this mission is less than or comparable to the 45-m resolution limit (Table 27). The consequent smearing of the source over an increased effective area significantly reduces the observed peak radiance of the plumes. The observed radiances are, hence, denoted "apparent" values to distinguish between the observed radiance values and those that would be obtained from an instrument with higher spatial resolution. Adjusting the CHARM 1.4 predicted peak radiances for this effect yields approximately factor-of-four agreement between prediction and observation (Table 28).

Radiant intensity values, obtained by summing over the plume central region and over the plume-camera field of view, are not affected by this resolution effect. The plume central region was defined for these computations as the region in which the radiance exceeded 25% of the peak apparent value, with the addition of the area defined by a 5 by 5 pixel dilation of this region. The projected area of the central region so defined was approximately 5000 to 7600 m<sup>2</sup> (Table 26). The remainder of the plume camera images is denoted the outer region.

The outer region data from the LCLV showed weak radiances and suffered from poor signal-to-noise ratio. This phenomenon may be related to the extreme brightness of the Aries motor plume. The plume brightness caused the camera gain to decrease to where it could no longer detect a radiant far field. However, like the Strypi test at higher altitude, an identifiable shock or mixing layer structure could be found in the LCLV outer region data. Thus, the outer region radiance could be causally connected to the LCLV third stage. The central region and total radiant intensities measured by the plume camera are summarized in Table 31. Figures 17 and 18 show the temporal behavior of the plume central region and total spectral radiant intensities measured by the plume camera.

The UVPI tracker camera provides wideband (255 to 450 nm) data that may complement the plume-camera data. The wide field of view of the tracker camera clearly prevents resolution of the plume, but radiant intensity values can be obtained. A 19 x 19 pixel region of the tracker camera images, matching the total field of view of the plume camera, was taken for computing radiant intensities. The values so obtained are summarized in Table 32, and the spectral radiant intensity time dependence is illustrated in Fig. 19.

The spectral radiant intensities deduced from the UVPI observations can be compared to the reference model of plume emission. The plume central region spectral radiant intensities show reference-like dependencies over the 250 to 300-nm range. The data suggest that the 250 to 270-nm values are higher, relative to the 280 to 300-nm values, than the reference predicts (Fig. 67). The spectral radiant intensities summed over the plume camera field of view show similar ultraviolet excess. The full field values from the plume camera can be complemented by the tracker-camera data over the same area (Fig. 68). The 390-nm value so obtained adds support to the tentative conclusion that the decrease in plume spectral radiant intensity, as the wavelength decreases below 300 nm, is less than expected on the basis of the reference model. This is similar to trends in data seen in the Strypi and other plume data, as shown in Section 9.

The LCLV vehicle carried an Aries solid-fuel motor to power its third stage. The Aries motor performed nominally, causing the rocket to reach a 117-km altitude at burnout. This performance was reflected in the plume radiance measured by the UVPI, which detected and tracked the third

stage. The results suggest that the technique for observing phenomena in the UV is effective in detecting and tracking high-energy upper stages at an early point in their flights.

## 10.2 Achievement of Objectives

The results of the UVPI observation of the LCLV missile can be compared to the objectives listed in Section 1.3.

### 10.2.1 General Objectives

- *Obtain isoradiance contours for the third stage plume.* Spatially resolved images of the third-stage plume were obtained for four data intervals corresponding to the four plume camera filters. These images were scaled to radiance maps and contours (Sections 4 and 5).
- *Obtain radiant intensity measurements based on the entire field of view of the plume camera and on a subregion corresponding approximately to a plume core.* Radiant intensity measurements for the plume camera FOV and for a plume central region defined in Section 5.1 were extracted from the images for the four data intervals (Section 6).
- *Compare radiometric measurements for the third-stage plume with those generated by the CHARM computer codes.* The preliminary comparison undertaken here suggests that the UVPI data present a spectral shape somewhat different from that of the reference spectrum. The experimental results indicate that the emission at wavelengths shorter than 300 nm is greater, relative to the emission at longer wavelengths, than is predicted by the reference model. These results are described in Section 7. The detailed comparison of CHARM predictions to the UVPI observations is a task for the modelers.
- *Provide radiometric measurements for non-plume, transient phenomena, if any.* A persistent cloud trail could be seen in the third stage of the LCLV test. The cloud at one point appeared to extend both before and behind the Aries stage, possibly indicating a case burn-through.

### 10.2.2 Specific Objectives Related to Spatial Features

- *Obtain the length of the third-stage plume core.* The resolution limit of the PSF-corrected UVPI corresponds, at this range, to about 40 m, which is comparable to the expected plume length. Thus, a close measurement of the plume length was not possible, but (as described in Section 5.3) the observations are consistent with the predicted plume length.
- *Determine the shape of the shock boundary/mixing layer for different rocket velocities.* A weak radiance in the outer region and the presence of an apparent shock or mixing layer structure in the images suggests that, like the Stryi and Nihka tests, a UV luminous outer region was formed as a result of the LCLV.
- *Identify asymmetries in plume shape and investigate possible causes.* No plume shape asymmetries were observed. The resolution limit of the UVPI at this range is such that only large asymmetries could have been detected.

### 10.2.3 Specific Objectives Related to Temporal Features

- *Identify temporal trends in radiometrics and investigate possible dependence on rocket velocity.* The time behavior of the radiant intensity of the third-stage plume is described in Section 6. No obvious correlation with rocket velocity was observed.
- *Investigate radiometric fluctuations to determine whether short-term variations in brightness are observed.* The statistics of the variations in plume radiant intensity are described in Section 6. Several peaks beyond the range of statistical likelihood were observed. The data were carefully analyzed and no reason was found to reject them.
- *Identify changes with time in the shape of the plume's outer region.* The weak outer region seen in PC-3 was not seen clearly in PC-1, indicating that it may have faded with time.
- *Identify persistence and cumulative effects, if any, in plumes or nonplume phenomena.* A cloud or trail was observed in the LCLV test. It apparently was an exhaust trail from the Aries late in its burn.

### 10.2.4 Specific Objectives Related to Spectral Features

- *Compare the shape of the plume central region's emission spectrum with the reference spectral shape, which is that of micron-sized alumina particles at their melting point, and spectral shape determinations based on other sensors.* As described in Section 7, the UVPI data indicate that the decrease in spectral radiance and radiant intensity, as the wavelength decreases below 300 nm, is less than indicated by the reference model. This is similar to data from the other tests. A comparison of the UVPI data with spectral data from other tests is discussed in Section 9.
- *Relate tracker-camera measurement to visible and infrared measurements made by other sensors.* The UVPI acquired plume radiometric data to 450-nm wavelength. These radiant intensity values can be compared to data at longer wavelengths from other sensors as those data become available.
- *Characterize the emission spectrum for the plume's outer regions, if any.* A weak identifiable outer region was found in the LCLV test data; emission was apparently strongest in the UV with  $\lambda < 300$  nm.

It is clear from the above that most of the task objectives were achieved. However, the instrumental limitations in resolution, as well as the uncertainty in the reference spectral shape, complicate the extraction of precise values.

### 10.3 Conclusions

The UVPI observation of the LCLV launch again demonstrates the capability of the instrument for tracking and imaging missiles in flight from 500-km range. The bright plume of the Aries third stage was successfully tracked throughout its burn. The Aries was a high-energy upper stage, and the large detected signal level and steady tracking of the Aries by the UVPI indicate that observation in the UV can be used to detect and track solid-fuel boosters above the atmosphere.



The third stage was tracked for approximately 40 s, and 385 plume-camera images, distributed over all four UVPI filters, were collected and analyzed. The spectral radiance and spectral radiant intensities were extracted from these images. Absolute values were necessarily obtained on the basis of an assumed spectral shape, namely the reference spectrum, which is the spectrum of micron-sized alumina particles at their melting point of 2320 K. A comparison of the results for the four UVPI filters indicates that the reference shape is not inaccurate, but the new data indicate a stronger component in the far UV,  $\lambda < 300$  nm, than the model predicts. This result is similar to that obtained in the other tests, as discussed in Section 9.

Like the Nihka and Strypi tests, the images reveal a radiant plume with an identifiable outer region of UV radiance, such as might be associated with a shock or mixing layer produced by the plume. The outer region radiances that are measured are generally weak compared to the plume central region and exhibit only a slight shock-wave structure near the rocket. Weak shock or mixing layer radiance seems to correlate with the intermediate altitude of the LCLV compared to the strong outer regions seen in the Strypi and Nihka tests at high altitude and the absence of an outer region in the Starbird test at lower altitude. This correlation is discussed in Section 9.

The time-dependence of the third-stage plume central region radiant intensity within each filter interval showed no pronounced trends or variations. Momentary, single-frame peaks exceeding the range of normal statistical variation were detected. Whether these can be correlated with missile engine events or other sensors remains to be seen.

The LCLV data gathered by UVPI form a basis for continued analysis and evaluation. Comparison with models and with data from sensors on other platforms and UVPI data from other tests will also yield improved radiometric results and an enhanced phenomenological understanding of UV emission by solid rocket motors in the upper atmosphere.

## REFERENCES

1. H.W. Smathers, D.M. Horan, J.G. Cardon, E.R. Malaret, M.R. Corson, and J.E. Brandenburg, "Ultraviolet Plume Instrument Description and Plume Data Reduction Methodology," NRL Report 9531, 1993.
2. H.W. Smathers, D.M. Horan, J.G. Cardon, E.R. Malaret, M. Singh, T. Sorensen, P.M. Laufer, M.R. Corson, J.E. Brandenburg, J.A. McKay, and R.R. Strunce, Jr., "UVPI Imaging From the LACE Satellite: The Strypi Rocket Plume," NRL Report 9526, 1993.
3. J.T. Wright, "Ultraviolet Plume Instrument (UVPI) Subsystem Users Manual," SDRL 068, Loral EOS Document No. 3731, Loral Electro Optical Systems, Pasadena, California, January 1989.
4. H.W. Smathers, D.M. Horan, L.H. Reynolds, W. Ramsey and H.D. Wolpert, "Design and Description of the Ultraviolet Plume Instrument (UVPI)," *Proc. SPIE* **1158**, 196, August 1989.
5. H.W. Smathers, G.R. Carruthers, W. Ramsey, G. Steiner and W. Louissaint, "Calibration and Performance of the Ultraviolet Plume Instrument (UVPI)," *Proc. SPIE* **1158**, 212, August 1989.
6. J. Nicholas, "Experiment Requirements Document for UVPI Observations of SDIO Special Projects (SPFE) Launches Rev 3," The Analytic Sciences Corporation, Arlington, Virginia, August 1990.
7. W.A. Jeffrey, M. Slack, and L. Laux, "Orbus Preflight Predictions," IDA document D-755, Institute for Defense Analyses, April 1990.

8. J.A. Marqusee, "The State of Knowledge of UV/V Boost- and Post-Boost-Phase Phenomenology and a Preliminary Assessment of Its Utility to SDI," IDA Paper P-2232, Institute for Defense Analyses, July 1989.
9. R.A. Reed and V.S. Calia, "Review of Rocket Particle Properties Research," Final Report AEDC-TR-89-11, Arnold Engineering Development Center, Tullahoma, Tennessee, November 1989.
10. K. Fukunaga, *Introduction to Statistical Pattern Recognition* (Academic Press, 1972).
11. C.L. Wyatt, *Radiometric System Design* (MacMillan, New York, 1987).
12. F.E. Nicodemus, "Normalization in Radiometry," *Applied Optics* **12**(12), 2960-2973 (1973).
13. J.A. Marqusee, Institute for Defense Analyses, private communication, 14 March 1991.
14. P.W. Erdman, E. Zipf, P. Espy, C. Howlett, D.A. Levin, and G.V. Candler, "In-Situ Measurements of UV and VUV Radiation from a Rocket Plume and Re-entry Bow Shock," AIAA Paper No. 92-0124, American Institute of Aeronautics and Astronautics, January 1992.
15. A. Papoulis, *Probability, Random Variables, and Stochastic Processes*, 2nd ed., (McGraw Hill, 1984).
16. W.L. Wolfe and G.J. Zissis, editors *The Infrared Handbook*, (Environmental Research Institute of Michigan, 1978).
17. R.H. Kingston, *Detection of Optical and Infrared Radiation* (Springer-Verlag, New York, 1978) pp. 43-51.
18. W.A. Jeffrey, Grumman Corporation, private communication, August 1992.
19. H.W. Smathers, D.M. Horan, J.G. Cardon, E.R. Malaret, J.E. Brandenburg, R. Campion, and R.R. Strunce, Jr., "UVPI Imaging From The LACE Satellite: The Nihka Rocket Plume," NRL Report 9537, 1993.
20. H.W. Smathers, D.M. Horan, J.G. Cardon, E.R. Malaret, L.Perez, T.Tran, J.E. Brandenburg, and R.R. Strunce, Jr., "UVPI Imaging From The LACE Satellite: The Starbird Rocket Plume," NRL Report 9546, 1993.

## Appendix A

### LCLV TRAJECTORY PARAMETERS

Various LCLV trajectory-related parameters are given as a function of time. The first column in each table is TALO (time after liftoff,) in seconds. Table A1 shows the rocket's position in Earth center-fixed (ECF) coordinates and the rocket's speed. Table A2 shows the aspect angle, the angle of attack, and the distance between the satellite and the rocket. The aspect angle is defined as the angle between the line-of-sight (LOS) vector from the satellite to the target point and the longitudinal axis of the rocket. The angle of attack is defined as the angle between the longitudinal axis of the rocket and its velocity vector. Table A3 shows the rocket's altitude, geodetic latitude, and longitude.

Table A1 – Rocket Position and Speed in ECF Coordinates

TALO (s)	XPOS (km)	YPOS (km)	ZPOS (km)	SPEED (km/s)
3	1264.992	-4881.588	3892.326	0.149
4	1265.048	-4881.700	3892.408	0.207
5	1265.119	-4881.868	3892.506	0.253
6	1265.191	-4882.075	3892.633	0.270
7	1265.274	-4882.292	3892.770	0.261
8	1265.357	-4882.506	3892.892	0.247
9	1265.428	-4882.708	3893.015	0.238
10	1265.506	-4882.905	3893.123	0.223
11	1265.572	-4883.089	3893.231	0.220
12	1265.645	-4883.268	3893.338	0.234
13	1265.723	-4883.462	3893.443	0.258
14	1265.815	-4883.677	3893.552	0.280
15	1265.913	-4883.914	3893.665	0.300
16	1266.015	-4884.167	3893.791	0.321
17	1266.122	-4884.440	3893.919	0.342
18	1266.252	-4884.729	3894.049	0.356
19	1266.376	-4885.032	3894.189	0.374
20	1266.512	-4885.346	3894.339	0.392
21	1266.653	-4885.679	3894.490	0.408
22	1266.797	-4886.025	3894.652	0.424
23	1266.952	-4886.376	3894.833	0.446
24	1267.112	-4886.749	3895.018	0.463
25	1267.268	-4887.139	3895.215	0.484
26	1267.434	-4887.537	3895.434	0.505
27	1267.597	-4887.954	3895.667	0.526
28	1267.763	-4888.382	3895.923	0.550
29	1267.934	-4888.830	3896.194	0.577
30	1268.110	-4889.298	3896.482	0.603
31	1268.290	-4889.781	3896.795	0.635
32	1268.478	-4890.294	3897.119	0.665
33	1268.670	-4890.824	3897.471	0.700
34	1268.879	-4891.385	3897.835	0.733

Table A1 – Rocket Position and Speed in ECF Coordinates (Cont'd)

TALO (s)	XPOS (km)	YPOS (km)	ZPOS (km)	SPEED (km/s)
35	1269.101	-4891.962	3898.227	0.756
36	1269.320	-4892.560	3898.635	0.756
37	1269.531	-4893.161	3899.043	0.756
38	1269.750	-4893.759	3899.450	0.759
39	1269.976	-4894.351	3899.869	0.754
40	1270.202	-4894.938	3900.284	0.739
41	1270.416	-4895.517	3900.690	0.731
42	1270.621	-4896.098	3901.082	0.720
43	1270.832	-4896.662	3901.477	0.710
44	1271.040	-4897.219	3901.866	0.699
45	1271.246	-4897.767	3902.247	0.688
46	1271.450	-4898.306	3902.622	0.675
47	1271.651	-4898.835	3902.988	0.664
48	1271.850	-4899.356	3903.348	0.650
49	1272.038	-4899.869	3903.700	0.641
50	1272.233	-4900.373	3904.045	0.628
51	1272.423	-4900.860	3904.393	0.618
52	1272.613	-4901.346	3904.724	0.607
53	1272.793	-4901.826	3905.049	0.595
54	1272.977	-4902.288	3905.376	0.585
55	1273.160	-4902.749	3905.687	0.574
56	1273.342	-4903.200	3905.991	0.563
57	1273.512	-4903.647	3906.289	0.552
58	1273.688	-4904.075	3906.589	0.544
59	1273.863	-4904.503	3906.875	0.531
60	1274.027	-4904.925	3907.153	0.522
61	1274.197	-4905.331	3907.434	0.513
62	1274.366	-4905.736	3907.700	0.502
63	1274.531	-4906.126	3907.970	0.492
64	1274.687	-4906.517	3908.223	0.482
65	1274.849	-4906.892	3908.480	0.472
66	1275.010	-4907.265	3908.721	0.464
67	1275.169	-4907.631	3908.956	0.450
68	1275.316	-4907.984	3909.194	0.443
69	1275.471	-4908.335	3909.417	0.432
70	1275.622	-4908.671	3909.643	0.433
71	1275.775	-4909.014	3909.859	0.445
72	1275.931	-4909.366	3910.083	0.464
73	1276.090	-4909.732	3910.319	0.483
74	1276.261	-4910.110	3910.565	0.506
75	1276.447	-4910.508	3910.816	0.526
76	1276.627	-4910.919	3911.089	0.555
77	1276.825	-4911.362	3911.361	0.577
78	1277.023	-4911.810	3911.666	0.605
79	1277.238	-4912.282	3911.978	0.635
80	1277.451	-4912.787	3912.299	0.661

Table A1 - Rocket Position and Speed in ECF Coordinates (Cont'd)

TALO (s)	XPOS (km)	YPOS (km)	ZPOS (km)	SPEED (km/s)
81	1277.669	-4913.305	3912.646	0.690
82	1277.892	-4913.846	3913.011	0.718
83	1278.129	-4914.406	3913.393	0.743
84	1278.371	-4914.985	3913.790	0.767
85	1278.611	-4915.591	3914.193	0.789
86	1278.863	-4916.206	3914.619	0.813
87	1279.120	-4916.845	3915.050	0.835
88	1279.383	-4917.502	3915.495	0.859
89	1279.648	-4918.170	3915.964	0.886
90	1279.929	-4918.863	3916.440	0.912
91	1280.209	-4919.585	3916.923	0.940
92	1280.501	-4920.319	3917.433	0.970
93	1280.801	-4921.083	3917.951	0.999
94	1281.104	-4921.862	3918.497	1.031
95	1281.416	-4922.673	3919.053	1.065
96	1281.735	-4923.509	3919.629	1.100
97	1282.062	-4924.379	3920.219	1.138
98	1282.406	-4925.274	3920.830	1.174
99	1282.756	-4926.198	3921.465	1.216
100	1283.115	-4927.154	3922.125	1.256
101	1283.491	-4928.139	3922.809	1.297
102	1283.868	-4929.163	3923.510	1.341
103	1284.262	-4930.218	3924.237	1.386
104	1284.667	-4931.314	3924.982	1.430
105	1285.090	-4932.441	3925.754	1.476
106	1285.513	-4933.606	3926.555	1.524
107	1285.954	-4934.805	3927.385	1.571
108	1286.406	-4936.047	3928.235	1.620
109	1286.877	-4937.323	3929.114	1.666
110	1287.350	-4938.644	3930.012	1.714
111	1287.841	-4939.999	3930.940	1.761
112	1288.351	-4941.387	3931.896	1.812
113	1288.863	-4942.823	3932.875	1.862
114	1289.395	-4944.295	3933.884	1.914
115	1289.936	-4945.807	3934.924	1.968
116	1290.499	-4947.364	3935.989	2.022
117	1291.065	-4948.965	3937.086	2.080
118	1291.660	-4950.611	3938.210	2.138
119	1292.257	-4952.299	3939.378	2.200
120	1292.879	-4954.044	3940.565	2.263
121	1293.513	-4955.836	3941.792	2.327
122	1294.169	-4957.676	3943.057	2.399
123	1294.841	-4959.578	3944.356	2.463
124	1295.534	-4961.525	3945.695	2.516
125	1296.230	-4963.516	3947.067	2.568
126	1296.955	-4965.547	3948.460	2.606

Table A1 – Rocket Position and Speed in ECF Coordinates (Cont'd)

TALO (s)	XPOS (km)	YPOS (km)	ZPOS (km)	SPEED (km/s)
127	1297.679	-4967.611	3949.877	2.640
128	1298.421	-4969.705	3951.304	2.651
129	1299.154	-4971.803	3952.749	2.655
130	1299.899	-4973.908	3954.186	2.647
131	1300.641	-4976.001	3955.627	2.638
132	1301.372	-4978.089	3957.063	2.631

Table A2 – Rocket Aspect Angle, Attack Angle, and Range from Satellite

TALO (s)	Aspect Angle (deg)	Attack Angle (deg)	Target Range (km)
3	59.84	4.09	820.989
4	59.75	2.35	815.663
5	58.11	1.86	810.325
6	57.21	1.28	804.975
7	56.85	1.43	799.647
8	56.76	1.45	794.348
9	56.59	1.81	789.076
10	56.45	1.38	783.843
11	56.55	0.86	778.639
12	56.66	0.77	773.471
13	56.55	1.32	768.321
14	56.39	0.99	763.192
15	56.32	0.68	758.076
16	56.27	0.92	752.977
17	56.23	1.71	747.894
18	56.17	0.61	742.842
19	56.07	0.67	737.803
20	55.84	0.40	732.79
21	55.45	0.48	727.796
22	55.01	1.64	722.823
23	54.5	0.28	717.877
24	53.78	0.83	712.949
25	52.91	0.95	708.035
26	52.04	0.54	703.146
27	51.18	0.87	698.27
28	50.35	0.41	693.412
29	49.63	0.07	688.572
30	49.03	0.88	683.748
31	48.53	0.41	678.941
32	48.12	0.74	674.148
33	47.74	0.37	669.369
34	47.35	0.72	664.609
35	46.88	0.42	659.869
36	46.1	0.59	655.144
37	45.54	0.29	650.451
38	45.48	0.69	645.806

Table A2 – Rocket Aspect Angle, Attack Angle, and Range from Satellite (Cont'd)

TALO (s)	Aspect Angle (deg)	Attack Angle (deg)	Target Range (km)
39	45.43	0.21	641.204
40	44.92	0.27	636.649
41	44.21	0.95	632.142
42	43.81	0.19	627.681
43	43.48	0.13	623.278
44	43.16	0.11	618.93
45	42.79	0.14	614.638
46	42.41	0.22	610.403
47	42.02	0.25	606.229
48	41.64	0.55	602.115
49	41.25	0.33	598.057
50	40.88	0.91	594.067
51	40.58	0.42	590.14
52	40.29	0.78	586.279
53	39.93	0.66	582.479
54	39.53	0.53	578.751
55	39.16	0.50	575.093
56	38.8	0.68	571.504
57	38.43	0.83	567.982
58	38.09	0.56	564.537
59	37.76	0.74	561.165
60	37.44	0.76	557.865
61	37.16	0.68	554.643
62	36.86	0.75	551.5
63	36.57	0.96	548.435
64	36.28	0.70	545.447
65	36	0.75	542.543
66	35.71	0.74	539.724
67	35.43	1.05	536.987
68	35.16	0.83	534.332
69	34.9	0.72	531.768
70	34.59	0.75	529.29
71	34.31	0.34	526.894
72	34.04	0.54	524.567
73	33.69	0.30	522.306
74	33.33	0.91	520.114
75	32.88	1.13	517.99
76	32.35	1.09	515.926
77	31.72	1.29	513.93
78	30.93	0.53	511.993
79	30.22	0.83	510.123
80	29.49	0.40	508.312
81	28.82	0.48	506.562
82	28.22	0.38	504.875
83	27.67	0.38	503.254
84	27.19	0.67	501.701

Table A2 – Rocket Aspect Angle, Attack Angle, and Range from Satellite (Cont'd)

TALO (s)	Aspect Angle (deg)	Attack Angle (deg)	Target Range (km)
85	26.75	0.50	500.217
86	26.34	0.25	498.804
87	25.96	0.21	497.465
88	25.63	0.67	496.199
89	25.35	0.32	495.002
90	25.1	0.64	493.88
91	24.89	0.31	492.83
92	24.71	0.28	491.85
93	24.56	0.51	490.941
94	24.43	0.12	490.059
95	24.33	0.24	489.33
96	24.29	0.42	488.627
97	24.3	0.17	487.994
98	24.33	0.03	487.427
99	24.42	0.20	486.926
100	24.54	0.35	486.486
101	24.68	0.26	486.11
102	24.85	0.10	485.802
103	25.05	0.24	485.555
104	25.31	0.21	485.373
105	25.59	0.26	485.253
106	25.87	0.18	485.193
107	26.22	0.12	485.193
108	26.63	0.17	485.257
109	27.03	0.30	485.382
110	27.44	0.05	485.574
111	27.87	0.21	485.826
112	28.36	0.21	486.141
113	28.85	0.02	486.52
114	29.36	0.13	486.96
115	29.89	0.14	487.459
116	30.45	0.22	488.02
117	31.01	0.23	488.642
118	31.58	0.33	489.323
119	32.18	0.16	490.056
120	32.79	0.08	490.851
121	33.4	0.10	491.701
122	34.05	0.06	492.601
123	34.7	0.12	493.555
124	35.33	0.21	494.561
125	35.98	0.17	495.635
126	36.65	0.11	496.776
127	37.38	0.15	497.997
128	38.07	0.16	499.304
129	38.76	0.16	500.706
130	39.43	0.12	502.217



Table A2 - Rocket Aspect Angle, Attack Angle, and Range from Satellite (Cont'd)

TALO (s)	Aspect Angle (deg)	Attack Angle (deg)	Target Range (km)
131	40.14	0.15	503.837
132	40.85	0.19	505.572

Table A3 -- Rocket Altitude, Geodetic Latitude, and Longitude

TALO (s)	ALTITUDE (km)	LONGITUDE (deg)	LATITUDE (deg)
3	0.141	284.528	37.849
4	0.288	284.528	37.849
5	0.491	284.528	37.849
6	0.741	284.529	37.849
7	1.007	284.529	37.848
8	1.263	284.529	37.848
9	1.507	284.529	37.848
10	1.739	284.530	37.847
11	1.959	284.530	37.847
12	2.175	284.530	37.847
13	2.404	284.531	37.846
14	2.654	284.531	37.846
15	2.924	284.531	37.845
16	3.214	284.532	37.844
17	3.523	284.532	37.844
18	3.849	284.533	37.843
19	4.191	284.533	37.842
20	4.550	284.534	37.841
21	4.925	284.534	37.840
22	5.317	284.535	37.840
23	5.728	284.536	37.839
24	6.158	284.536	37.838
25	6.608	284.537	37.837
26	7.080	284.538	37.836
27	7.574	284.538	37.835
28	8.091	284.539	37.835
29	8.633	284.540	37.834
30	9.203	284.540	37.833
31	9.800	284.541	37.833
32	10.428	284.541	37.832
33	11.087	284.542	37.831
34	11.780	284.543	37.831
35	12.507	284.543	37.830
36	13.257	284.544	37.829
37	14.008	284.545	37.829
38	14.759	284.545	37.828
39	15.513	284.546	37.828
40	16.262	284.547	37.827
41	16.995	284.548	37.827
42	17.721	284.548	37.826

Table A3 – Rocket Altitude, Geodetic Latitude, and Longitude (Cont'd)

TALO (s)	ALTITUDE (km)	LONGITUDE (deg)	LATITUDE (deg)
43	18.436	284.549	37.826
44	19.141	284.550	37.825
45	19.835	284.550	37.825
46	20.517	284.551	37.824
47	21.187	284.552	37.824
48	21.845	284.553	37.823
49	22.491	284.553	37.823
50	23.126	284.554	37.822
51	23.750	284.555	37.822
52	24.363	284.555	37.821
53	24.964	284.556	37.821
54	25.555	284.557	37.820
55	26.133	284.557	37.820
56	26.702	284.558	37.819
57	27.259	284.559	37.819
58	27.806	284.559	37.818
59	28.343	284.560	37.818
60	28.869	284.561	37.817
61	29.385	284.561	37.817
62	29.892	284.562	37.817
63	30.388	284.563	37.816
64	30.873	284.563	37.816
65	31.349	284.564	37.815
66	31.814	284.565	37.815
67	32.271	284.565	37.814
68	32.715	284.566	37.814
69	33.151	284.567	37.813
70	33.576	284.567	37.813
71	34.001	284.568	37.812
72	34.439	284.569	37.812
73	34.895	284.569	37.811
74	35.369	284.570	37.811
75	35.864	284.571	37.810
76	36.382	284.572	37.810
77	36.926	284.573	37.809
78	37.495	284.574	37.809
79	38.090	284.575	37.808
80	38.716	284.576	37.807
81	39.368	284.577	37.807
82	40.050	284.577	37.806
83	40.758	284.578	37.806
84	41.493	284.579	37.805
85	42.251	284.580	37.804
86	43.033	284.581	37.804
87	43.837	284.582	37.803
88	44.664	284.583	37.802

Table A3 - Rocket Altitude, Geodetic Latitude, and Longitude (Cont'd)

TALO (s)	ALTITUDE (km)	LONGITUDE (deg)	LATITUDE (deg)
89	45.515	284.584	37.802
90	46.392	284.585	37.801
91	47.296	284.586	37.800
92	48.228	284.588	37.799
93	49.189	284.589	37.799
94	50.180	284.590	37.798
95	51.203	284.591	37.797
96	52.260	284.592	37.796
97	53.351	284.593	37.795
98	54.479	284.594	37.795
99	55.644	284.595	37.794
100	56.851	284.597	37.793
101	58.098	284.598	37.792
102	59.386	284.599	37.791
103	60.717	284.600	37.790
104	62.092	284.602	37.789
105	63.512	284.603	37.788
106	64.978	284.604	37.787
107	66.491	284.606	37.785
108	68.051	284.607	37.784
109	69.660	284.609	37.783
110	71.314	284.610	37.782
111	73.017	284.612	37.780
112	74.766	284.613	37.779
113	76.566	284.615	37.778
114	78.416	284.616	37.776
115	80.318	284.618	37.775
116	82.273	284.620	37.773
117	84.283	284.621	37.772
118	86.349	284.623	37.770
119	88.474	284.625	37.769
120	90.660	284.627	37.767
121	92.909	284.628	37.765
122	95.223	284.630	37.764
123	97.607	284.632	37.762
124	100.055	284.634	37.760
125	102.556	284.636	37.758
126	105.108	284.638	37.756
127	107.700	284.640	37.755
128	110.323	284.642	37.753
129	112.960	284.644	37.751
130	115.599	284.646	37.749
131	118.230	284.648	37.747
132	120.852	284.650	37.745

## Appendix B

### UVPI PARAMETERS

Table B1 is a list of all frames used for this report for the four data intervals. The time, in UVPI mission time (UMT), and frame number are recorded in the first two columns. Note that the frame number carries a trailing P if it is a plume-camera frame and a trailing T if it is a tracker-camera frame. The third column lists the filter wheel position if it is a plume-camera frame. A filter-wheel position of 0 denotes a tracker-camera frame. The next two columns provide the exposure time for the frame. For the plume camera this is fixed at 1/30th of a second, but for the tracker camera it is variable, with a maximum allowed value of 1/30th of a second. The next two columns provide the tracker-camera and the plume-camera gain steps. For the 30 Hz zoom image transmission rate, each telemetry frame carries one image. For the 5 Hz normal image transmission rate, six telemetry frames carry one image. UVPI mission time is related to GMT for the LCLV data intervals by the equation:

$$\text{UMT} = \text{GMT} + [0.27 + (\text{Frame}) (7.8 \times 10^{-6})] \text{ seconds.}$$

Table B1 – Telemetry Frames and Camera Parameters

UMT	Telemetry Frame	Filter	Tracker Exp. Time (ms)	Plume Exp. Time (ms)	Tracker Gain	Plume Gain	Comments
7:30:42.21	15645T	0	12.2	33.3	6	9	Begin data
7:30:42.25	15646T	0	12.2	33.3	6	9	interval 1
7:30:42.28	15647P	4	12.2	33.3	6	9	PC-4
7:30:42.31	15648P	4	12.2	33.3	6	9	
7:30:42.35	15649P	4	12.2	33.3	6	9	
7:30:42.38	15650P	4	12.2	33.3	6	9	
7:30:42.41	15651P	4	12.2	33.3	6	9	
7:30:42.45	15652P	4	12.2	33.3	6	9	
7:30:42.48	15653P	4	12.2	33.3	6	9	
7:30:42.51	15654P	4	12.2	33.3	6	9	
7:30:42.55	15655T	0	12.2	33.3	6	9	
7:30:42.58	15656T	0	12.2	33.3	6	9	
7:30:42.61	15657P	4	12.2	33.3	6	9	
7:30:42.65	15658P	4	12.2	33.3	6	9	
7:30:42.68	15659P	4	12.2	33.3	6	9	
7:30:42.71	15660P	4	12.2	33.3	6	9	
7:30:42.75	15661P	4	12.2	33.3	6	9	
7:30:42.78	15662P	4	12.2	33.3	6	9	
7:30:42.81	15663P	4	12.2	33.3	6	9	
7:30:42.85	15664P	4	12.2	33.3	6	9	
7:30:42.88	15665T	0	12.2	33.3	6	9	
7:30:42.91	15666T	0	12.2	33.3	6	9	
7:30:42.95	15667P	4	12.2	33.3	6	9	
7:30:42.98	15668P	4	12.2	33.3	6	9	
7:30:43.01	15669P	4	12.2	33.3	6	9	
7:30:43.05	15670P	4	12.2	33.3	6	9	
7:30:43.08	15671P	4	12.2	33.3	6	9	
7:30:43.11	15672P	4	12.2	33.3	6	9	
7:30:43.15	15673P	4	12.2	33.3	6	9	
7:30:43.18	15674P	4	12.2	33.3	6	9	
7:30:43.21	15675T	0	12.2	33.3	6	9	

Table B1 - Telemetry Frames and Camera Parameters (Cont'd)

UMT	Telemetry Frame	Filter	Tracker Exp. Time (ms)	Plume Exp. Time (ms)	Tracker Gain	Plume Gain	Comments
7:30:43.25	15676T	0	12.2	33.3	6	9	
7:30:43.28	15677P	4	12.2	33.3	6	9	
7:30:43.32	15678P	4	12.2	33.3	6	9	
7:30:43.35	15679P	4	12.2	33.3	6	9	
7:30:43.38	15680P	4	12.2	33.3	6	9	
7:30:43.42	15681P	4	12.2	33.3	6	9	
7:30:43.45	15682P	4	12.2	33.3	6	9	
7:30:43.48	15683P	4	12.2	33.3	6	9	
7:30:43.52	15684P	4	12.2	33.3	6	9	
7:30:43.55	15685T	0	12.2	33.3	6	9	
7:30:43.58	15686T	0	12.2	33.3	6	9	
7:30:43.62	15687P	4	12.2	33.3	6	9	
7:30:43.65	15688P	4	12.2	33.3	6	9	
7:30:43.68	15689P	4	12.2	33.3	6	9	
7:30:43.72	15690P	4	12.2	33.3	6	9	
7:30:43.75	15691P	4	12.2	33.3	6	9	
7:30:43.78	15692P	4	12.2	33.3	6	9	
7:30:43.82	15693P	4	12.2	33.3	6	9	
7:30:43.85	15694P	4	12.2	33.3	6	9	
7:30:43.88	15695T	0	12.2	33.3	6	9	
7:30:43.92	15696T	0	12.2	33.3	6	9	
7:30:43.95	15697P	4	12.2	33.3	6	9	
7:30:43.98	15698P	4	12.2	33.3	6	9	
7:30:44.02	15699P	4	12.2	33.3	6	9	
7:30:44.05	15700P	4	12.2	33.3	6	9	
7:30:44.08	15701P	4	12.2	33.3	6	9	
7:30:44.12	15702P	4	12.2	33.3	6	9	
7:30:44.15	15703P	4	12.2	33.3	6	9	
7:30:44.18	15704P	4	12.2	33.3	6	9	
7:30:44.22	15705T	0	12.2	33.3	6	9	
7:30:44.25	15706T	0	12.2	33.3	6	9	
7:30:44.28	15707P	4	12.2	33.3	6	9	
7:30:44.32	15708P	4	12.2	33.3	6	9	
7:30:44.35	15709P	4	12.2	33.3	6	9	
7:30:44.38	15710P	4	12.2	33.3	6	9	
7:30:44.42	15711P	4	12.2	33.3	6	9	
7:30:44.45	15712P	4	12.2	33.3	6	9	
7:30:44.48	15713P	4	12.2	33.3	6	9	
7:30:44.52	15714P	4	12.2	33.3	6	9	
7:30:44.55	15715T	0	12.2	33.3	6	9	
7:30:44.58	15716T	0	12.2	33.3	6	9	
7:30:44.62	15717P	4	12.2	33.3	6	9	
7:30:44.65	15718P	4	12.2	33.3	6	9	
7:30:44.68	15719P	4	12.2	33.3	6	9	
7:30:44.72	15720P	4	12.2	33.3	6	9	
7:30:44.75	15721P	4	12.2	33.3	6	9	
7:30:44.78	15722P	4	12.2	33.3	6	9	
7:30:44.82	15723P	4	12.2	33.3	6	9	
7:30:44.85	15724P	4	12.2	33.3	6	9	
7:30:44.88	15725T	0	12.2	33.3	6	9	
7:30:44.92	15726T	0	12.2	33.3	6	9	
7:30:44.95	15727P	4	12.2	33.3	6	9	
7:30:44.98	15728P	4	12.2	33.3	6	9	
7:30:45.02	15729P	4	12.2	33.3	6	9	
7:30:45.05	15730P	4	12.2	33.3	6	9	

Table B1 - Telemetry Frames and Camera Parameters (Cont'd)

UMT	Telemetry Frame	Filter	Tracker Exp. Time (ms)	Plume Exp. Time (ms)	Tracker Gain	Plume Gain	Comments
7 30:45.08	15731P	4	12.2	33.3	6	9	
7 30:45.12	15732P	4	12.2	33.3	6	9	
7 30:45.15	15733P	4	12.2	33.3	6	9	
7 30:45.18	15734P	4	12.2	33.3	6	9	
7 30:45.22	15735T	0	12.2	33.3	6	9	
7 30:45.25	15736T	0	12.2	33.3	6	9	
7 30:45.28	15737P	4	12.2	33.3	6	9	
7 30:45.32	15738P	4	12.2	33.3	6	9	
7 30:45.35	15739P	4	12.2	33.3	6	9	
7 30:45.38	15740P	4	12.2	33.3	6	9	
7 30:45.42	15741P	4	12.2	33.3	6	9	
7 30:45.45	15742P	4	12.2	33.3	6	9	
7 30:45.48	15743P	4	12.2	33.3	6	9	
7 30:45.52	15744P	4	12.2	33.3	6	9	
7 30:45.55	15745T	0	12.2	33.3	6	9	
7 30:45.58	15746T	0	12.2	33.3	6	9	
7 30:45.62	15747P	4	12.2	33.3	6	9	
7 30:45.65	15748P	4	12.2	33.3	6	9	
7 30:45.68	15749P	4	12.2	33.3	6	9	
7 30:45.72	15750P	4	12.2	33.3	6	9	
7 30:45.75	15751P	4	12.2	33.3	6	9	
7 30:45.78	15752P	4	12.2	33.3	6	9	
7 30:45.82	15753P	4	12.2	33.3	6	9	
7 30:45.85	15754P	4	12.2	33.3	6	9	
7 30:45.88	15755T	0	12.2	33.3	6	9	
7 30:45.92	15756T	0	12.2	33.3	6	9	
7 30:45.95	15757P	4	12.2	33.3	6	9	
7 30:45.98	15758P	4	12.2	33.3	6	9	
7 30:46.02	15759P	4	12.2	33.3	6	9	
7 30:46.05	15760P	4	12.2	33.3	6	9	
7 30:46.08	15761P	4	12.2	33.3	6	9	
7 30:46.12	15762P	4	12.2	33.3	6	9	
7 30:46.15	15763P	4	12.2	33.3	6	9	
7 30:46.19	15764P	4	12.2	33.3	6	9	
7 30:46.22	15765T	0	12.2	33.3	6	9	
7 30:46.25	15766T	0	12.2	33.3	6	9	
7 30:46.29	15767P	4	12.2	33.3	6	9	
7 30:46.32	15768P	4	12.2	33.3	6	9	
7 30:46.35	15769P	4	12.2	33.3	6	9	
7 30:46.39	15770P	4	12.2	33.3	6	9	
7 30:46.42	15771P	4	12.2	33.3	6	9	
7 30:46.45	15772P	4	12.2	33.3	6	9	
7 30:46.49	15773P	4	12.2	33.3	6	9	
7 30:46.52	15774P	4	12.2	33.3	6	9	
7 30:46.55	15775T	0	12.2	33.3	6	9	
7 30:46.59	15776T	0	12.2	33.3	6	9	
7 30:46.62	15777P	4	12.2	33.3	6	9	
7 30:46.65	15778P	4	12.2	33.3	6	9	
7 30:46.69	15779P	4	12.2	33.3	6	9	
7 30:46.72	15780P	4	12.2	33.3	6	9	
7 30:46.75	15781P	4	12.2	33.3	6	9	
7 30:46.79	15782P	4	12.2	33.3	6	9	
7 30:46.82	15783P	4	12.2	33.3	6	9	
7 30:46.85	15784P	4	12.2	33.3	6	9	
7 30:46.89	15785T	0	12.2	33.3	6	9	

Table B1 – Telemetry Frames and Camera Parameters (Cont'd)

UMT	Telemetry Frame	Filter	Tracker Exp. Time (ms)	Plume Exp. Time (ms)	Tracker Gain	Plume Gain	Comments
7:30:46.92	15786T	0	12.2	33.3	6	9	
7:30:46.95	15787P	4	12.2	33.3	6	9	
7:30:46.99	15788P	4	12.2	33.3	6	9	
7:30:47.02	15789P	4	12.2	33.3	6	9	
7:30:47.05	15790P	4	12.2	33.3	6	9	
7:30:47.09	15791P	4	12.2	33.3	6	9	
7:30:47.12	15792P	4	12.2	33.3	6	9	
7:30:47.15	15793P	4	12.2	33.3	6	9	
7:30:47.19	15794P	4	12.2	33.3	6	9	
7:30:47.22	15795T	0	12.2	33.3	6	9	
7:30:47.25	15796T	0	12.2	33.3	6	9	
7:30:47.29	15797P	4	12.2	33.3	6	9	
7:30:47.32	15798P	4	12.2	33.3	6	9	
7:30:47.35	15799P	4	12.2	33.3	6	9	
7:30:47.39	15800P	4	12.2	33.3	6	9	
7:30:47.42	15801P	4	12.2	33.3	6	9	
7:30:47.45	15802P	4	12.2	33.3	6	9	
7:30:47.49	15803P	4	12.2	33.3	6	9	
7:30:47.52	15804P	4	12.2	33.3	6	9	
7:30:47.55	15805T	0	12.2	33.3	6	9	
7:30:47.59	15806T	0	12.2	33.3	6	9	
7:30:47.62	15807P	4	12.2	33.3	6	9	
7:30:47.65	15808P	4	12.2	33.3	6	9	
7:30:47.69	15809P	4	12.2	33.3	6	9	
7:30:47.72	15810P	4	12.2	33.3	6	9	
7:30:47.75	15811P	4	12.2	33.3	6	9	
7:30:47.79	15812P	4	12.2	33.3	6	9	
7:30:47.82	15813P	4	12.2	33.3	6	9	
7:30:47.85	15814P	4	12.2	33.3	6	9	
7:30:47.89	15815T	0	12.2	33.3	6	9	
7:30:47.92	15816T	0	12.2	33.3	6	9	
7:30:47.95	15817P	4	12.2	33.3	6	9	
7:30:47.99	15818P	4	12.2	33.3	6	9	
7:30:48.02	15819P	4	12.2	33.3	6	9	End data
7:30:48.05	15820P	4	12.2	33.3	6	9	interval 1
7:30:54.89	16025T	0	12.2	33.3	6	13	Begin data
7:30:54.93	16026T	0	12.2	33.3	6	13	interval 2
7:30:54.96	16027P	3	12.2	33.3	6	13	PC-3
7:30:54.99	16028P	3	12.2	33.3	6	13	
7:30:55.03	16029P	3	12.2	33.3	6	13	
7:30:55.06	16030P	3	12.2	33.3	6	13	
7:30:55.09	16031P	3	12.2	33.3	6	13	
7:30:55.13	16032P	3	12.2	33.3	6	13	
7:30:55.16	16033P	3	12.2	33.3	6	13	
7:30:55.20	16034P	3	12.2	33.3	6	13	
7:30:55.23	16035T	0	12.2	33.3	6	13	
7:30:55.26	16036T	0	12.2	33.3	6	13	
7:30:55.30	16037P	3	12.2	33.3	6	13	
7:30:55.33	16038P	3	12.2	33.3	6	13	
7:30:55.36	16039P	3	12.2	33.3	6	13	
7:30:55.40	16040P	3	12.2	33.3	6	13	
7:30:55.43	16041P	3	12.2	33.3	6	13	
7:30:55.46	16042P	3	12.2	33.3	6	13	
7:30:55.50	16043P	3	12.2	33.3	6	13	

Table B1 - Telemetry Frames and Camera Parameters (Cont'd)

UMT	Telemetry Frame	Filter	Tracker Exp. Time (ms)	Plume Exp. Time (ms)	Tracker Gain	Plume Gain	Comments
7:30:55.53	16044P	3	12.2	33.3	6	13	
7:30:55.56	16045T	0	12.2	33.3	6	13	
7:30:55.60	16046T	0	12.2	33.3	6	13	
7:30:55.63	16047P	3	12.2	33.3	6	13	
7:30:55.66	16048P	3	12.2	33.3	6	13	
7:30:55.70	16049P	3	12.2	33.3	6	13	
7:30:55.73	16050P	3	12.2	33.3	6	13	
7:30:55.76	16051P	3	12.2	33.3	6	13	
7:30:55.80	16052P	3	12.2	33.3	6	13	
7:30:55.83	16053P	3	12.2	33.3	6	13	
7:30:55.86	16054P	3	12.2	33.3	6	13	
7:30:55.90	16055T	0	12.2	33.3	6	13	
7:30:55.93	16056T	0	12.2	33.3	6	13	
7:30:55.96	16057P	3	12.2	33.3	6	13	
7:30:56.00	16058P	3	12.2	33.3	6	13	
7:30:56.03	16059P	3	12.2	33.3	6	13	
7:30:56.06	16060P	3	12.2	33.3	6	13	
7:30:56.73	16080P	3	12.2	33.3	6	13	
7:30:56.76	16081P	3	12.2	33.3	6	13	
7:30:56.80	16082P	3	12.2	33.3	6	13	
7:30:56.83	16083P	3	12.2	33.3	6	13	
7:30:56.86	16084P	3	12.2	33.3	6	13	
7:30:56.90	16085T	0	12.2	33.3	6	13	
7:30:56.93	16086T	0	12.2	33.3	6	13	
7:30:56.96	16087P	3	12.2	33.3	6	13	
7:30:57.00	16088P	3	12.2	33.3	6	13	
7:30:57.03	16089P	3	12.2	33.3	6	13	
7:30:57.06	16090P	3	12.2	33.3	6	13	
7:30:57.10	16091P	3	12.2	33.3	6	13	
7:30:57.13	16092P	3	12.2	33.3	6	13	
7:30:57.16	16093P	3	12.2	33.3	6	13	
7:30:57.20	16094P	3	12.2	33.3	6	13	
7:30:57.23	16095T	0	12.2	33.3	6	13	
7:30:57.26	16096T	0	12.2	33.3	6	13	
7:30:57.30	16097P	3	12.2	33.3	6	13	
7:30:57.33	16098P	3	12.2	33.3	6	13	
7:30:57.36	16099P	3	12.2	33.3	6	13	
7:30:57.40	16100P	3	12.2	33.3	6	13	
7:30:57.43	16101P	3	12.2	33.3	6	13	
7:30:57.46	16102P	3	12.2	33.3	6	13	
7:30:57.50	16103P	3	12.2	33.3	6	13	
7:30:57.53	16104P	3	12.2	33.3	6	13	
7:30:57.56	16105T	0	12.2	33.3	6	13	
7:30:57.60	16106T	0	12.2	33.3	6	13	
7:30:57.63	16107P	3	12.2	33.3	6	13	
7:30:57.66	16108P	3	12.2	33.3	6	13	
7:30:57.70	16109P	3	12.2	33.3	6	13	
7:30:57.73	16110P	3	12.2	33.3	6	13	
7:30:57.76	16111P	3	12.2	33.3	6	13	
7:30:57.80	16112P	3	12.2	33.3	6	13	
7:30:57.83	16113P	3	12.2	33.3	6	13	
7:30:57.86	16114P	3	12.2	33.3	6	13	
7:30:57.90	16115T	0	12.2	33.3	6	13	
7:30:57.93	16116T	0	12.2	33.3	6	13	
7:30:57.96	16117P	3	12.2	33.3	6	13	



Table B1 - Telemetry Frames and Camera Parameters (Cont'd)

UMT	Telemetry Frame	Filter	Tracker Exp. Time (ms)	Plume Exp. Time (ms)	Tracker Gain	Plume Gain	Comments
7:30:58.00	16118P	3	12.2	33.3	6	13	
7:30:58.03	16119P	3	12.2	33.3	6	13	End data
7:30:58.06	16120P	3	12.2	33.3	6	13	interval 2
7:31: 3.64	16287P	2	12.2	33.3	6	12	Begin data
7:31: 3.67	16288P	2	12.2	33.3	6	12	interval 3
7:31: 3.70	16289P	2	12.2	33.3	6	12	PC-2
7:31: 3.74	16290P	2	12.2	33.3	6	12	
7:31: 3.77	16291P	2	12.2	33.3	6	12	
7:31: 3.80	16292P	2	12.2	33.3	6	12	
7:31: 3.84	16293P	2	12.2	33.3	6	12	
7:31: 3.87	16294P	2	12.2	33.3	6	12	
7:31: 3.90	16295T	0	12.2	33.3	6	12	
7:31: 3.94	16296T	0	12.2	33.3	6	12	
7:31: 3.97	16297P	2	12.2	33.3	6	12	
7:31: 4.00	16298P	2	12.2	33.3	6	12	
7:31: 4.04	16299P	2	12.2	33.3	6	12	
7:31: 4.07	16300P	2	12.2	33.3	6	12	
7:31: 4.11	16301P	2	12.2	33.3	6	12	
7:31: 4.14	16302P	2	12.2	33.3	6	12	
7:31: 4.17	16303P	2	12.2	33.3	6	12	
7:31: 4.21	16304P	2	12.2	33.3	6	12	
7:31: 4.24	16305T	0	12.2	33.3	6	12	
7:31: 4.27	16306T	0	12.2	33.3	6	12	
7:31: 4.31	16307P	2	12.2	33.3	6	12	
7:31: 4.34	16308P	2	12.2	33.3	6	12	
7:31: 4.37	16309P	2	12.2	33.3	6	12	
7:31: 4.41	16310P	2	12.2	33.3	6	12	
7:31: 4.44	16311P	2	12.2	33.3	6	12	
7:31: 4.47	16312P	2	12.2	33.3	6	12	
7:31: 4.51	16313P	2	12.2	33.3	6	12	
7:31: 4.54	16314P	2	12.2	33.3	6	12	
7:31: 4.57	16315T	0	12.2	33.3	6	12	
7:31: 4.61	16316T	0	12.2	33.3	6	12	
7:31: 4.64	16317P	2	12.2	33.3	6	12	
7:31: 4.67	16318P	2	12.2	33.3	6	12	
7:31: 4.71	16319P	2	12.2	33.3	6	12	
7:31: 4.74	16320P	2	12.2	33.3	6	12	
7:31: 4.77	16321P	2	12.2	33.3	6	12	
7:31: 4.81	16322P	2	12.2	33.3	6	12	
7:31: 4.84	16323P	2	12.2	33.3	6	12	
7:31: 4.87	16324P	2	12.2	33.3	6	12	
7:31: 4.91	16325T	0	12.2	33.3	6	12	
7:31: 4.94	16326T	0	12.2	33.3	6	12	
7:31: 4.97	16327P	2	12.2	33.3	6	12	
7:31: 5.01	16328P	2	12.2	33.3	6	12	
7:31: 5.04	16329P	2	12.2	33.3	6	12	
7:31: 5.07	16330P	2	12.2	33.3	6	12	
7:31: 5.11	16331P	2	12.2	33.3	6	12	
7:31: 5.14	16332P	2	12.2	33.3	6	12	
7:31: 5.17	16333P	2	12.2	33.3	6	12	
7:31: 5.21	16334P	2	12.2	33.3	6	12	
7:31: 5.24	16335T	0	12.2	33.3	6	12	
7:31: 5.27	16336T	0	12.2	33.3	6	12	
7:31: 5.31	16337P	2	12.2	33.3	6	12	

Table B1 - Telemetry Frames and Camera Parameters (Cont'd)

UMT	Telemetry Frame	Filter	Tracker Exp. Time (ms)	Plume Exp. Time (ms)	Tracker Gain	Plume Gain	Comments
7:31: 5.34	16338P	2	12.2	33.3	6	12	
7:31: 5.37	16339P	2	12.2	33.3	6	12	
7:31: 5.41	16340P	2	12.2	33.3	6	12	
7:31: 5.44	16341P	2	12.2	33.3	6	12	
7:31: 5.47	16342P	2	12.2	33.3	6	12	
7:31: 5.51	16343P	2	12.2	33.3	6	12	
7:31: 5.54	16344P	2	12.2	33.3	6	12	
7:31: 5.57	16345T	0	12.2	33.3	6	12	
7:31: 5.61	16346T	0	12.2	33.3	6	12	
7:31: 5.64	16347P	2	12.2	33.3	6	12	
7:31: 5.67	16348P	2	12.2	33.3	6	12	
7:31: 5.71	16349P	2	12.2	33.3	6	12	
7:31: 5.74	16350P	2	12.2	33.3	6	12	
7:31: 5.77	16351P	2	12.2	33.3	6	12	
7:31: 5.81	16352P	2	12.2	33.3	6	12	
7:31: 5.84	16353P	2	12.2	33.3	6	12	
7:31: 5.87	16354P	2	12.2	33.3	6	12	
7:31: 5.91	16355T	0	12.2	33.3	6	12	
7:31: 5.94	16356T	0	12.2	33.3	6	12	
7:31: 5.97	16357P	2	12.2	33.3	6	12	
7:31: 6.01	16358P	2	12.2	33.3	6	12	
7:31: 6.04	16359P	2	12.2	33.3	6	12	
7:31: 6.07	16360P	2	12.2	33.3	6	12	
7:31: 6.11	16361P	2	12.2	33.3	6	12	
7:31: 6.14	16362P	2	12.2	33.3	6	12	
7:31: 6.17	16363P	2	12.2	33.3	6	12	
7:31: 6.21	16364P	2	12.2	33.3	6	12	
7:31: 6.24	16365T	0	12.2	33.3	6	12	
7:31: 6.27	16366T	0	12.2	33.3	6	12	
7:31: 6.31	16367P	2	12.2	33.3	6	12	
7:31: 6.34	16368P	2	12.2	33.3	6	12	
7:31: 6.37	16369P	2	12.2	33.3	6	12	
7:31: 6.41	16370P	2	12.2	33.3	6	12	
7:31: 6.44	16371P	2	12.2	33.3	6	12	
7:31: 6.47	16372P	2	12.2	33.3	6	12	
7:31: 6.51	16373P	2	12.2	33.3	6	12	
7:31: 6.54	16374P	2	12.2	33.3	6	12	
7:31: 6.57	16375T	0	12.2	33.3	6	12	
7:31: 6.61	16376T	0	12.2	33.3	6	12	
7:31: 6.64	16377P	2	12.2	33.3	6	12	
7:31: 6.67	16378P	2	12.2	33.3	6	12	
7:31: 6.71	16379P	2	12.2	33.3	6	12	
7:31: 6.74	16380P	2	12.2	33.3	6	12	
7:31: 6.77	16381P	2	12.2	33.3	6	12	
7:31: 6.81	16382P	2	12.2	33.3	6	12	
7:31: 6.84	16383P	2	12.2	33.3	6	12	
7:31: 6.87	16384P	2	12.2	33.3	6	12	
7:31: 6.91	16385T	0	12.2	33.3	6	12	
7:31: 6.94	16386T	0	12.2	33.3	6	12	
7:31: 6.97	16387P	2	12.2	33.3	6	12	
7:31: 7.01	16388P	2	12.2	33.3	6	12	
7:31: 7.04	16389P	2	12.2	33.3	6	12	
7:31: 7.08	16390P	2	12.2	33.3	6	12	
7:31: 7.11	16391P	2	12.2	33.3	6	12	
7:31: 7.14	16392P	2	12.2	33.3	6	12	

Table B1 - Telemetry Frames and Camera Parameters (Cont'd)

UMT	Telemetry Frame	Filter	Tracker Exp. Time (ms)	Plume Exp. Time (ms)	Tracker Gain	Plume Gain	Comments
7:31: 7.18	16393P	2	12.2	33.3	6	12	
7:31: 7.21	16394P	2	12.2	33.3	6	12	
7:31: 7.24	16395T	0	12.2	33.3	6	12	
7:31: 7.28	16396T	0	12.2	33.3	6	12	
7:31: 7.31	16397P	2	12.2	33.3	6	12	
7:31: 7.34	16398P	2	12.2	33.3	6	12	
7:31: 7.38	16399P	2	12.2	33.3	6	12	
7:31: 7.41	16400P	2	12.2	33.3	6	12	
7:31: 7.44	16401P	2	12.2	33.3	6	12	
7:31: 7.48	16402P	2	12.2	33.3	6	12	
7:31: 7.51	16403P	2	12.2	33.3	6	12	
7:31: 7.54	16404P	2	12.2	33.3	6	12	End data
7:31: 7.58	16405T	0	12.2	33.3	6	12	interval 3
7:31:20.99	16807P	1	15.402	33.3	5	11	Begin data
7:31:21.02	16808P	1	15.402	33.3	5	11	interval 4
7:31:21.06	16809P	1	15.402	33.3	5	11	PC-1
7:31:21.09	16810P	1	15.402	33.3	5	11	
7:31:21.12	16811P	1	15.402	33.3	5	11	
7:31:21.16	16812P	1	15.402	33.3	5	11	
7:31:21.19	16813P	1	15.402	33.3	5	11	
7:31:21.22	16814P	1	15.402	33.3	5	11	
7:31:21.26	16815T	0	15.402	33.3	5	11	
7:31:21.29	16816T	0	15.402	33.3	5	11	
7:31:21.32	16817P	1	15.402	33.3	5	11	
7:31:21.36	16818P	1	15.402	33.3	5	11	
7:31:21.39	16819P	1	15.402	33.3	5	11	
7:31:21.42	16820P	1	15.402	33.3	5	11	
7:31:21.46	16821P	1	15.402	33.3	5	11	
7:31:21.49	16822P	1	15.402	33.3	5	11	
7:31:21.52	16823P	1	15.402	33.3	5	11	
7:31:21.56	16824P	1	15.402	33.3	5	11	
7:31:21.59	16825T	0	15.402	33.3	5	11	
7:31:21.62	16826T	0	15.402	33.3	5	11	
7:31:21.66	16827P	1	15.402	33.3	5	11	
7:31:21.69	16828P	1	15.402	33.3	5	11	
7:31:21.72	16829P	1	15.402	33.3	5	11	
7:31:21.76	16830P	1	15.402	33.3	5	11	
7:31:21.79	16831P	1	15.402	33.3	5	11	
7:31:21.82	16832P	1	15.402	33.3	5	11	
7:31:21.86	16833P	1	15.402	33.3	5	11	
7:31:21.89	16834P	1	15.402	33.3	5	11	
7:31:21.93	16835T	0	15.402	33.3	5	11	
7:31:21.96	16836T	0	15.402	33.3	5	11	
7:31:21.99	16837P	1	15.402	33.3	5	11	
7:31:22.03	16838P	1	15.402	33.3	5	11	
7:31:22.06	16839P	1	15.402	33.3	5	11	
7:31:22.09	16840P	1	15.402	33.3	5	11	
7:31:22.13	16841P	1	15.402	33.3	5	11	
7:31:22.16	16842P	1	15.402	33.3	5	11	
7:31:22.19	16843P	1	15.402	33.3	5	11	
7:31:22.23	16844P	1	15.402	33.3	5	11	
7:31:22.26	16845T	0	15.402	33.3	5	11	
7:31:22.29	16846T	0	15.402	33.3	5	11	
7:31:22.33	16847P	1	15.402	33.3	5	11	

Table B1 - Telemetry Frames and Camera Parameters (Cont'd)

UMT	Telemetry Frame	Filter	Tracker Exp. Time (ms)	Plume Exp. Time (ms)	Tracker Gain	Plume Gain	Comments
7:31:22.36	16848P	1	15.402	33.3	5	11	
7:31:22.39	16849P	1	15.402	33.3	5	11	
7:31:22.43	16850P	1	15.402	33.3	5	11	
7:31:22.46	16851P	1	15.402	33.3	5	11	
7:31:22.49	16852P	1	15.402	33.3	5	11	
7:31:22.53	16853P	1	15.402	33.3	5	11	
7:31:22.56	16854P	1	15.402	33.3	5	11	
7:31:22.59	16855T	0	15.402	33.3	5	11	
7:31:22.63	16856T	0	15.402	33.3	5	11	
7:31:22.66	16857P	1	15.402	33.3	5	11	
7:31:22.69	16858P	1	15.402	33.3	5	11	
7:31:22.73	16859P	1	15.402	33.3	5	11	
7:31:22.76	16860P	1	15.402	33.3	5	11	
7:31:22.79	16861P	1	15.402	33.3	5	11	
7:31:22.83	16862P	1	15.402	33.3	5	11	
7:31:22.86	16863P	1	15.402	33.3	5	11	
7:31:22.89	16864P	1	15.402	33.3	5	11	
7:31:22.93	16865T	0	15.402	33.3	5	11	
7:31:22.96	16866T	0	15.402	33.3	5	11	
7:31:22.99	16867P	1	15.402	33.3	5	11	
7:31:23.03	16868P	1	15.402	33.3	5	11	
7:31:23.06	16869P	1	15.402	33.3	5	11	
7:31:23.09	16870P	1	15.402	33.3	5	11	
7:31:23.13	16871P	1	15.402	33.3	5	11	
7:31:23.16	16872P	1	15.402	33.3	5	11	
7:31:23.19	16873P	1	15.402	33.3	5	11	
7:31:23.23	16874P	1	15.402	33.3	5	11	
7:31:23.26	16875T	0	15.402	33.3	5	11	
7:31:23.29	16876T	0	15.402	33.3	5	11	
7:31:23.33	16877P	1	15.402	33.3	5	11	
7:31:23.36	16878P	1	15.402	33.3	5	11	
7:31:23.39	16879P	1	15.402	33.3	5	11	
7:31:23.43	16880P	1	15.402	33.3	5	11	
7:31:23.46	16881P	1	15.402	33.3	5	11	
7:31:23.49	16882P	1	15.402	33.3	5	11	
7:31:23.53	16883P	1	15.402	33.3	5	11	
7:31:23.56	16884P	1	15.402	33.3	5	11	
7:31:23.59	16885T	0	15.402	33.3	5	11	
7:31:23.63	16886T	0	15.402	33.3	5	11	
7:31:23.66	16887P	1	15.402	33.3	5	11	
7:31:23.69	16888P	1	15.402	33.3	5	11	
7:31:23.73	16889P	1	15.402	33.3	5	11	
7:31:23.76	16890P	1	15.402	33.3	5	11	
7:31:23.79	16891P	1	15.402	33.3	5	11	
7:31:23.83	16892P	1	15.402	33.3	5	11	
7:31:23.86	16893P	1	15.402	33.3	5	11	
7:31:23.89	16894P	1	15.402	33.3	5	11	
7:31:23.93	16895T	0	15.402	33.3	5	11	
7:31:23.96	16896T	0	15.402	33.3	5	11	
7:31:23.99	16897P	1	15.402	33.3	5	11	
7:31:24.03	16898P	1	15.402	33.3	5	11	
7:31:24.06	16899P	1	15.402	33.3	5	11	
7:31:24.09	16900P	1	15.402	33.3	5	11	
7:31:24.13	16901P	1	15.402	33.3	5	11	
7:31:24.16	16902P	1	15.402	33.3	5	11	

Table B1 - Telemetry Frames and Camera Parameters (Cont'd)

UMT	Telemetry Frame	Filter	Tracker Exp. Time (ms)	Plume Exp. Time (ms)	Tracker Gain	Plume Gain	Comments
7:31:24.19	16903P	1	15.402	33.3	5	11	
7:31:24.23	16904P	1	15.402	33.3	5	11	
7:31:24.26	16905T	0	15.402	33.3	5	11	
7:31:24.29	16906T	0	15.402	33.3	5	11	
7:31:24.33	16907P	1	15.402	33.3	5	11	
7:31:24.36	16908P	1	15.402	33.3	5	11	
7:31:24.39	16909P	1	15.402	33.3	5	11	
7:31:24.43	16910P	1	15.402	33.3	5	11	
7:31:24.46	16911P	1	15.402	33.3	5	11	
7:31:24.49	16912P	1	15.402	33.3	5	11	
7:31:24.53	16913P	1	15.402	33.3	5	11	
7:31:24.56	16914P	1	15.402	33.3	5	11	End data
7:31:24.59	16915T	0	15.402	33.3	5	11	interval 4

## GLOSSARY

ARI	average radiant intensity
ASRI	average spectral radiant intensity
CCD	charge-coupled device
CHARM	Composite High Altitude Radiation Model
DN	digital number
DN/PE	digital number per photoevent
ECF	Earth center-fixed
FOR	field of regard
FOV	Field of view
FWHM	full-width-half-maximum
GMT	Greenwich Mean Time
Hz	Hertz
ICCD	intensified charge-coupled device
IDA	Institute for Defense Analyses
IR	infrared
K	degrees Kelvin
LACE	Low-power Atmospheric Compensation Experiment
LCLV	Low-cost launch vehicle
LOS	line of sight
Mbps	megabits per second
MCP	microchannel plate
MHz	megaHz
NER	noise-equivalent radiance
NQE	net quantum efficiency
NRL	Naval Research Laboratory
PC-N	plume camera filter, N = 1, 2, 3, 4
PE	photoevent
PSF	point spread function
RMS	root mean square
SDIO	Strategic Defense Initiative Organization
SNR	signal-to-noise ratio
sr	Steradian
TALO	time after liftoff
UMT	UVPI mission time
UV	ultraviolet
UVPI	Ultraviolet Plume Instrument
W	watt